

# The effect of nodal topology on cellular solid mechanics

A preliminary diagnostic experimental investigation



**Derron T.J. van Helvoort**

Supervisor:

**Assistant Professor Calvin D. Rans**

Assessment Committee:

**Professor Clemens A. Dransfeld**

**Assistant Professor Calvin D. Rans**

**Assistant Professor Julie J.E. Teuwen**

**Assistant Professor Otto K. Bergsma**

Faculty of Aerospace Engineering

Delft University of Technology

This thesis is in partial fulfillment for the degree of  
*Master of Science*

Aerospace Structures and Materials  
ALM Research Group

December 2018



TO MY WONDERFUL MOTHER AND FATHER, KIM & PA,  
*for their many sacrifices, encouragement, and belief in me;*

TO MY YOUNGER SISTER, MARIELLE,  
*for her raillery, and good taste in music;*

TO MY PATERNAL GRANDPARENTS, OPA & TUTU  
*for my first visit to the Aerospace Engineering Faculty, en mij altijd aangemoedigd hebben;*

TO MY MATERNAL GRANDPARENTS, GRANDMA & GRANDPA  
*for their unwavering enthusiasm, and rooting for me;*

AND TO MY AMAZING PARTNER, ISABELLE  
*for her wit, her kindness, and precisely enough patience to stick it out.*



## **Declaration**

I hereby declare that except where specific references are made, and except for this declaration, the contents of this Master of Science Thesis are original and have not been submitted in whole or in part for consideration for any other degree or qualification in this, or any other university. This thesis is my own work and contains nothing which is the outcome of work done in collaboration with others, except as specified in the text and Acknowledgements.

Derron T.J. van Helvoort  
December 2018



## Acknowledgements

Thank you Calvin Rans for giving me the opportunity to catch a glimpse of a hugely interesting niche, for your time, your measured words, and for your very thoughtful guidance. Although the Additive Layer Manufacturing Research Group is still getting established, I was proud to be a part of it.

Thank you Megan Walker for getting me started in my literature review, and for sharing your knowledge of the 3-D printers, and your insights. “Layers of structure for layers of damage”.

Thank you Gertjan Mulder for the patient support without which I would have undoubtedly spent several more weeks in the DASML, and for the friendly chats in and around those times. Thank you Cees Paalvast, Berthil Grashof, Misja Huizinga, and Johan Boender for your craftsmanship, time, flexibility and experience. Thank you Bram, Ivar and Vincent in the Structural Integrity & Composites Masters Office for many a restorative coffee or lunch-time conversation, and for a constructive collaborative relationship regarding experimental procedures.

Thank you Otto Bergsma for all of those enthusiastic and creative conversations, throughout the entire Master Program and during my Bachelor Design Synthesis Exercise.

I am fortunate to be surrounded by so many important people. Thank you all for the good times outside of this thesis. Thank you everyone at the Delft University of Technology, at SRC Thor, and at MareVisie. Ralph and Michiel, you have both made it a point to support me, and I am really grateful for it.

Lastly, I would like to acknowledge Krishna Kumar and the University of Cambridge’s Department of Engineering for making this L<sup>A</sup>T<sub>E</sub>X-template openly available for myself and other students around the World.





## **Abstract**

Additive manufacturing allows material structuring, supporting the fabrication of multiple-level structures or metamaterials. Through the lens of classical stress reduction, nature's cellular solid structures feature stress-homogenizing nodal topologies. Avian long bones are an example. Research into the mechanics of open cell cellular solids seems focused on the effectiveness of unit cell architecture and neglects the detailed behavior of constituent nodes. Several specimen series were printed on the nodal- and cellular solid-levels of analysis, all with varying nodal topologies. A discussion of force-displacement and digital image correlation experimental data is had; the cellular solid deflection rigidity seems highly sensitive to nodal topology under quasi-static compression. It is thought that bioinspired profiles successfully homogenize stress and improve load transfer, mitigating nodal softening: peak stresses and the propagation of nodal torsion into adjoining strut deflection decreased. This sensitivity is relevant for lightweight strain energy absorption and stiffness provision, and demands further research.



# Table of contents

List of figures	xv
List of tables	xvii
Nomenclature	xix
<b>I Project initiation &amp; literature review</b>	<b>1</b>
<b>1 Introduction</b>	<b>3</b>
<b>2 Background information</b>	<b>5</b>
2.1 Looking to nature . . . . .	5
2.1.1 Mattheck's stress-homogenizing curve . . . . .	5
2.1.2 Bone structure and functional grading . . . . .	6
2.2 Cellular solids . . . . .	10
2.2.1 Natural cellular solids . . . . .	10
2.2.2 Cellular solid mechanics . . . . .	11
2.2.3 Cellular solids as crush structures . . . . .	13
2.3 Key engineering concepts . . . . .	14
2.3.1 Plane stress problems . . . . .	14
2.3.2 Saint-Venant's problem & principle . . . . .	15
2.3.3 Beam structures . . . . .	15
2.3.4 Classical stress-reduction in engineering design . . . . .	16
2.3.5 The Von Mises equivalent strain . . . . .	20
<b>3 Research definition</b>	<b>23</b>
3.1 Research scope . . . . .	23
3.2 Author inspiration, opinions and personal biases . . . . .	24
3.3 Hypotheses . . . . .	24

<b>II</b>	<b>Nodes</b>	<b>27</b>
<b>4</b>	<b>Nodal-level methodology</b>	<b>29</b>
4.1	Specimen design . . . . .	29
4.1.1	Nodal fillet shapes . . . . .	30
4.1.2	Infinite node specimens . . . . .	30
4.1.3	Finite node specimens . . . . .	31
4.2	Methodology validity . . . . .	31
4.2.1	Material considerations . . . . .	31
4.2.2	Strut deflection rigidity . . . . .	31
4.2.3	Nominal strain . . . . .	32
4.3	Experimental design . . . . .	32
4.3.1	Test goal . . . . .	32
4.3.2	Chosen approach . . . . .	32
<b>5</b>	<b>Nodal-level data processing</b>	<b>35</b>
5.1	Digital image correlation . . . . .	35
5.1.1	System calibration . . . . .	35
5.1.2	Appending load cell data to DIC images . . . . .	35
5.1.3	Area of interest . . . . .	35
5.1.4	Blending the DIC data . . . . .	36
5.2	Apparent flexural rigidity . . . . .	36
5.3	Initial deflection rigidity . . . . .	37
5.4	Strain concentration visualization . . . . .	37
<b>6</b>	<b>Nodal-level results</b>	<b>39</b>
6.1	Infinite node specimens . . . . .	40
6.1.1	Strut deflection rigidity . . . . .	40
6.1.2	Strut deflection analysis . . . . .	41
6.1.3	Strut free boundary analysis . . . . .	42
6.1.4	Plane strain section analysis . . . . .	44
6.1.5	Equivalent strut length calculations . . . . .	44
6.2	Finite node specimens . . . . .	45
<b>III</b>	<b>Honeycombs</b>	<b>55</b>
<b>7</b>	<b>Cellular solid level methodology</b>	<b>57</b>
7.1	Specimen design . . . . .	57
7.1.1	Nodal fillet shapes . . . . .	57

---

7.1.2	Specimen development . . . . .	58
7.1.3	Chosen specimen design . . . . .	59
7.2	Methodology validity . . . . .	60
7.3	Experimental design . . . . .	60
7.3.1	Test goal . . . . .	60
7.3.2	Specimen preparation and camera calibration . . . . .	60
7.3.3	Experiment procedure . . . . .	61
<b>8</b>	<b>Cellular solid level data processing</b>	<b>63</b>
8.1	Apparent initial flexural rigidity . . . . .	63
8.2	Normalized specimen strain energy absorption before break . . . . .	63
<b>9</b>	<b>Cellular solid level results</b>	<b>65</b>
<b>IV</b>	<b>Discussion, conclusions &amp; recommendations</b>	<b>75</b>
<b>10</b>	<b>Discussion</b>	<b>77</b>
10.1	A synthesis of the experimental evidence . . . . .	77
10.2	Implications for further research and potential applications . . . . .	88
<b>11</b>	<b>Conclusions &amp; Recommendations</b>	<b>91</b>
11.1	Conclusions . . . . .	91
11.2	Recommendations . . . . .	93
	<b>References</b>	<b>97</b>
	<b>Appendices</b>	<b>101</b>
<b>A</b>	<b>Young's modulus analysis</b>	<b>103</b>
<b>B</b>	<b>Experiment development and further information</b>	<b>105</b>
B.1	Specimen clamping . . . . .	105
B.2	Specimen preparation . . . . .	105
B.3	Camera and lighting considerations . . . . .	106
B.4	Specimen technical drawings . . . . .	106
<b>C</b>	<b>Overview of VIC3D 8 settings</b>	<b>117</b>



# List of figures

1.1	Richard Feynman . . . . .	3
1.2	Root-knot nematode . . . . .	4
1.3	Additively manufactured lattices . . . . .	4
2.1	Mattheck's curve . . . . .	6
2.2	Mammalian long bone . . . . .	7
2.3	Knee implant prototype . . . . .	8
2.4	Characteristics of avian long bones . . . . .	9
2.5	Cross-section of avian long bone . . . . .	10
2.6	Stretch- and bending-dominated structures . . . . .	11
2.7	General cellular solid behavior . . . . .	12
2.8	Effect of stepped shoulder size on stress concentration . . . . .	18
2.9	Effect of base thickness on stress concentration . . . . .	19
2.10	Baud's curve . . . . .	20
2.11	Photoelastic photograph of a cantilever . . . . .	21
2.12	Comparing designs . . . . .	22
6.1	Force-displacement of infinite nodes . . . . .	41
6.2	Initial deflection rigidity of infinite nodes . . . . .	42
6.3	Infinite node rotation review . . . . .	43
6.4	Strut deformation for 1 % tip deflection . . . . .	43
6.5	Strut deformation for 1 % tip deflection . . . . .	44
6.6	Apparent bending stiffness for 1 % tip deflection . . . . .	45
6.7	Major principal strain for 1 % tip deflection . . . . .	46
6.8	Major principal stress concentration for 1 % tip deflection . . . . .	47
6.9	Infinite node internal strains . . . . .	48
6.10	Infinite node equivalent Von Mises strains . . . . .	49
6.11	Force-displacement of finite nodes . . . . .	50
6.12	Initial deflection rigidity of finite nodes . . . . .	50
6.13	Strut deformation for 1 % tip deflection . . . . .	50

6.14	Strut deformation for 1 % tip deflection . . . . .	51
6.15	Apparent bending stiffness for 1 % tip deflection . . . . .	51
6.16	Major principal strain for 1 % tip deflection . . . . .	52
6.17	Major principal stress concentration for 1 % tip deflection . . . . .	52
6.18	Finite node internal strains . . . . .	53
6.19	Finite node equivalent Von Mises strains . . . . .	54
7.1	Generalized hexagonal honeycomb specimen . . . . .	59
9.1	Force-displacement of the hexagonal honeycombs . . . . .	66
9.2	Volume-normalized initial deflection rigidities . . . . .	67
9.3	Relative density and initial deflection rigidity . . . . .	68
9.4	Energy absorption of hexagonal specimens ( $F_{ult}$ ) . . . . .	69
9.5	Energy absorption of hexagonal specimens ( $\delta_{ult}$ ) . . . . .	69
9.6	Bathtub curves for hexagonal honeycomb for 1 % tip deflection . . . . .	70
9.7	Un-filleted honeycomb fragments . . . . .	71
9.8	Circular-filleted honeycomb fragments . . . . .	72
9.9	Mattheck-filleted honeycomb fragments . . . . .	73
9.10	Lumped-node honeycomb fragments . . . . .	74
10.1	Infinite-node theoretical versus apparent bending stiffness . . . . .	80
10.2	Finite-node theoretical versus apparent bending stiffness . . . . .	81
10.3	Infinite node internal strains . . . . .	83
10.4	Finite node internal strains . . . . .	84
10.5	Infinite-node equivalent Von Mises strains . . . . .	85
10.6	Finite-node equivalent Von Mises strains . . . . .	86
A.1	The Young's modulus of Formlabs resin dependence on time . . . . .	104
B.1	Un-filleted infinite node specimen . . . . .	107
B.2	Circular-filleted infinite node specimen . . . . .	108
B.3	Mattheck-filleted infinite node specimen . . . . .	109
B.4	Baud-filleted infinite node specimen . . . . .	110
B.5	Un-filleted finite node specimen . . . . .	110
B.6	Circular-filleted finite node specimen . . . . .	111
B.7	Mattheck-filleted finite node specimen . . . . .	111
B.8	Baud-filleted finite node specimen . . . . .	112
B.9	Un-filleted hexagonal honeycomb specimen . . . . .	113
B.10	Circular-filleted hexagonal honeycomb specimen . . . . .	114
B.11	Mattheck-filleted hexagonal honeycomb specimen . . . . .	115
B.12	Lumped-node hexagonal honeycomb specimen . . . . .	116



# List of tables

4.1	Descriptive overview of fillet shapes . . . . .	30
4.2	Summary of the node-level test program . . . . .	33
6.1	Nodal specimen masses . . . . .	39
6.2	Nodal specimen volumes . . . . .	40
6.3	Infinite node specimen geometry . . . . .	40
6.4	Finite node specimen geometry . . . . .	40
6.5	Nodal specimen effective strut lengths . . . . .	46
7.1	Overview of nodal shapes . . . . .	58
7.2	Summary of cellular solid test program . . . . .	61
9.1	Honeycomb specimen projected volumes . . . . .	65
9.2	Overview of estimated honeycomb relative densities . . . . .	67
9.3	Overview of honeycomb specimen energy absorption . . . . .	68
11.1	Current status of the hypotheses . . . . .	92
C.1	VIC 3D 8 settings . . . . .	118



# Nomenclature

## Roman Symbols

$b$	Strut width	[m]
$C$	Complementary energy of flexure	[–]
$D$	Major shaft, strut or beam base depth	[m]
$d$	Minor shaft, strut or beam depth	[m]
$E$	Young's modulus, constant of material elasticity	[kg m <sup>-1</sup> s <sup>-2</sup> ]
$F$	Generic force vector	[kg m s <sup>-2</sup> ]
$h$	Un-filleted strut height	[m]
$I$	Second moment of area, moment of inertia	[m <sup>4</sup> ]
$K$	Stress concentration factor	[–]
$k$	Hooke constant, deflection rigidity	[kg s <sup>-2</sup> ]
$l$	Cell, strut, or wall length	[m]
$M$	Moment	[kg m <sup>2</sup> s <sup>-2</sup> ]
$f$	Component of an applied force	[kg m s <sup>-2</sup> ]
$P$	Critical failure mode force	[kg m s <sup>-2</sup> ]
$\partial$	Partial derivative	[–]
$n$	Order of Mattheck fillet	[–]
$r$	Geometric radius	[m]
$S$	Shear force	[kg m s <sup>-2</sup> ]
$t$	Cell, strut, or wall thickness	[m]

---

$U$	Strain energy absorption	[N m]
$v$	Vertical strut or beam deflection	[m]
$x$	Cartesian position of $yz$ -plane, the first dimension	[m]
$y$	Cartesian position of $xz$ -plane, the second dimension	[m]
$z$	Cartesian position of $xy$ -plane, the third dimension	[m]

### Greek Symbols

$\Delta$	“Change in”	
$\varepsilon$	Material strain	[-]
$\gamma$	Material shear strain	[-]
$\sigma$	Material stress	[kg m <sup>-1</sup> s <sup>-2</sup> ]
$\tau$	Material shear stress	[kg m <sup>-1</sup> s <sup>-2</sup> ]
$\theta$	Angle	[rad]

### Subscripts

1	Major principal direction
2	Minor principal direction
bf	Critical brittle failure stress
c	Strut or beam tip
crit	Critical force for some (identified) failure mode
dr	Deflection rigidity
idr	Initial deflection rigidity
eb	Elastic buckling
fs	Modulus of rupture
max	Maximum
min	Minimum
nf	No fillet (design baseline)

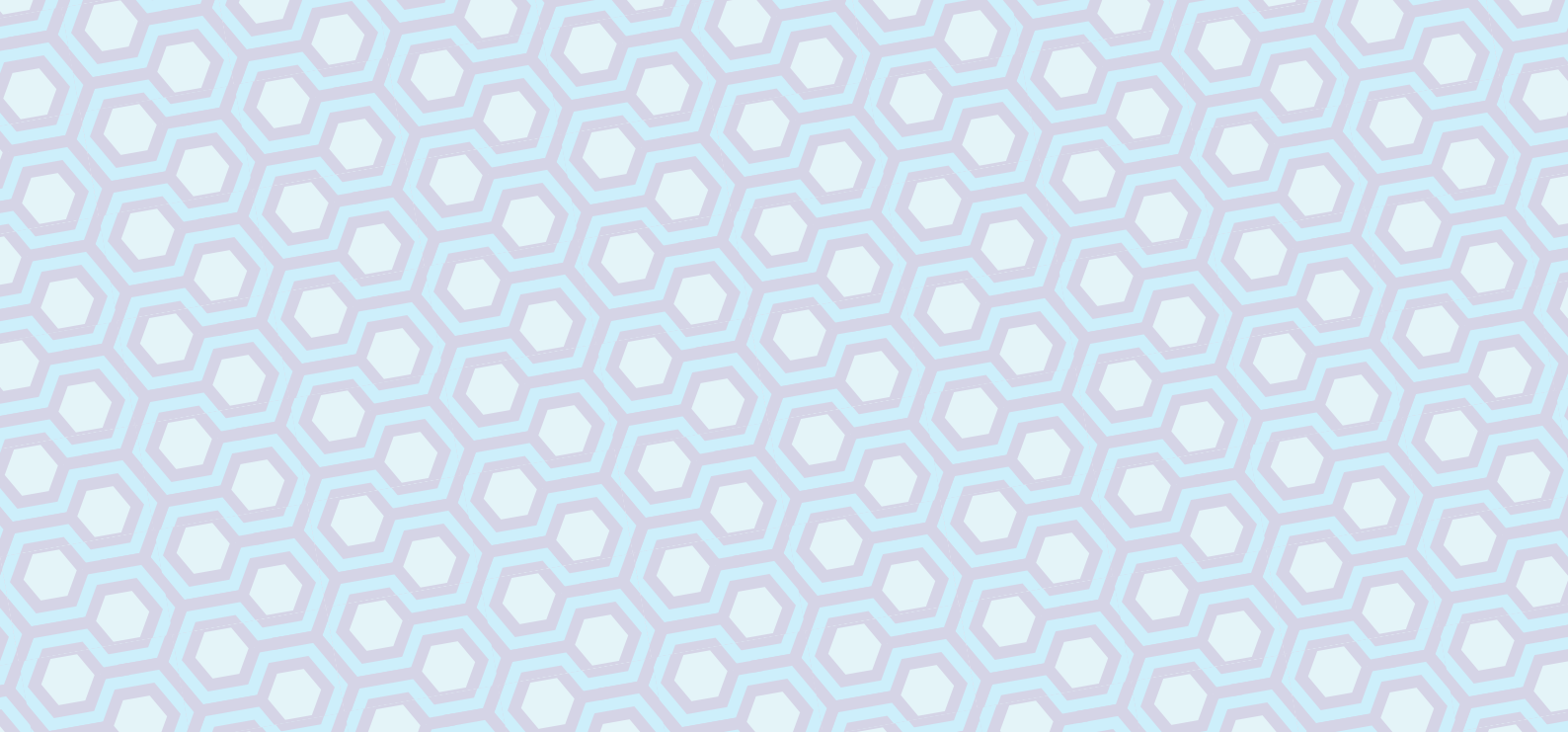
---

nom	Nominal (reference)
pl	Critical plastic stress
t	Theoretical (stress concentration factor)
ult	Ultimate
V	Per unit volume
ys	Critical yield stress

**Acronyms and Abbreviations**

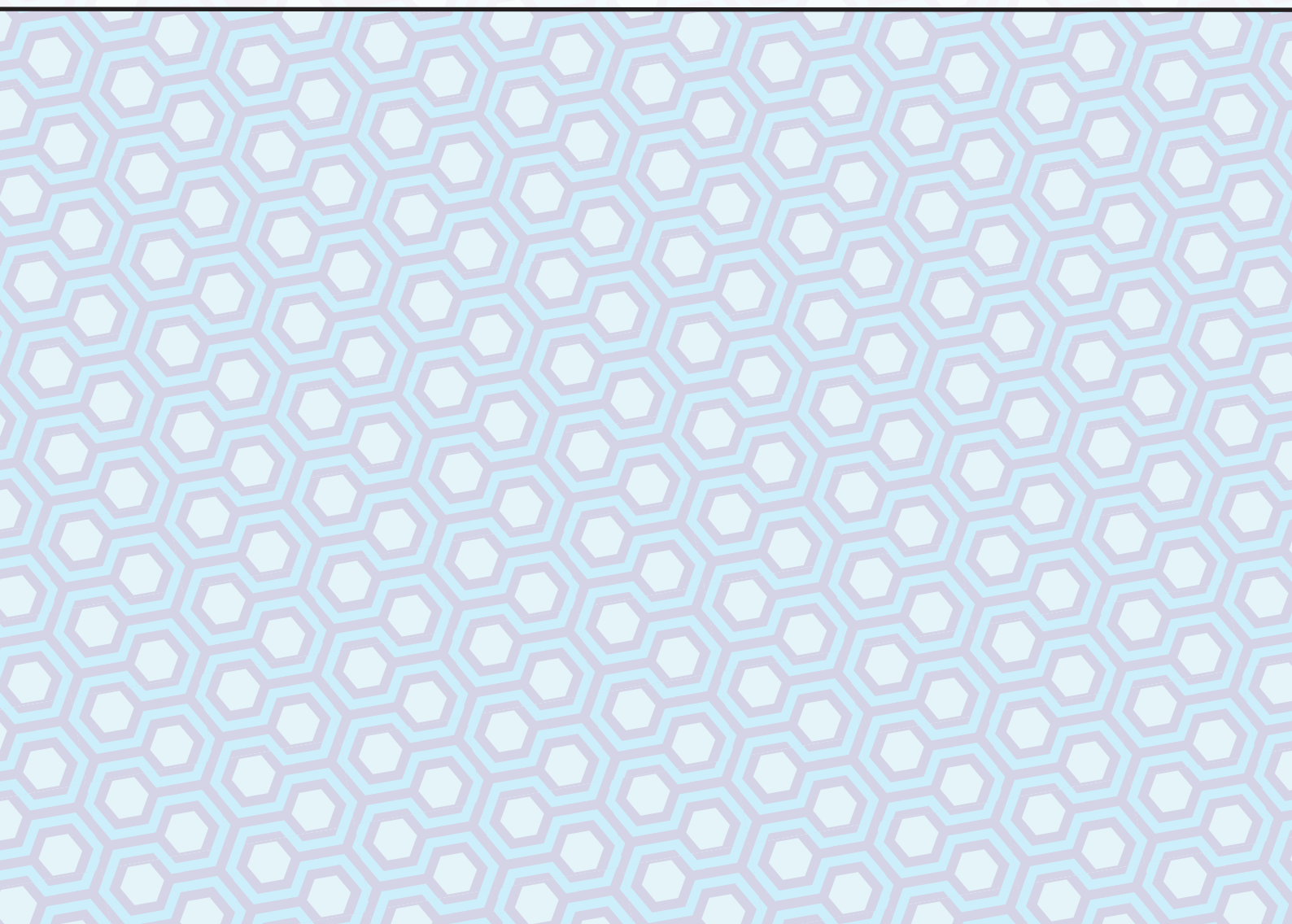
1-D	One-dimensional, geometric setting
2-D	Two-dimensional, a geometric setting
3-D	Three-dimensional, a geometric setting
ALM	Additive layer manufacturing
CT	Compression-tension
DASML	Delft Aerospace Structures and Materials Laboratory, Delft University of Technology, the Netherlands
DIC	Digital image correlation
FE	Finite element
FPS	Frames per second
GUI	Graphical User Interface
NaN	Not-a-number, a numerical dummy variable in MATLAB
SCF	Stress concentration factor(s)
SC	Stress concentration
SLS	Selective laser sintering
VM	Von Mises equivalent





**Part I**

**Project initiation & literature review**







# Chapter 1

## Introduction

Richard Feynman, once said of a flower: “it’s not just beauty at this dimension, at one centimeter; there’s also beauty at smaller dimensions, the inner structure, also the processes.” Feynman, portrayed in Figure 1.1, had an admiration of natural beauty and a powerful belief that the scientific method could add to its many wonders.

Our conceptualizations of ‘cellular solids’ are no exception. The phrase itself stems from mankind’s abstractions of biology. Organic tissues are made up of many microscopic cells, coming together to form millimeter-long organisms like the nematode worm — one is depicted in 1.2 — to the biggest 173 metric ton Blue whale ever observed. Cellular solids as a knowledge area has expanded to include artificial structures whose material is shaped at a sub-structural scale through various manufacturing processes.

Additive manufacturing is a group of fabrication technologies, wherein material is incrementally deposited to the target substrate according to digital instructions. Classical engineering structures are the result of many simplifying functional idealizations. Some are being challenged by new potential to support more intelligent idealizations, partly through the elimination of classical manufacturing constraints. Although additive manufacturing technologies are in their infancy of industry adoption, their impact on cellular solid research has already been felt.

To do away with the engineering design handbooks and to articulate one’s own technology from scratch is a highly enticing technical challenge. Yet to ignore the empirical truths of yesterday is naïve; applying them to new conditions, however, is not. To paraphrase the words of Thomas S. Kuhn,

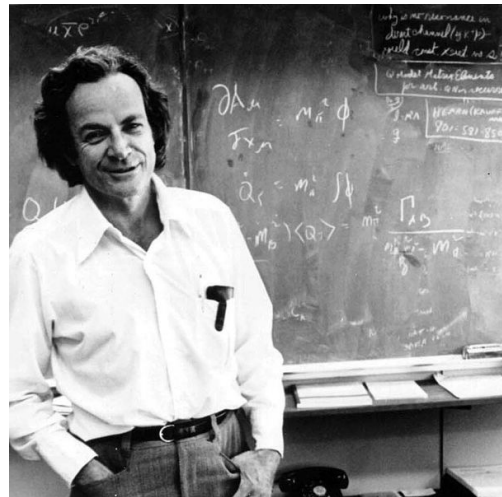


Fig. 1.1 Physics Nobel laureate and best-selling author Richard P. Feynman (Feynman et al., 2018)



Fig. 1.2 Scanning electron micrograph of a root-knot nematode penetrating a tomato root (Agricultural Research Service, 2006).

‘paradigm shifts’ in science are often the result of spotting anomalies against the backdrop of ‘normal science’, meaning that they are at odds with mainstream scientific understanding.

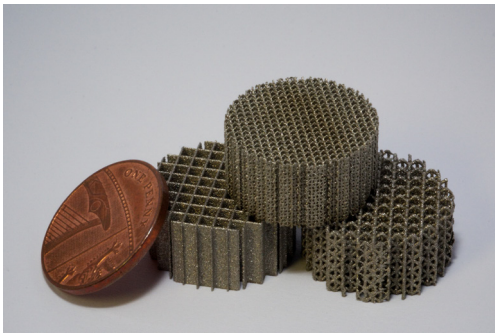


Fig. 1.3 Examples of energy-absorbing blast structures produced with selective laser sintering, an additive manufacturing process with a penny for scale (Harris, 2014).

too does the application of classical stress-reduction design principles. Filleting nodal junctions would surely improve load transfer and distribute stress more evenly. The following question seems justified, therefore: How sensitive are cellular solids to nodal topology?

This thesis is a preliminary diagnostic investigation of this sensitivity. Using stereolithography – an additive manufacturing process – several sets of specimens are fabricated and then tested in a comparative framework. Bioinspired nodal filleting is juxtaposed with the sharp notches that are typical in today’s metamaterials. The aim of the investigation is to support a synthesizing multiscaled discussion of the results, to identify any current short-comings in the scientific understanding of cellular solid mechanics, and to identify possible routes towards a more enlightened glimpse of our world.

Cellular solids such as those in Figure 1.3 comprise of slender struts joined together at nodal intersections. Broadly, the current scientific understanding of their mechanical properties is based on idealized strut behavior on the cell level, where strut lengths are assumed equal to the distance between idealized lattice nodes; the nodal intersections themselves are reduced to one-dimensional entities. At most, they have an implicit stiffness which are articulated as strut boundary conditions.

Yet some of nature’s designs seem to contradict this simplification: strut joints in natural cellular solids are smooth and streamlined. So-

## Chapter 2

# Background information

### 2.1 Looking to nature

Nature has inspired the creation of countless artificial structures. As mankind's powers of observation, conceptual understanding and modeling abilities grow, new layers of the world are peeled into existence.

Natural structures are the harsh result of wearing conditions and or natural selection. For organisms: processes of reproducible mortality in a complex environment. These repeated bouts of success, some of which are more than a million years old, are correspondingly fascinating.

#### 2.1.1 Mattheck's stress-homogenizing curve

The endless fractal geometry of trees; forest boundary profiles; stag antlers; trabecular bone; glacier cavities; and water-eroded rock. According to Claus Mattheck, the unifying theme of the elements in this list is a specific stress-homogenizing topology (Mattheck, 2011). Independent biological growth processes, mechanical wear, and evolution, all play their part in shaping natural structures. The common shape in question can apparently be approximated by a common construction, and its algorithm is defined geometrically in Figures 2.1 a) and b). Mattheck calls this construction his "Method of Tensile Triangles" (Mattheck et al., 2007). For the sake of brevity, it shall henceforth be referred to as Mattheck's curve.

Figure 2.1 a) shows the construction of Mattheck's curve. For a given filleting base length, a circular arc is drawn to bisect the target line. From this new intersection, an arc of radius  $r_1$  equal to half of the length of the newly constructed slope is drawn to create a new bisection. From this new bisection, an arc of radius  $r_2$  can be defined. This pattern continues to the  $n^{\text{th}}$  order, at the discretion of the designer. (Mattheck et al., 2007)

Figure 2.1 b) shows how Mattheck's curve can be applied to joints. The degree of relative loading must be known or assumed, such that a stress-homogenizing topology may be constructed. In this case, the angles subtended by the node and the apex of the curve and each target line are directly proportional

to their relative loads (Mattheck, 2011). This simple method of producing stress-homogenizing notch fillets could be a particularly efficient concept when applied to an iterative finite elements (FE) model where network branches are being stress-homogenized. Mattheck's motivation to teach his non-FE methods seems to be focused on developing intuition and understanding of the natural world and optimization solutions. He has also researched more expensive optimization methods that mimic tree growth in response to its load cases (Mattheck and Haller, 2013).

### 2.1.2 Bone structure and functional grading

To succeed in life, organisms must deal with a multi-variate existence. Correspondingly, their designs are subject many compromises. It is this point that makes the list at the beginning of Section 2.1.1 so important. Mammalian bones are no exception, themselves a systems engineering marvel: bones have varying topologies according to zonal functionality. Functional grading is hereby defined as “the gradual variation in composition and structure over a volume resulting in changes in the mechanical properties of the material” (Birman and Byrd, 2007; Genin et al., 2009). In bone structures, functional grading is the result of addressing stiffness mismatches, usually at bone ends where they interface with others within joints, or with other bodily tissue (Sola et al., 2016).

Generally, mammalian long bones can be divided into three distinctive zones: the epiphyses, the metaphysis and the diaphysis (OpenStax, 2016). Figure 2.2 provides an overview of the three regions. The epiphyses are located at either end of the bone and are made up of cancellous spongy or trabecular bone topologies with porosities in the region of 60-95 [%] (Mullen et al., 2009; Zhang et al., 2016). A large part of their functionality is to transfer load. The trabecular structures allow the bone's base material produced by the body to take on a broad range of stiffnesses, thereby tailoring it to the specific nature of the joint (Hayes and Keaveny, 1993). It should be noted that osteoclasts and osteoblasts are key to understanding bone topology, and are not necessarily well-suited to non-adapting engineering designs.

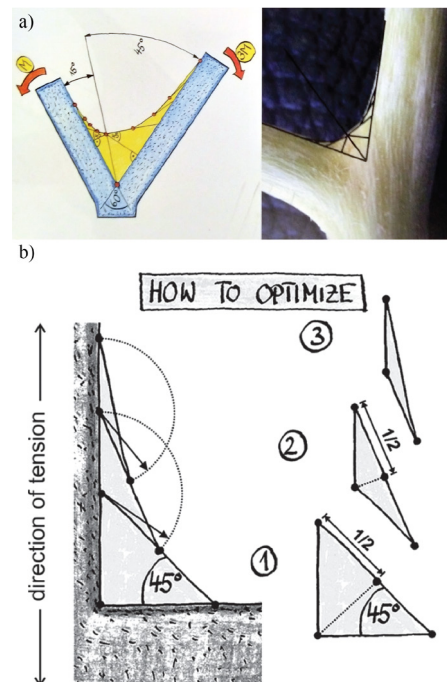


Fig. 2.1 Construction of Mattheck's curve for a) a branch junction where angle ratio  $\theta_1/\theta_2$  is equal the relative load of each branch  $F_1/F_2$  (Mattheck, 2007) and b) for a simple right-angled notch (Mattheck, 2011).

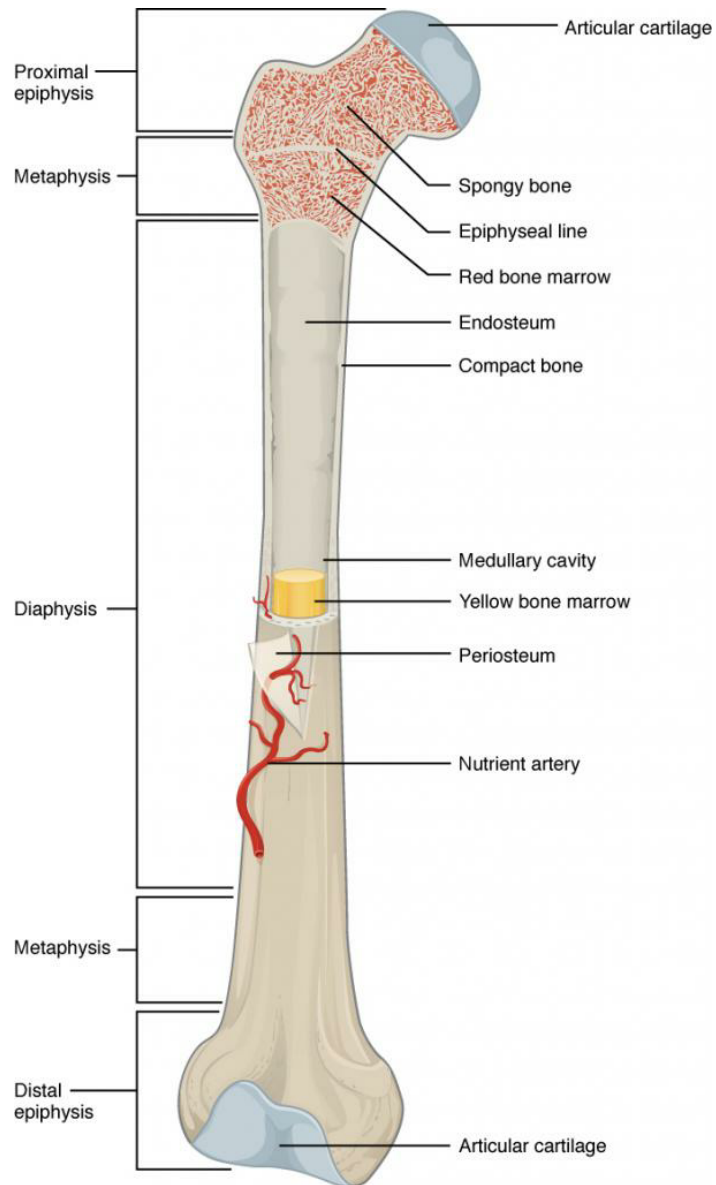


Fig. 2.2 A diagram of a mammalian long bone (OpenStax, 2016)

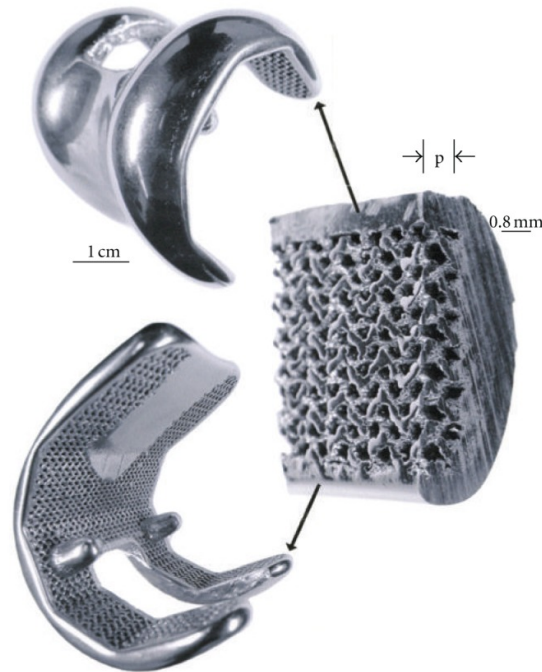


Fig. 2.3 Knee implant prototype with a porous inner structure (Murr et al., 2012)

The biomedical implant industry is undergoing a radical transformation, with some of its latest and most innovative products being designed for bone ‘in-growth’. Conventional solid-cast parts are made from biologically inert metals like Titanium, and are tightly fixed to patient host bones using stiff fasteners and adhesives (Mullen et al., 2009). A well-known mantra in structural analysis and design is that “stiffness attracts load”; an altogether too common result of replacement surgery is that the patient’s neighboring bone atrophies through the natural process of osteoclasts, weakening the joint until failure (Mullen et al., 2009).

Selective laser sintering (SLS), an additive layer manufacturing (ALM) technology, offers the possibility of including porous metamaterial zones in implant design. This intricacy may blur some classical definitions of material and structure by allowing natural and artificial materials to gradually fuse together, forming a lighter ‘living’ joint. According to (Mahmoud and Elbestawi, 2017; Mullen et al., 2009, 2010), SLS and novel design methods show great promise in improving patient recovery time and quality of life. Figure 2.3 shows a photograph of a conceptual design for a human hip implant, realized with SLS (Murr et al., 2012).

Avian long bones are unique in that they are part of the ornithological respiration and circulatory system and have low relative density (O’Connor and Claessens, 2005). It seems that that these added functionalities, together with the evolutionary airborne advantages of flying lightweight, has brought about the avian bone topologies that we recognize as highly distinctive today (Sullivan et al., 2017).

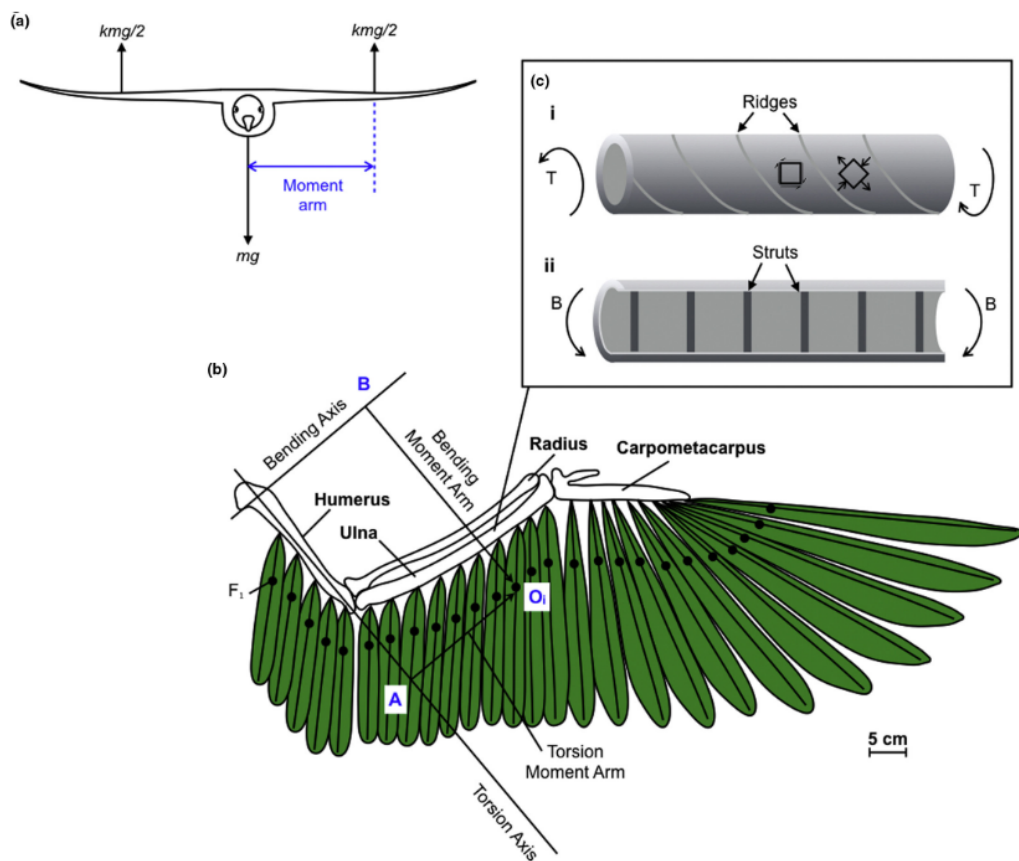


Fig. 2.4 Characteristics of avian long bones (Sullivan et al., 2017).

Studying avian bones more closely reveals that they are much more porous than those of mammalian counterparts, and feature reinforcing struts between the thinner compact bone walls (Sullivan et al., 2017). Figure 2.4 provides an overview of these observations using simple conceptualizations. Figure 2.5 shows a cross-section of the Cape vulture's long bones. *Gyps coprotheres* seems to show off much thinner wall thicknesses as well as internal reinforcement struts that join to the thin walls with streamlined contours than, say, a human's.

## 2.2 Cellular solids

### 2.2.1 Natural cellular solids

One of the best-known and most-cited books on cellular solids is (Gibson and Ashby, 1997). According to their definition, cellular solids are assemblies of smaller sub-structural 'cells', made of connective tissue in the form of struts, ligaments, or membranes (Ashby, 2006). The choice in nomenclature is likely based on the relevant literature available, which was largely biological and botanical according to the references published in that book.

Natural cellular solids are wide-spread, and include wood, cork, plant tissue, animal tissue and bone (Gibson, 2005). As discussed in Section 2.1, many of these examples feature a common stress-reducing topology. Artificial cellular solids are an emerging field. These

man-made designs currently fall into two broad categories, as do natural ones: foams and ordered cellular solid systems. Foams are understood to be random or stochastic in nature, a reflection of their manufacturing process which include stochastic blowing processes (Abueidda et al., 2017; Montemayor et al., 2015). Ordered cells tend to be more anisotropic. Their mechanical properties are considered derivative to cell properties (Gibson and Ashby, 1997), which is explained in Section 2.2.2.

One of the most recognizable natural cellular solids is the honey bee's humble honeycomb. Charles Darwin noted the spectacular ability of bees to shape their wax in order to store food and larvae as efficiently as possible (Darwin, 1859). In 1999, Professor Thomas Hales of the University of Michigan proved outright that "honeycombs provide the least-perimeter to enclose infinitely many regions of unit area in the plane", allowing bees to work quickly and with the fewest resources. His work was, in fact, the answer to the so-called hexagonal honeycomb conjecture that had been bothering mathematicians for millennia (Hales, 2001).

Honeycombs have been used in the aerospace industry for decades, and are commonly featured in composite sandwich panels. They provide excellent vertical stiffness for a small weight penalty,

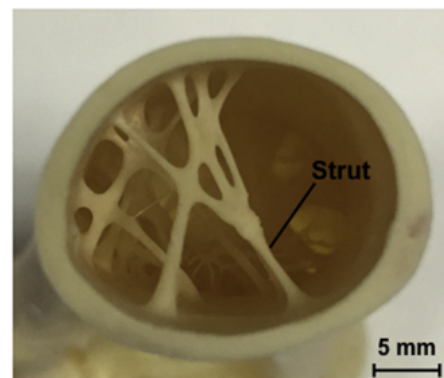


Fig. 2.5 Cross-section of a Cape vulture's (*Gyps coprotheres*) long bone (Sullivan et al., 2017).



allowing high Young's modulus face sheets to be loaded in tension and compression perpendicular to it, resulting in high specific bending stiffnesses. Correspondingly, a great deal is known of their mechanics, making them an excellent candidate for a preliminary study.

### 2.2.2 Cellular solid mechanics

Two broad geometrical categories are often referred to in cellular solid mechanics research. Open cells are structures that have a single enclosed air pocket and tend to be made up of interconnected struts. Closed cells are structures that separate air pockets from each other and tend to be made from membranes. The central importance of these differences is the effect of internal air pressure on the structure. (Gibson and Ashby, 1997)

The scope of this thesis, whose definition is presented in the following Chapter, is principally concerned with open cell structures, as they are more straight-forward to analyze using classical engineering theory.

An apparent trend in the research of cellular solid mechanical properties and characteristics, is to classify their behavior. Broadly, there seem to be two main categories: bending-dominated structures and stretching-dominated structures. Figure 2.6 illustrates their differences. The struts of bending-dominated structures are principally loaded in bending and are depicted by Figure 2.6 a). The struts of stretch-dominated lattices are principally loaded in the axial axis and are depicted in 2.6 9 b).

According to (Deshpande et al., 2001), stretching-dominated structures “offer greater stiffness and strength per unit weight than those in which the dominant mode of deformation is (...) bending”, yet suffer from post-yield softening compared to bending dominated structures due to strut buckling. Bending dominated structures, meanwhile, suffer from a ligament deformation mode that causes more rapid decreases in strength and stiffness for increasing porosity.

The general behavior of cellular solids under compression loading is shown in Figure 2.7. Here, an external load is applied to the system, and is counteracted by the cellular solid's internal loads. Initially, the response is linearly elastic with a constant system deformation rigidity. The structure then begins to soften as the effect of geometric non-linearity and material softening grows.

As the ligaments are loaded beyond their limit and begin to fail, the result is a so-called stress plateau. From there, tissue self-contact dominates the response in a densification regime where the deflection rigidity begins to approach the base material stiffness. (Ashby, 2011).

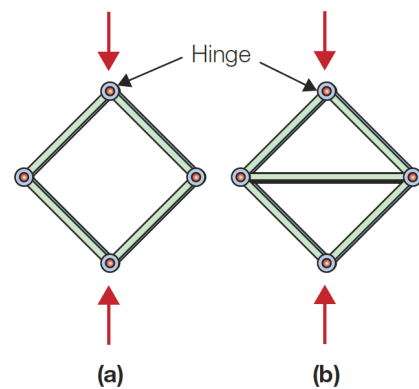


Fig. 2.6 Anecdotal truss-structure examples of a) bending-dominated and b) stretch-dominated lattices (Ashby, 2011)

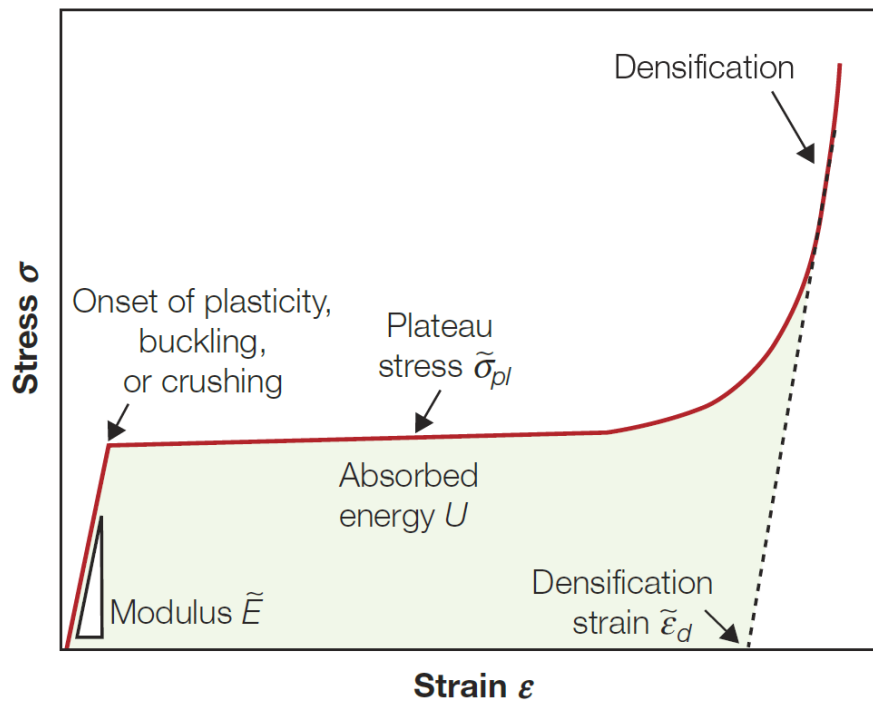


Fig. 2.7 The stress-strain behavior of cellular solids under compression (Ashby, 2011)

The initial linear-elastic response is caused by cell walls flexing elastically under load before non-linear responses dominate the structural response. For two-dimensional (2-D) hexagonal honeycomb solids, Ashby & Gibson have shown that the apparent Young's modulus (referred to by the author as the cellular solid's 'initial deflection rigidity') is a function of its relative density and its aspect ratio. For a regular hexagonal structure, where any strut or cell wall is equal to the other, the relation becomes

$$\frac{k_{idr}}{E_s} = \left(\frac{t}{l}\right)^3 \frac{(1 + \sin(\pi/6))}{\cos^3(\pi/6)} = \frac{4}{\sqrt{3}} \left(\frac{t}{l}\right)^3 \quad (2.1)$$

where  $k_{idr}$  is the initial cellular solid deflection rigidity of a 2-D hexagonal honeycomb cellular solid with wall thickness  $t$ , cell wall length  $l$ , and a material Young's modulus  $E_s$ . Neglecting the size of the node,  $l$  is also the distance between the honeycomb's nodes. (Gibson and Ashby, 1997)

The stress plateau is caused by cell collapse. For 2-D hexagonal honeycomb cellular solids that are loaded uni-axially, this can occur through: elastic buckling in elastomeric materials; the formation of plastic hinges for those with a plastic yield point; and brittle fracture. (Gibson and Ashby, 1997)

### Elastic buckling

The elastic buckling of cell walls in an elastomeric three-dimensional (3-D) honeycomb is considered to occur when the cell walls are able to behave as slender columns which have an Euler buckling load

with critical load

$$P_{\text{crit}} = \frac{n^2 \pi^2 E_s I}{l^2} \quad (2.2)$$

where  $P_{\text{crit}}$  is the critical elastic buckling load,  $0.69^2$  is its end fixity or nodal rotational stiffness,  $E_s$  is the material Young's modulus,  $I$  is the minimum second moment of area, and  $l$  is the cell wall length or inter-nodal distance. A value of 0.69 is assumed for regular hexagonal structures, and is not considered to vary for differences in nodal topology. (Gibson and Ashby, 1997)

### Plastic collapse

Ashby & Gibson's models assume that plastic hinges occur at nodal points. The researchers' model for regular hexagonal structures is an exact

$$\frac{\sigma_{\text{pl}}}{\sigma_{\text{ys}}} = \frac{2}{3} \left( \frac{t}{l} \right)^2, \quad (2.3)$$

where  $\sigma_{\text{pl}}$  is the critical plastic stress,  $\sigma_{\text{ys}}$  is the yield stress of the material,  $t$  is the cell wall thickness, and  $l$  is the cell wall length or inter-nodal distance. (Gibson and Ashby, 1997)

### Brittle fracture

Ashby & Gibson's models assume that brittle fracture occurs near the nodal points. The researchers' model for regular hexagonal structures is defined by

$$\frac{\sigma_{\text{bf}}}{\sigma_{\text{fs}}} = \frac{4}{9} \left( \frac{t}{l} \right)^2, \quad (2.4)$$

where  $\sigma_{\text{bf}}$  is the critical brittle fracture strength or crush strength of the cellular solid,  $\sigma_{\text{fs}}$  is the modulus of rupture,  $t$  is the cell wall thickness, and  $l$  is the cell wall length or inter-nodal distance. The modulus of rupture is usually considered to be roughly 10 [%] larger than the ultimate tensile strength of the material. (Gibson and Ashby, 1997)

### 2.2.3 Cellular solids as crush structures

The gradual crushing through plastic strain and cell wall collapse is reminiscent of Béla Barényi's work at automotive manufacturing giant Daimler-Benz. The Austrian engineer began his career in 1939. By the time he retired in 1972, he had not only invented the concept of the crumple-zone, but a safer steering column and over 2000 other patented designs.

In "Kraftfahrzeug, insbesondere zur Beförderung von Personen" (Motor vehicles, with an emphasis on passenger transport), Barényi challenged the then-age-old adagio that "a safe car must not yield but be stable", arguing instead for the kinetic energy of the crash to be transformed into relatively harmless strain energy (Béla, 1949; Daimler, 2009; Eckermann, 2000). Instead of subjecting the occupants to the full impulse of an energetic collision, the collision is spread out over time, and a

significant portion of the energy into wrecking the material around the passenger cabin. Overall, this reduces the extent to which the occupants are accelerated (or decelerated).

Barényi's idea has been applied to automotive design ever since and led to significant improvements in human welfare. When applied to energy absorption contexts, cellular solids can support the application of crush structure principles to the material level. The mechanics of this behavior have been addressed already. Cellular solids have historically been applied for energy absorption under compression applications. One example is the Apollo 11 landing module in which a sandwich structure was used as a shock-absorber in its landing module (Gibson and Ashby, 1997).

## 2.3 Key engineering concepts

A few key engineering concepts have been identified as essential or important background information which together provides a foundation for the experiment design, analysis, and the subsequent discussion of the results.

### 2.3.1 Plane stress problems

For the case where in-plane forces act on an element, the stress components regarding the out-of-plane component can be assumed equal to zero (Pilkey and Pilkey, 2008). This is the definition of plane stress. The assumption of plane stress reduces the compatibility equations for stress to a simpler set of system of equations in which

$$\frac{\partial \sigma_x}{\partial x} + \frac{\partial \tau_{xy}}{\partial y} + \bar{p}_{Vx} = 0, \quad (2.5)$$

$$\frac{\partial \tau_{xy}}{\partial x} + \frac{\partial \sigma_y}{\partial y} + \bar{p}_{Vy} = 0, \quad (2.6)$$

and

$$\left( \frac{\partial^2}{\partial x^2} + \frac{\partial^2}{\partial y^2} \right) (\sigma_x + \sigma_y) = -(1 + \nu) \left( \frac{\partial f_{Vx}}{\partial x} + \frac{\partial f_{Vy}}{\partial y} \right) \quad (2.7)$$

(Pilkey and Pilkey, 2008). Terms and denote the components of the body forces acting on the unit volume in consideration. If the variation of these forces can be considered zero, then the last constitutive relation reduces to

$$\left( \frac{\partial^2}{\partial x^2} + \frac{\partial^2}{\partial y^2} \right) (\sigma_x + \sigma_y) = 0. \quad (2.8)$$

The above system of equations is that they do not contain any material properties: the state of stress is only related to the geometry of the specimen in question and the load acting on it. The implicit assumption here is that the material has constant material properties that relate strain to stress.

### 2.3.2 Saint-Venant's problem & principle

Saint-Venant's problem was "The task of determining, within the framework of the linear theory of elasticity, the stresses and displacements in an elastic cylinder in equilibrium under the action of loads that arise solely from tractions applied to its plane ends". Circa 1856, Barré Saint-Venant reported his principles on the problem as his semi-inverted solution method, which has since transformed to become known as Saint-Venant's principle. (Horgan and Knowles, 1983)

Saint-Venant's principle is a practical approximation in which the effects of nonlinear stress state responses to changes in geometry and load for distances far enough away from the discrepancies are neglected. This distance is usually defined by the minimum dimension of the geometry being analyzed. According to (Young and Budynas, 2002):

*If a load distribution is replaced by a statically equivalent force system, the distribution of stress throughout the body is possibly altered only near the regions of load application.*

### 2.3.3 Beam structures

Straight beams are slender structures that have: homogeneous material in tension and compression; have an overall curvature at least 10 times its depth; a near-constant cross-sectional area; at least one longitudinal plane of symmetry; loads and reactions acting perpendicularly to the beam axis; and long dimensions relative to its minimum dimension. Furthermore, it does not experience a maximum stress that exceeds the proportional limit of its material. Satisfying these cases seem to yield in a maximum error of 5 [%] for evaluating beam deflections. (Young and Budynas, 2002)

Notch stresses are evaluated by assuming an idealized bending stress distribution, and applying assumed stress concentration factor from classical stress reduction theory (Young and Budynas, 2002).

The effect of shear is considered to be negligible under the above conditions - that is to say, in conditions that respect the idealization of the Euler-Bernoulli beam model (Young and Budynas, 2002). In this beam model, the general differential equation at any cross-section is given by

$$EI \frac{d^2 y_c}{dx^2} = M, \quad (2.9)$$

where  $E$  is the Young's modulus of the material,  $I$  its second moment of area,  $M$  the moment at that cross-section, and  $y_c$  the vertical tip deflection of the centroidal axis. (Young and Budynas, 2002). The latter term is the inverse of the local radius of curvature. This can easily be rearranged to solve for what shall from now be referred to as the apparent bending stiffness, where  $v(x)$  is the strut's vertical deflection function:

$$EI(x) = \frac{M(x)}{\left(\frac{d^2 v(x)}{dx^2}\right)}. \quad (2.10)$$

According to Castigliano's second theorem,

$$y_c = \frac{\partial C}{\partial F}, \quad (2.11)$$

where beam displacement  $y_d$  is also the partial derivative of the complementary energy of flexure  $C$  with respect to a vertical tip load  $F$  (Young and Budynas, 2002).

The relationship between a local cross-section's moment  $M$  and shear force  $S$  is given by the equation

$$S = \frac{dM}{dx}. \quad (2.12)$$

The strain energy of stretching material  $U$  is defined as the work done by that material in absorbing the load  $F$  integrated for the resulting deflection  $dx$  according to the equation

$$U = \int F dx. \quad (2.13)$$

$C$  and  $U$  are related to each-other by totalling as the product of load and deflection at any point of a load-deflection curve.

Overall, the deflection rigidity of a beam can be found by dividing the tip force  $F$  by the tip displacement  $v(x=l)$ . This effectively idealizes the beam as a rotational spring, hence the use of symbol  $k_{dr}$  in the defining equation

$$k_{dr} := \frac{F}{v(x=l)}. \quad (2.14)$$

### 2.3.4 Classical stress-reduction in engineering design

#### Stress concentration factors

Cross-sections that suffer from abrupt changes in their geometry suffer from high stress gradients at those changes. These localizations are known as stress concentration factors (SCF) and are defined by the ratio of the peak stress to some baseline stress (Pilkey and Pilkey, 2008). For linear elastic materials, stress can be considered directly proportional to strain by invoking Hooke's law. This is hereby considered a valid assumption under the provision that the material has not yielded its elasticity.

The reference stress (or strain) is known as the nominal value. Its selection is arbitrary but aims to provide a form factor to engineers so that they can compare designs (Pilkey and Pilkey, 2008). Photoelastic experiments were performed to study the influence of different basic geometries on the resulting stress gradients under load. These findings have since been compiled into various design handbooks in the form of design charts including (Pilkey and Pilkey, 2008; R.B Heywood, 1965; Young and Budynas, 2002).

In this thesis, the stress concentration (SC) in stepped bars are in a plane problem are particularly important. In such designs, the geometric discontinuity of the step provides what is known as a notch stress. According to experimental results, the notch stress is a function of the smaller nominal shaft's size relative to the base shaft, of the applied fillet geometry, and the length of the base. For a circular fillet, these effects can be inferred from Figures 2.8 and 2.9 (Pilkey and Pilkey, 2008). For a relatively large step size (ie.  $d/D$  is large), Figure 2.8 shows that small changes would have little effect; this is especially true for larger values of  $r/d$ . For a large base thickness (ie.  $L$  is large using the figure's nomenclature), Figure 2.9 shows that for an  $r/d$  equal to 1.0, the design is not very sensitive to further variations in geometry.

### Mitigating stress concentrations with fillets

To mitigate the effects of SC – an important consideration for assessing fatigue performance and the goodness of a lightweight design – engineers can grade geometric changes and discontinuities with more streamlined fillet contours. This is especially relevant to improving designs whose main geometric parameters are fixed or highly limited for the application.

Circular fillets are perhaps the most straight-forward type of shoulder fillet. Non-circular contours such as elliptical fillets or Baud's fillet can provide even better reductions of SC. Baud's fillet is based on an idealization of frictionless liquid flowing by gravity from an opening in a tank bottom (Baud, 1934; Pilkey and Pilkey, 2008). Its contour is defined by

$$x = 2r \sin^2 \left( \frac{\theta}{2} \right), \quad (2.15)$$

and

$$y = r \log \left[ \tan \left( \frac{\theta}{2} + \frac{\pi}{4} \right) - \sin(\theta) \right] \quad (2.16)$$

where  $r$  is the base fillet width, and  $\theta$  is the tangent angle of the contour to the  $x$ -axis in radians, as shown in Figure 2.10. Baud's fillet can provide a SCF of near-unity when the appropriate  $r$  is selected. Baud himself recommends it to be equal to the nominal shaft size  $d$  for a stepped shoulder divided by the value of  $\pi$  (Baud, 1934).

### Stress concentrations in cellular solids

Little is known about how the role stress-reduction design might play in cellular solid design. Take nodal filleting as an example. At the beginning of this thesis, only (Dallago et al., 2017) remarked on the possible effects that circular fillets might have on 2-D cellular solid structures. Dallago *et al.* provided a glimpse into the sensitivity of cellular solids to changes in nodal topology via FE and analytical beam models. The initial results were promising, with circular fillets being applied with a radius equal to one half of the strut thickness. Overall, the structural modulus of the material was 'highly sensitive' to the circular fillets, although the differences seemed an obscure 5 [%] for a square

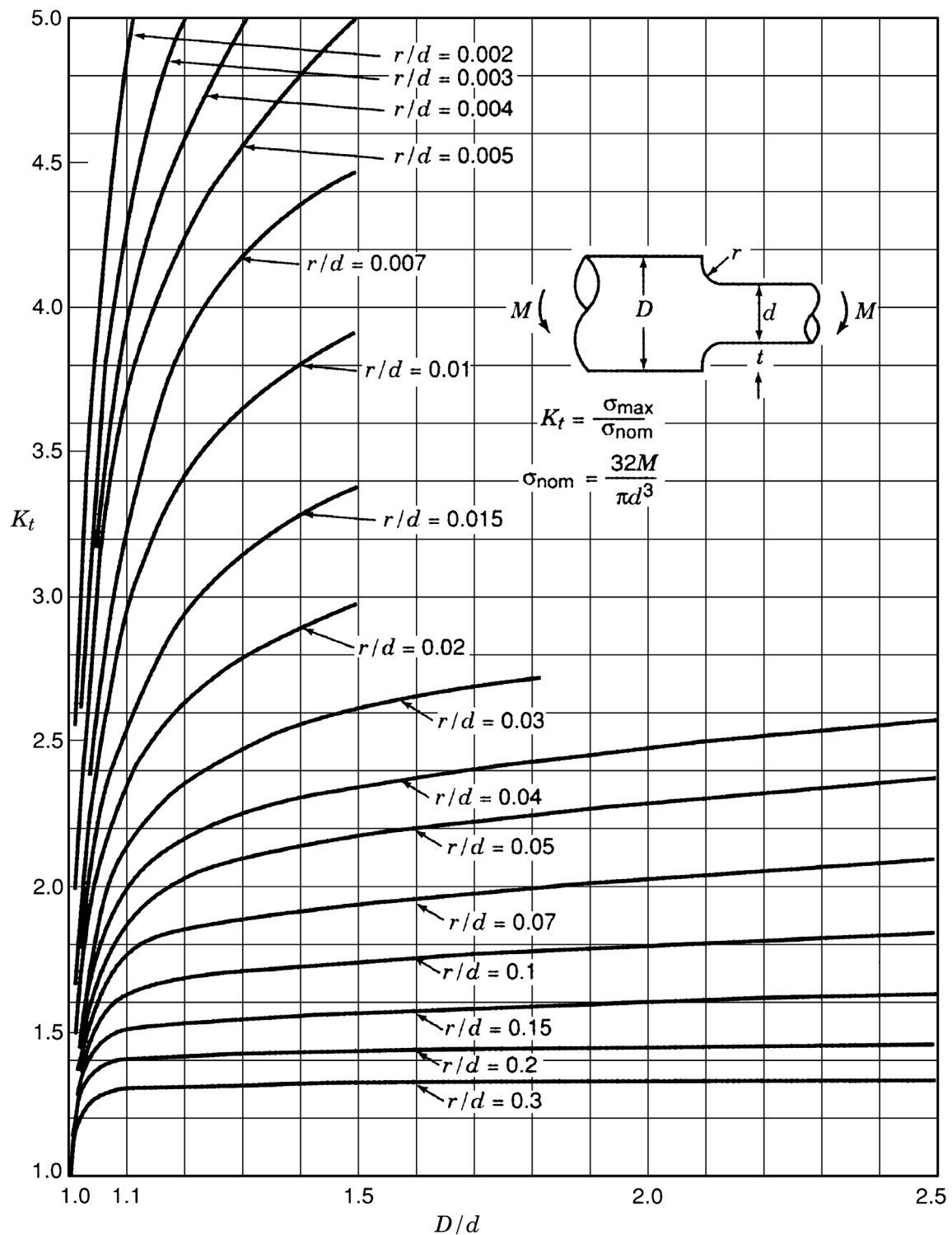


Fig. 2.8 The effect of the stepped shoulder size on stress concentration factor  $K_t$  for a bending stepped bar with a circular fillet according to photoelasticity tests (Pilkey and Pilkey, 2008)



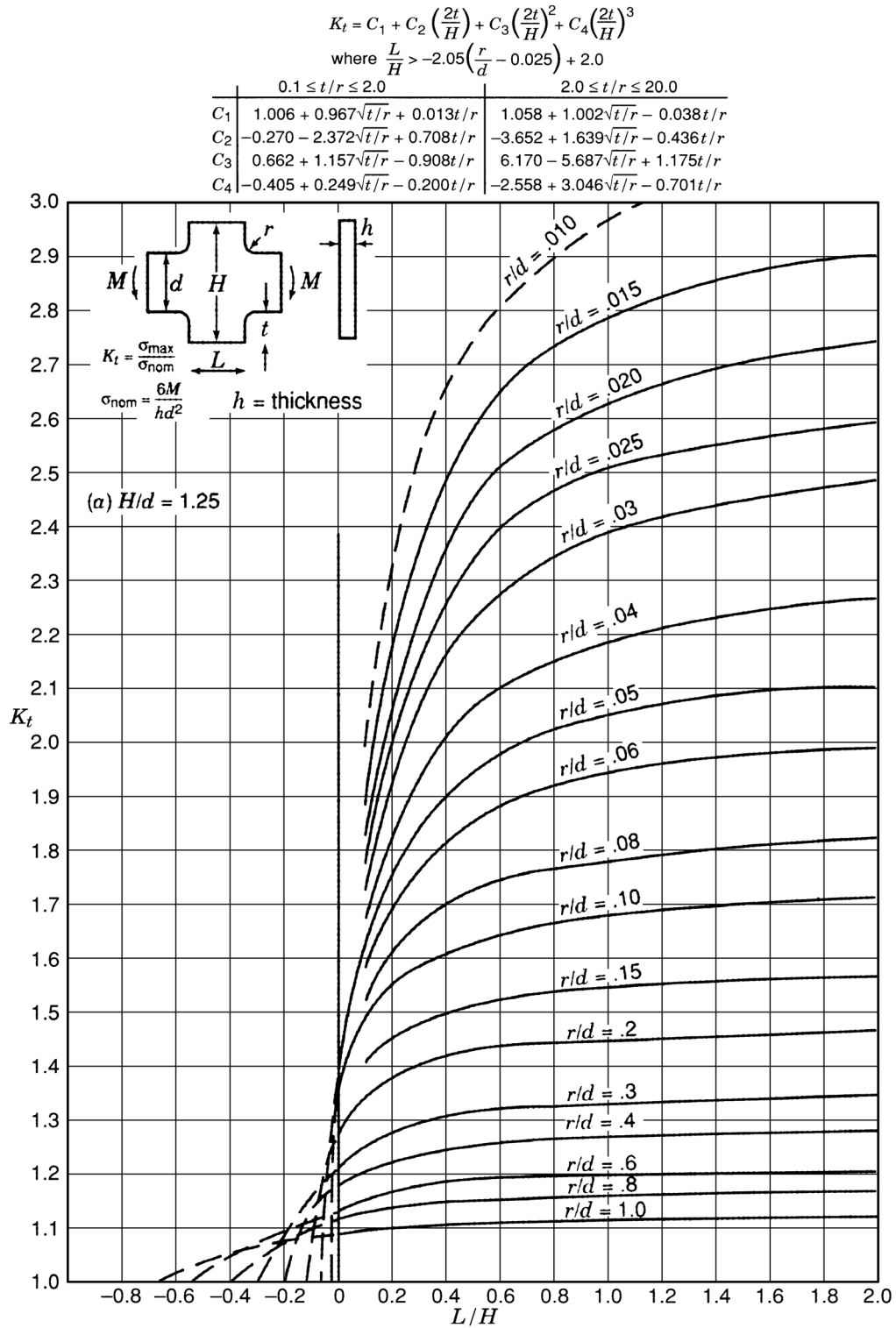


Fig. 2.9 The effect of base thickness on stress concentration factor  $K_t$  for a bending stepped bar with a circular fillet according to photoelasticity tests (Pilkey and Pilkey, 2008)

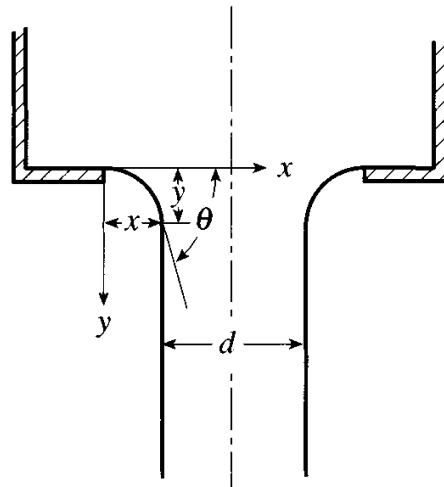


Fig. 2.10 The parametric definition of Baud's curve

lattice. According to the author, “the fillet radius increases the rotational stiffness of the joints, thus making the structure less compliant, but the effect is weaker than that of [the change in thickness]”.

The central problem in the opinion of this author is that FE models suffer in their inability to directly assess the effect of geometric discontinuities on SCFs.

### Design stress-reduction performance

As mentioned earlier in Section 2.3.4, design charts can be found in engineering design handbooks, many of which are knowledge compilations of photoelastic experiments. The experimental specimens were made from translucent material. They had a 2-D form, which is to say that the front and back faces were parallel to each other to form an extrusion of some contour. A series of lights, filters, and other optical equipment allowed scientists to capture diffraction patterns as a result of body forces deforming the specimens. These diffraction patterns were then translated into plane stress gradients over the idealized 2-D surface. The maximum SCF could thus be calculated. An example of fringes showing SC is given in Figure 2.11 for a cantilever specimen with a filleted base. (R.B Heywood, 1965)

Designs were then compared to each other in an iterative engineering process. Stress – or correspondingly strain – can be plotted against load for each specimen along with the ideal nominal stress not affected by SC, as shown in Figure 2.12. The maximum SCF can directly be compared or compared to the ideal situation as an expression of material efficiency.

### 2.3.5 The Von Mises equivalent strain

The Von Mises stress is a fictional stress that combines normal and shear stresses to determine the extent of the material's loading according to the basic Von Mises criterion. The Von Mises equivalent

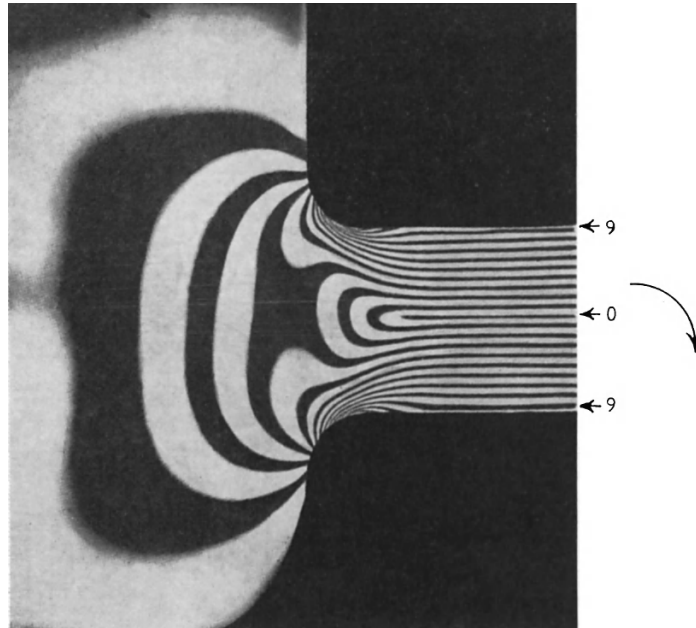


Fig. 2.11 The fringe patterns produced in a photoelastic experiment of a cantilevered specimen with a circular fillet applied to its base (R.B Heywood, 1965)

strain is the corresponding strain, and is often used in FE models to compare material inefficiencies in structural design. The Von Mises equivalent strain is defined by the equation

$$\varepsilon_{VM} := \frac{2}{3} \sqrt{\left( \frac{3}{2} (\varepsilon_{xx}^2 + \varepsilon_{yy}^2 + \varepsilon_{zz}^2) + \frac{3}{4} (\gamma_{xy}^2 + \gamma_{yz}^2 + \gamma_{zx}^2) \right)}, \quad (2.17)$$

where  $\varepsilon_{VM}$  is the equivalent Von Mises strain,  $\varepsilon_{xx}$ ,  $\varepsilon_{yy}$  and  $\varepsilon_{zz}$  are the strains in the  $x$ ,  $y$  and  $z$  directions respectively, and  $\gamma$  is the shear whose subscripts denote in which plane the shear strains are referring.

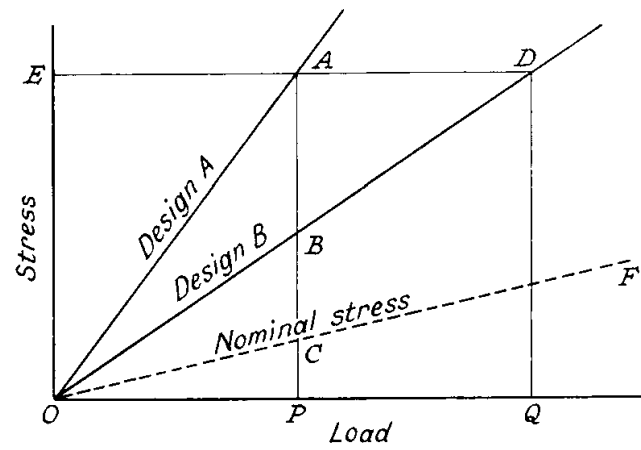


Fig. 2.12 Comparing the stress reduction performance of comparable designs (R.B Heywood, 1965)

## Chapter 3

# Research definition

In Chapter 2, gaps in the scientific understanding of cellular solids were identified. The potential sensitivity of cellular solids to nodal topology was particularly striking. Broadly, researchers believe that the detailed behavior of cell-level mechanics matter little at the larger scale. In the words of metamaterial pioneers Ashby & Gibson, “the single most important structural characteristic of a cellular solid is its relative density” (Gibson and Ashby, 1997). The characteristic cell wall lengths for their mechanical models are equal to the corresponding distance between the idealized lattice nodes regardless of strut thickness. In other words, nodes are reduced to 1-dimensional (1-D) entities who have a position but no explicit stiffness.

Many of nature’s nodes have remarkably streamlined topologies. This curious pattern indicates that nodes might play an important functional role in cellular solid mechanics. This basic observation helped to define the following central research question and the hypotheses presented in Section 3.3.

*What is the effect of nodal topology on cellular solid mechanics?*

### 3.1 Research scope

The above research question is too broad to consider in a single Master of Science thesis. Executing a preliminary diagnostic investigation became its objective. As with many cellular solid studies, the project scope was reduced to consider 2-D structures, though with the goal of scaling the lessons learned to 3-D structures in a synthesizing multiple-scale discussion.

A multiple-scale analysis seemed appropriate to shed as much light on nodal topology as possible. If empirical evidence exists for nodal topology affecting strut mechanical properties, and corroborating evidence supports those findings on a cellular solid level, it could draw a conclusive link between the two.

Comparing and contrasting test specimens seemed an intuitive way to probe the structural significance of nodal topology. In a nod to Heywood’s photoelastic design principles, and to classical

stress-reducing fillet design engineering handbooks, varying nodal topology through filleting became a central idea.

The scope of this project can be defined by the following mission statement:

*Determine the sensitivity of 2-D hexagonal honeycomb cellular solid mechanics to changes in strut base filleting from the nodal and finite cellular solid scales of analysis.*

### 3.2 Author inspiration, opinions and personal biases

The author was particularly inspired by nature's beauty and by apparent patterns in its design. Claus Mattheck's studies of organic and inorganic natural forms, were hugely formative for the author. After researching the internal topology of avian bone, the idea that nodal topology is important became unshakable. It seemed intuitive for the entire structure to become more homogeneously loaded and for it to benefit from shorter streamlined load-paths through the material as a direct result.

There is a general danger in the blind belief of 'utopia'. Pursuing stress homogenization through effective material redistribution might well bring every part of the material to an equivalent loading and for the material efficiency to drastically increase. Indeed, this is one of the core values of an engineer. On the other hand, it might bring every point to an equally critical limit. If every part of the structure is critical, the smallest of flaws or disturbances might cause catastrophe. The rightness of a pure pursuit, therefore, depends greatly on context. It seems to the author that pursuing this knowledge and bringing it together with well-articulated and planned structural weak-points or 'triggers' could be a hugely powerful concept in the general case.

The last idea is partly based on a presentation given by Megan Walker to the author and other colleagues in Calvin Rans' Additive Manufacturing research group on the concept of 'layers of structure for layers of damage'.

### 3.3 Hypotheses

Several hypotheses are put to the test in this thesis. The author's perceptions and guesses were continually re-articulated into the form of the falsifiable – or at least experimentally observable – statements. As this work is a preliminary diagnostic investigation and discussion across multiple scales in cellular solids, it seemed appropriate to reflect this in their classification and articulation as follows.

1. Nodal scale:
  - 1.1 Mass-normalized strut deflection rigidity is unaffected by nodal topology.
  - 1.2 Strut stress fields and their homogenization are unaffected by nodal topology.
  - 1.3 If stress homogenization in a bending structure improves, then that structure will increase in its mass-normalized strut deflection rigidity.

2. Cellular solid scale:

- 2.1 Mass-normalized cellular solid deflection rigidity is unaffected by nodal topology.
- 2.2 Stress homogenization in a cellular solid is unaffected by nodal topology.
- 2.3 If stress homogenization improves, then a cellular solid will increase in its mass-normalized deflection rigidity.
- 2.4 If stress homogenization improves, then a cellular solid will become less sensitive to localized stress gradients and their effects, thereby increasing the height of the so-called stress plateau.







---

**Part II**

**Nodes**

---



# Chapter 4

## Nodal-level methodology

In an attempt to systematically assess the sensitivity of cellular solids to nodal topology, and offer new insights grounded in real experimental data, the multi-scale begins with the investigation on the so-called ‘nodal level’. A number of hypotheses were put forward earlier in Section 3. The process of refining specimen design, designing test procedures, and amassing enough detailed data to justify drawing those insights is detailed in this Chapter. The author has attempted to be up-front about the decisions that were taken - some of which are arbitrary - and to outline how the results presented in Chapter 6 can be reproduced. More specifically, the objective is to reproducibly challenge Hypotheses 1.1 through 1.3.

### 4.1 Specimen design

Two basic specimen types were developed for the nodal level of analysis. Both feature a slender strut whose base is filleted. Slender struts are likened to slender beams, whose definitions are given in Section 2.3.3.

The differences between specimens within a type manifest as distinctive nodal topology, articulated through changes in base filleting. These fillets were inspired by patterns in nature (explained in Section 2.1.1) and by classical engineering design methods (explained in Section 2.3.4). According to Saint-Venant’s principle (explained in Section 2.3.2), the outer portions of the struts can be considered comparable. Should the strut’s deflection rigidity change after controlling for variables like material usage, this may indicate strut sensitivity to nodal topology, thereby disproving Hypothesis 1.1.

Variables pertaining to the design of the specimen itself must be controlled such that specimen comparisons are fair. It is precisely this which is targeted in the proceeding sub-sections of this Section.

For information regarding the detailed specimen fabrication, the reader is directed to (van Helvoort, 2018) for the relevant MATLAB design scripts, printable files, and specimen logs.

Table 4.1 Overview of fillet shapes to be applied to a sharp notch

Fillet shape	Inspiration
No fillet	Baseline design (current state of most cellular solids)
Circular	‘State-of-the-art’ in cellular solid design; straight-forward engineering practice
Mattheck’s fillet	Bioinspired stress-reducing fillet design
Baud’s fillet	Classical stress-reducing streamlined fillet design

#### 4.1.1 Nodal fillet shapes

The first specimen’s nodal topology is the non-filletted node, and represents the baseline design. The remaining shapes are an arbitrary assortment of fillets inspired by different contexts. Descriptive and visual overviews are given in Table 4.1.

The geometric definitions for each fillet are given in Section 2.3.4, where a common geometric parameter is the fillet envelope height, henceforth referred to as  $r$ . The author wished to observe the surface strain of an affected nodal area without significantly disturbing the far-field behavior. An arbitrary balance was struck between fillet dissemblance in the vicinity of the node, and its size relative to the strut, the envelope height was arbitrarily set to  $1/10^{\text{th}}$  of the strut length for all specimens. For the circular fillet, this corresponds to the fillet remaining within the boundary-affected zone implied by Saint-Venant’s principle.

#### 4.1.2 Infinite node specimens

A slender strut is joint to a self-constrained node, designed to be insensitive to small changes in shoulder geometry, in accordance with classical stress reduction theory. In the early stages of this project, the author planned to compare experimental data with Ciomber and Jackel’s FE model results, but later, little added value of this was perceived. Although Ciomber & Jackel’s work was extremely helpful, it should be noted that the selection of base fillets for this thesis was completely coincidental.

A ratio of  $D/d = 10$  was selected to build in a safety margin, and initially to compare results with Ciomber and Jackel’s work directly. Figures 2.8 and 2.9 meanwhile, together indicate that for increasing values of  $r/d$  provide increasingly ‘stable’ values of  $K_t$  which approaches 1 at  $r/d$  approaches 1 for a circular fillet. This stability is assumed for all fillets, meaning that their maximum stress concentrations can be directly compared as a direct function of fillet geometry.

The specimen geometries was defined according to this  $D/d$  ratio, fillet height  $r$ , and strut length  $L$ . In terms of  $r$ ,  $L := 10r$ ,  $D := 10r$ , and  $d := r$ . The final physical dimensions were a function of the available printing volume of a Formlabs Form 2 printer, the printer made available to the author at the Delft Aerospace Structures and Materials Laboratory (DASML). Technical drawings for each specimen can be found in Appendix B.

### 4.1.3 Finite node specimens

The same slender struts and filleted bases are now joint to two perpendicular support struts with the same properties. The finite nodes offer insight into how nodes are affected by being ‘free’, in terms of strut flexibility and load transfer. Their design differs only in the depth of the node base which has become equal to  $r$ . The technical drawings for each specimen can also be found in Appendix B.

## 4.2 Methodology validity

The comparative study aims to shed light on the effect different fillets had within a predefined fillet envelope on strut deflection rigidity, and on its detailed strain behavior in terms of stress concentration visualizations. Unintended changes from specimen to specimen should therefore be accounted or controlled for.

### 4.2.1 Material considerations

The material used to fabricate all specimens was the Formlabs Gray resin V4 using a Formlabs Form 2 SLA printer. The specimens were rinsed and post-cured using the Formlabs Wash and Cure stations respectively. It is assumed that the critical sections to be compared are not thick enough to experience residual stress concentrations, and other material differences as a result of the manufacturing processes used are eliminated using the manufacturer’s advise on specimen treatments. The relatively thick parts of the specimens did not seem to suffer from excessive warping, indicating that this is a reasonable assumption to make. The assumptions were necessary with regard to the thesis scope and time-frame. This is revisited later in Chapter 10.

### 4.2.2 Strut deflection rigidity

Controlling for any changes in second moment of area of the nodal regions would be a poor normalization of strut deflection behavior, as it too-closely relates to the intended variation between specimens. As most of the added material is located at the strut root, which is an area considered to have a complex stress field according the Saint-Venant principle, the second moment of area may not be of key interest if a section is not principally loaded in bending. For this reason, it is assumed that controlling for differences in the second moment of area is not justifiable. Instead, it is proposed to normalize the results according to the material usage of the functional strut (from base to tip). This is done in the processing of results, in Chapter 5.

As it is not possible to load an edge, the strut length hereby receives a more practical definition. The length is based on the functional strut, which is defined as the length of the point of load application to the shoulder location. Determining this precise location and the corresponding strut length is specifically addressed in Section 4.3.2.

### 4.2.3 Nominal strain

To compute the free-boundary stress concentration from the DIC strain field data, a theoretical nominal reference strain must be selected. As slight geometric differences were observed between samples as a result of the fabrication process, it was judged that a fair solution would be to assume that the bending stiffness of the minimum-area cross-section can be modelled by calculating the actual moment of area of the strut tip. Thus, each specimen's strut tip dimensions and effective strut lengths are to be measured using LIN 69332638 digital calipers. From these measurements, the second moment of area is calculated using

$$I_{xx} = \frac{1}{12}bh^3, \quad (4.1)$$

where  $I_{xx}$  is the second moment of area round the  $x$ -axis,  $b$  is the strut width, and  $h$  is the strut's local height, at the minimum-area cross-section.

## 4.3 Experimental design

### 4.3.1 Test goal

The aim of the experiment is to compare the various effects that a tip load causes through the resulting internal shear and moment distribution. The comparison itself will be based on differences in strut displacement, and on the resulting strain fields from two DIC camera setups: one observing the free boundary, and one observing the section-view. The overall setup is functionally similar to old photoelastic experiment designs.

The force is to be applied by a 20kN Zwick 1455 20kN test bench with a 1 [kN] load cell which records the magnitude of the applied load and the tip displacement. Using a permanent marker, the test bench's push-rod is to be coated to leave an impression on each specimen. The distance from this mark to the shoulder base is the (functional) strut length, and is to be measured by the same calipers by temporarily transcribing both locations to a piece of blank paper. The load should act in-plane with the specimen geometry and be made consistent with the help of specimen clamping.

### 4.3.2 Chosen approach

#### Specimen preparation and camera calibration

After fabricating, washing and curing the test specimens – a process detailed in (van Helvoort, 2018) – the specimens were brought to the DASML paint booth. The target surfaces for DIC were spray-painted with a flexible matte white base coat and left to dry for 1 hour. In that time, the DIC setups were calibrated, and the calibration file saved as a reference data file. Then, spare or old specimens were speckled with black paint using swift consistent motions from several distances. Those samples

Table 4.2 Summary of the node-level test program on a Zwick 1455 equipped with a 1 [kN] load cell.

	Infinite node	Finite node
Max. force channel voltage [V]	10	10
Max. force channel force [N]	165	40
Max. force test [N]	150	35
Max. displ. test [mm]	20	20
Strain rate test [mm / min]	0.25	1

were brought the experimental setup, and the speckle patterns were reviewed. The best results were attempted once more, and then applied to actual experiment specimens.

### Experiment methodology

Table 4.2 summarizes the experimental test program that was used for the 20kN Zwick 1455 20kN test bench configured to use a 1 [kN] load cell. It is also available for download in the form of a Zwick 1455 template at (van Helvoort, 2018).

The following method was then applied.

1. The test bench's push rod is coated with a new application of permanent marker.
2. A specimen is placed in the test environment. A small distance of approximately 3 [mm] was left between the specimen and the test bench's point of force application.
3. The DIC cameras are manually set to start taking pictures at a rate of 2 frames per second (FPS) using hardware triggering in VIC Snap 8.
4. The load cell was calibrated to 0 [N].
5. The laboratory climate is recorded in terms of the relative humidity and temperature.
6. The test program described in Table 4.2 was executed.
7. After reaching the maximum force threshold, the DIC cameras were manually controlled to stop taking pictures.
8. The specimen was removed. Return to step 1 until all specimens have been tested. Then proceed to step 8.
9. The imprint left by the coated push-rod is used to measure the effective length of the strut  $l$ , defined previously as the distance between the marker and the specimen shoulder, by paper transcription.





# Chapter 5

## Nodal-level data processing

Unprocessed data in the form of analog sensor spreadsheet logs, and stereoscopic black and white digital images were processed with MATLAB and Correlated Solutions' VIC-3D 8. The reader is referred to (van Helvoort, 2018), where the MATLAB data processing scripts have been made available. Briefly, the underlying theory is presented in this Chapter.

### 5.1 Digital image correlation

#### 5.1.1 System calibration

For each series of experiments, a series of calibration images of the test environment were taken to correlate pixel transformations between images to meaningfully scaled discrete transformations in three dimensions in a process commonly referred to as Digital Image Calibration (DIC) using VIC Snap 8. The analysis of these stereoscopic photographs within VIC Snap 8 provided a reference data file for those specific camera and lighting conditions. For information, the reader is referred to Appendix B.

#### 5.1.2 Appending load cell data to DIC images

The spreadsheet data log for all image sequences includes the force registered by the load cell at each point in time in terms of an analog voltage reading. This data was inspected manually to determine the point at which the specimens first encountered the test machine and thereby defined as the start of each test. Any error here is assumed negligible owing to the low strain rate.

#### 5.1.3 Area of interest

To begin with, an outline of each specimen had to be manually traced using a mouse in the graphical user interface (GUI) of VIC-3D 8. Through a process of trial-and-error, a single unchanging set of subset, step, and strain filter size was selected for each series. An overview of these and other settings specific to VIC-3D 8 is given in Appendix C.

The objective of the trial-and-error process was to reduce output noise, maximize coverage, whilst maintaining sharpness across all specimens. In order to do so, the smoothing area needs to be kept as small as possible in order to observe localized regions of high strain gradients, whilst reducing noise, the risk of aliasing, and non-convergence. Edge data cannot be observed; enough neighboring points need to be present in order to compute strain.

The basic  $x$ -,  $y$ -,  $z$ -,  $xy$ -, and 1- and 2-principal strains were then post-processed to compute the equivalent Von Mises strain, curvature, local in-plane rotation, and velocity for further analysis and exported to MATLAB. This data can be found at (van Helvoort, 2018). The equivalent Von Mises strain is a fictional strain that combines deformations into a single metric, defined earlier by Equation 2.17.

In VIC-3D 8, the initial surface facing the camera was fitted to a flat plane. Data points in which no strain is detected is set to not-a-number (NaN). The  $y$ -axis ( $x = 0$ ) was defined by the position and orientation of the base shoulder geometry in the first image. Thus, the necessary axis transformations were made according to these definitions.

The detailed strain fields can be visualized with standard MATLAB plots like `quiver`, `streamline`, `contour`, and `contourf` plots without further processing.

#### 5.1.4 Blending the DIC data

As the experiment was designed as a plane problem, the two DIC setups are considered to be complementary. Pictures from each DIC setup were taken at slightly different points in time, so results were linearly correlated and interpolated through the logged force output and shoulder location as a time-proxy and space reference respectively. The struts' tip deflections at a given force level can be interpolated from the high frequency sampling of the Zwick 1455 20kN's 1 [kN] load cell's analog output signal.

## 5.2 Apparent flexural rigidity

To compare the apparent flexural rigidity, a tip deflection of 1% of the functional strut length was selected for, where any geometric nonlinearities are assumed negligible. A MATLAB analysis code made openly available at (van Helvoort, 2018) calculated the mean and standard deviation for the vertical displacement at each point along the  $x$ -axis using the `nanmean` and `std` MATLAB functions, both configured to `omitnan`, from the section view DIC setup. The local derivative with respect to  $x$  is taken twice numerically using MATLAB's `diff` function.

The moment distribution as a function of  $x$  is assumed to be a linear distribution increasing from 0 at the strut's effective tip (where the tip load acted) to its root by the equation

$$M(x) = (l - x)F. \quad (5.1)$$

It is important to note that this may not be the precise moment distribution. This will be discussed more fully later.

From the rearranged Bernoulli-Euler law of bending in Equation 2.10, the apparent stiffness of the beam is calculated from its local curvature.

### 5.3 Initial deflection rigidity

The initial deflection rigidity is a simple application of Hooke's law applied to the raw Zwick 1455 20kN's 1 [kN] load cell's analog output signal. A change in force is simply divided by a change in the sip deflection. A deflection of 0.5 to 1.0 [mm] was chosen arbitrarily for all specimens. The deflection rigidity defined earlier in Equation 2.14 then normalized according to the estimated amount of beam material for the real specimen. The normalization is performed according to

$$\overline{k_{dr}} := k_{dr} \frac{V_{nf}}{\Delta V + V_{nf}}. \quad (5.2)$$

### 5.4 Strain concentration visualization

Stress concentrations depend on the problem at hand and on the reference stress in question. For linear-elastic problems, stress concentrations can be calculated by the ratio of a strain over a reference or nominal strain.

Usually, the reference strain would be chosen from an undisturbed but representative location; for no stress concentration, a strain concentration of 1 is conventionally expected. In words, unity represents a return to a 'status-quo' or undisturbed strain distribution. The undisturbed strain field is the idealized strain distribution for regions considered to be unaffected by boundary conditions and load introductions, though exceptions are made for the classical analysis of notches. The identification of these regions is often related to Saint-Venant's principle.

As the moment is a changing distribution in response to shear instead of a pure moment, the author found it most intuitive to reflect this in a nominal strain dependent on  $x$ . The assumption can be reflected on by inspecting the shape of the far-field strain distribution. The Euler-Bernoulli law can then be reformulated to express the nominal strain  $\epsilon_{nom}$  as a function of the distance from the strut's neutral axis  $x$ . To 'level the playing field', the actual printed geometry of each strut tip is used to define the distance of the free surface from the neutral axis  $y$ , which is assumed to be  $h$ , the height of the beam. The second moment of area becomes a constant and is easily calculated using the basic equation for a rectangular section.

$$\epsilon_{nom,x}(x) = -y \left( \frac{d^2 v(x)}{dx^2} \right) = -y \frac{M(x)}{EI} \quad (5.3)$$

The computation of the strain concentration distribution  $K_{t,x}(x)$  becomes:

$$K_{t,x}(x) = \frac{\epsilon_x(x)}{\epsilon_{\text{nom},x}(x)}, \quad (5.4)$$

and the maximum stress concentration  $K_{t,\text{max}}$  can be found according to:

$$K_{t,\text{max}} = \max(K_{t,x}(x)). \quad (5.5)$$

## Chapter 6

# Nodal-level results

Two specimen archetypes whose detailed designs are explained more thoroughly in Chapter 4 were tested in an experimental setup under quasi-static loading conditions. The first archetype represented an ‘infinite node’ and is like a cantilevered beam plane problem. The second archetype had geometrically identical strut and fillet geometries but had a truncated base in the form of two adjoining struts. This second archetype represented a ‘finite node’ and is more like an actual cellular solid node.

The specimen masses are given in Table 6.1, having been weighed with a Mettler AE 1666 digital scale. The specimen projected volumes are given in Table 6.2, using the Formlabs PreForm software estimation from the input stereolithography file. An overview of each infinite-node specimen’s geometries in which the LIN 69332638 digital calipers were used is provided in Table 6.3, and an overview of each finite-node specimen’s geometries in which the same calipers were used is provided in Table 6.4.

Table 6.1 An overview of nodal specimen masses

Fillet design	Specimen masses pm 0.0005 [g]	
	Infinite node	Finite node
No fillet	100.268	7.353
Circular	99.130	7.537
Mattheck’s fillet	100.701	7.799
Baud’s fillet	100.207	7.931

Of interest is the overall strut deflection rigidity. This performance parameter essentially idealizes the strut as a torsional spring. If this rigidity varies according to fillet shape, after controlling and normalizing the results, this would directly challenge Hypothesis 1.1.

By analyzing local curvature along the strut length, the apparent stiffness can be estimated by invoking the Euler-Bernoulli law. This process will help identify preliminary explanations for how the fillet shapes affect strut rigidity, and which areas are particularly significant.

Table 6.2 An overview of nodal specimen volumes

Fillet design	Specimen volumes $\pm 0.005$ [ml]	
	Infinite node	Finite node
No fillet	83.02	6.07
Circular	83.11	6.16
Mattheck's fillet	83.36	6.41
Baud's fillet	83.46	6.51

Table 6.3 An overview of the infinite-node specimen geometric parameters

Fillet design	Geometric parameter lengths $\pm 0.010$ [mm]		
	Tip height ( $h$ )	Tip width ( $b$ )	Strut length ( $l$ )
No fillet	4.51	9.89	39.53
Circular	4.61	10.02	42.02
Mattheck's fillet	4.51	9.78	40.06
Baud's fillet	4.77	10.00	39.00

Table 6.4 An overview of the finite-node specimen geometric parameters

Fillet design	Geometric parameter lengths $\pm 0.010$ [mm]		
	Tip height ( $h$ )	Tip width ( $b$ )	Strut length ( $L$ )
No fillet	4.62	10.07	40.16
Circular	4.62	10.09	40.16
Mattheck's fillet	4.66	10.02	40.16
Baud's fillet	4.72	10.02	40.16

By comparing and contrasting the apparent strut stiffness for every beam section with the theoretical stiffness of each strut, how anomalies from this well-understood backdrop can be identified and hopefully explained later in the synthesizing discussion, along with a comparison of free boundary strain distributions, stress concentration, and photoelastic-like section views.

## 6.1 Infinite node specimens

The infinite node aims to present the effects of a strut base fillet independent of other geometric parameters.

### 6.1.1 Strut deflection rigidity

Under quasi-static loading conditions, the specimens differed in their strut deflection rigidity. This is clearly seen in the unprocessed test bench results, shown in Figure 6.1, and remain after normalizing

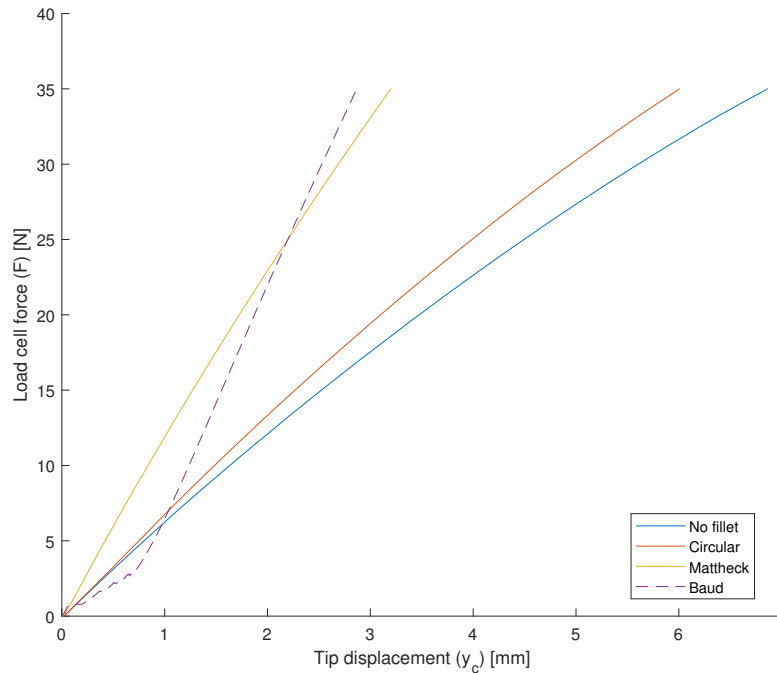


Fig. 6.1 The unprocessed force-displacement results for the infinite node specimens

by the projected strut and fillet material volume, as defined by Equation 5.2 in Chapter 5. The normalized rigidity of each specimen is compared graphically in Figure 6.2. For a given displacement, it seems that significant differences in force is required as a function of the specimen themselves.

The Baud-filletted infinite node specimen, represented by a dashed line in Figure 6.1, rotated in its clamp during the experiment, unbeknownst to the author at the time. This is clearly seen by comparing the first and last photographs of each specimen. The Baud-filletted infinite node suffers from rotational blurring in Figure 6.3d as compared to 6.3a, for example, which did not rotate. Although this rotation may seem small, it is still considered a significant systematic error. The displacement occurred randomly in the initial stages of the experiment according to the force-displacement output, and knowing that the strain rate was constant. This movement significantly affected the specimen's orientation with respect to the applied load. For this reason, these results cannot be considered truly representative, hence the dashed line.

### 6.1.2 Strut deflection analysis

The strut displacement pattern of each specimen for a tip deflection of 1 [%] of its functional length is shown in Figure 6.4. According to theory outlined in Chapter 5, it was differentiated twice with respect to  $x$  to find the local curvature, and correspondingly its apparent stiffness through the Euler-Bernoulli bending law and assuming a linear moment distribution from tip to base. The moment distributions are shown in Figure 6.5. The resulting apparent stiffness distributions are shown in Figure 6.6.

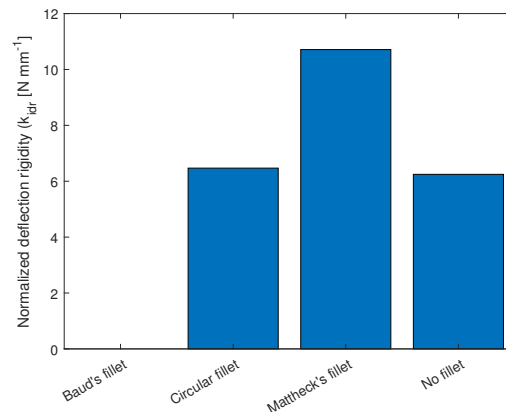


Fig. 6.2 The initial deflection rigidities for the infinite nodal specimens

In the region of the node, St. Venant's principle implies that the stress field in these regions are subject to highly complex strain fields; they are not easily modelled. The strain fields of the specimens in this area may thus give clues as to how the flexural rigidity of the beam is actually affected by the fillet.

### 6.1.3 Strut free boundary analysis

The specimen average free boundary principle strain for every point in  $x$  is shown in Figure 6.7 for a tip deflection of 1 [%], and the corresponding stress SCF distribution as defined in Chapter 5 is shown in Figure 6.8.

The nodal regions of both Figures 6.7 and 6.8 are distinctive from each other, and their far-fields converge to comparable principle strain levels and SCF values respectively. The relative shape of both distributions were seen to be similar throughout each trial. It is thought that for these larger strut deflections, structural non-linearities upset the pattern, and are thus not representative for the general linear case.

According to Figure 6.8, the stress concentration factors vary greatly from specimen to specimen in terms of magnitude and location. It seems that the un-filletted baseline experienced an observable maximum SCF of 1.6 [-] at a position of 3.5 [mm] from the notch. The SCF at the notch itself was not able to be computed owing to the nature of DIC. The circular- and Mattheck-filletted nodes, experience near-zero SCFs at the notch: the maximum SCF of the circular-filletted node was found to be 1.2 [-] at a position of 4.1 [mm] from the notch; the SCF of the Mattheck-fillet was roughly unity for much of its length, and was not sufficiently localized to be considered a maximum. The area around the notch had a very low stress concentration, however.



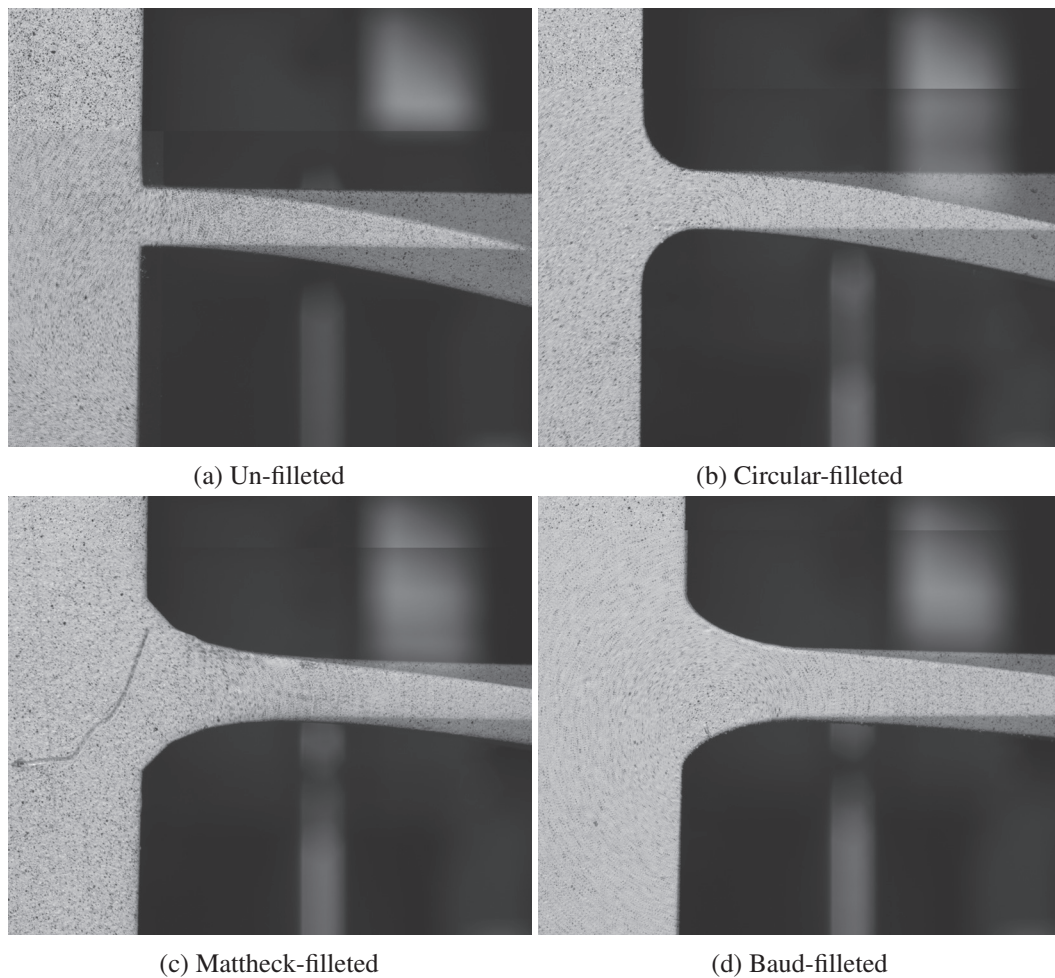


Fig. 6.3 A review of the rotations of the infinite-node specimens: from initial to final deflection. Notice how 6.3d has a base that is affected by a radial blur and has edge 'ghosting'. This indicates slippage in the clamp.

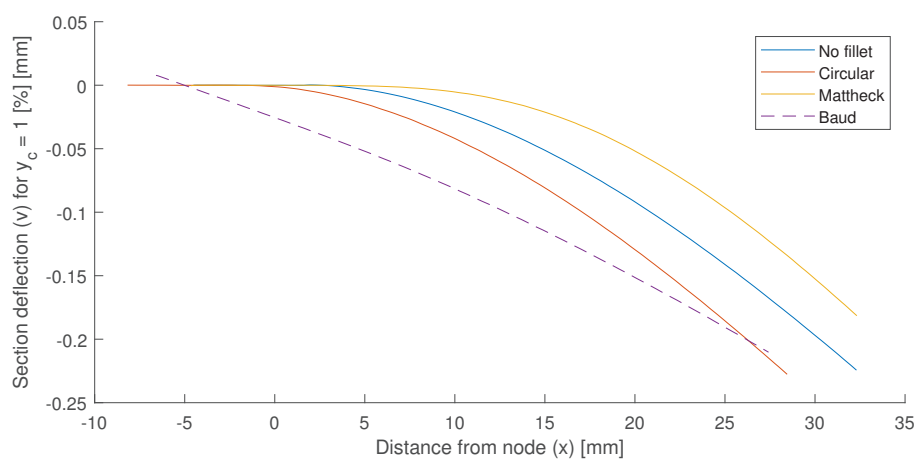


Fig. 6.4 Strut deformation for 1 [%] tip deflection

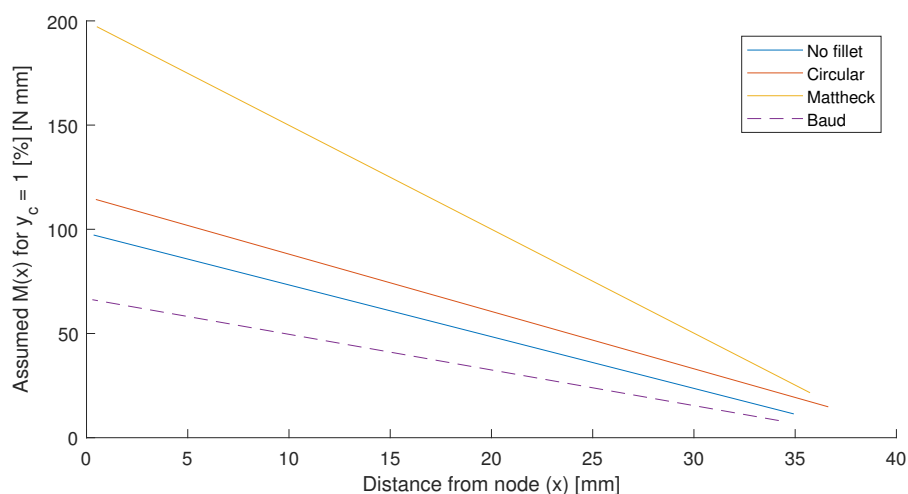


Fig. 6.5 Strut deformation for 1 [%] tip deflection

#### 6.1.4 Plane strain section analysis

In the previous section, obvious differences in apparent stiffness were observed in the nodal region. The complexity of the stress field in the region of the node is difficult to assess quantitatively owing to the complex nature of local stress fields. This complexity is implied in Saint-Venant's principle. Applying the principle to the un-filletted node would give a compromised region defined by inequality  $x < 4.5$  [mm]. This was thus arbitrarily defined as the 'nodal region' for all specimens.

For a tip deflection of 1 [%], the  $x$ -,  $y$ - and  $xy$ - strains were plotted in Figure 6.9 and equivalent Von Mises strains in Figure 6.10. It seems that qualitatively, Mattheck and Baud fillets have a much more homogeneous strain distributions along their free boundaries than the un- and circular-filletted specimens. It seems too that the  $x$ - and  $y$ - strains are much lower. It seems as though the nodal region for the Mattheck- and Baud-filletted nodes were less affected by bending. The reader is reminded about the earlier concern with the Baud-filletted node.

#### 6.1.5 Equivalent strut length calculations

The length of equivalent strut models (where the far-field stiffness was assumed constant throughout the strut) were calculated using standard analytical expressions for a cantilevered beam. Taking the quotient of this theoretical strut length and the known strut length gives an apparent effective length multiplier. The effective lengths and the resulting multiplier of each specimen is shown in Table 6.5, along with their finite counterparts.

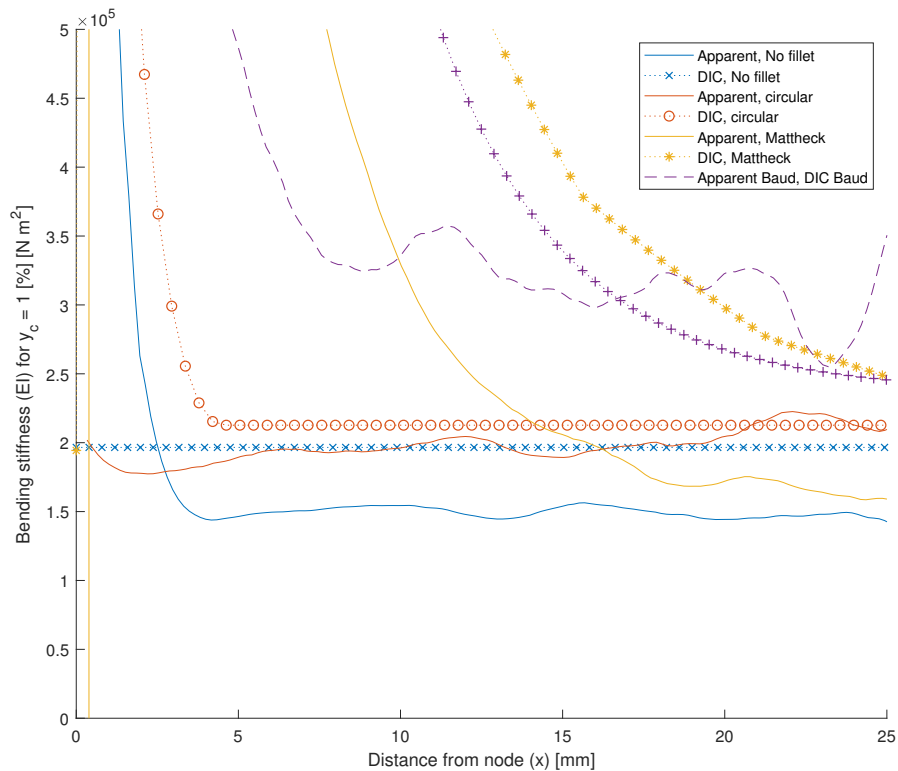


Fig. 6.6 Apparent bending stiffness for 1 [%] tip deflection

## 6.2 Finite node specimens

The same methods and processes were applied to the finite-node specimens, which are displayed in Figures 6.11 through 6.19. Much of the above commentary applies to the finite node specimens as well, though some important differences do exist. Note that the finite node effective lengths have already been given in Table 6.5.

It is no surprise that the deflection rigidities of the finite nodes are less stiff than their infinite counterparts. Less base material is present, and the node itself is freer to rotate. The underlying concept of testing such a configuration - despite being arbitrary - is that it is more representative of a cellular solid node. Whereas the infinite strut highlights differences in structural performance which is independent from certain geometric parameters, it is hoped that a direct comparison with the equivalent finite struts can shine some new light on the effect of nodal topology on cellular solids.

This time, each specimen was well-tested. The observable stress concentration distribution for a strut deflection of 1 [%] is shown in Figure 6.17. It is clear that the maximum stress concentrations suffered by the baseline un-filleted and circular-filleted specimens suffered much more from localized effects in this region. This is in very stark contrast to the profiles that reduce these effects: the Baud-

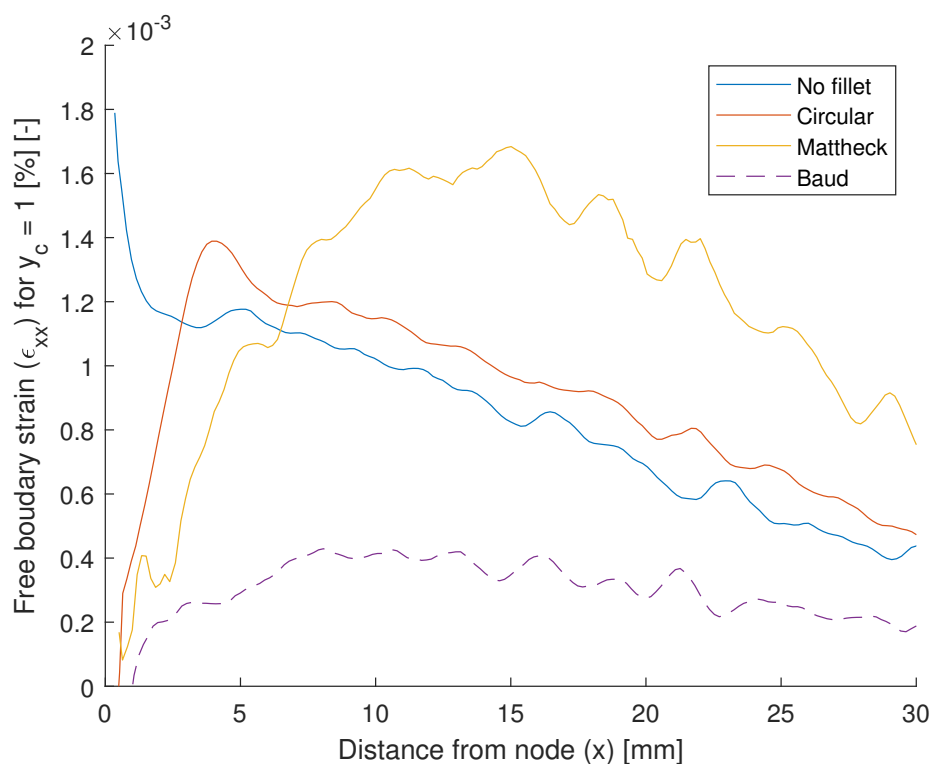


Fig. 6.7 Major principal strain for 1 [%] tip deflection

and Mattheck-filletted specimens were seemingly successful in homogenizing stress throughout the specimen.

Another important difference is how the strain fields developed in the nodal region, which may explain some of the previous effects, although the link should only be drawn in the synthesizing discussion of Chapter 10. Regardless, the patterns are certainly more acute with the finite nodes: the various strain distributions in the nodal regions have much higher gradients, as can be seen in Figure 6.18. The un-filletted node suffers especially from ‘hot-spots’, and this is especially apparent for  $\epsilon_{xy}$ , and for  $\epsilon_{VM}$  in Figure 6.19, whereas the Mattheck- and Baud-filletted nodes seem to have contours that adopt the shape of their ‘container’: the free boundary shape. For this reason, the much

Table 6.5 An overview of nodal specimen effective strut lengths

Fillet design	Specimen effective strut lengths ( $l_{eff}$ ) [mm]	
	Infinite node	Finite node
No fillet	45.49	52.51
Circular	45.53	49.91
Mattheck’s fillet	36.50	45.08
Baud’s fillet	38.67	44.74

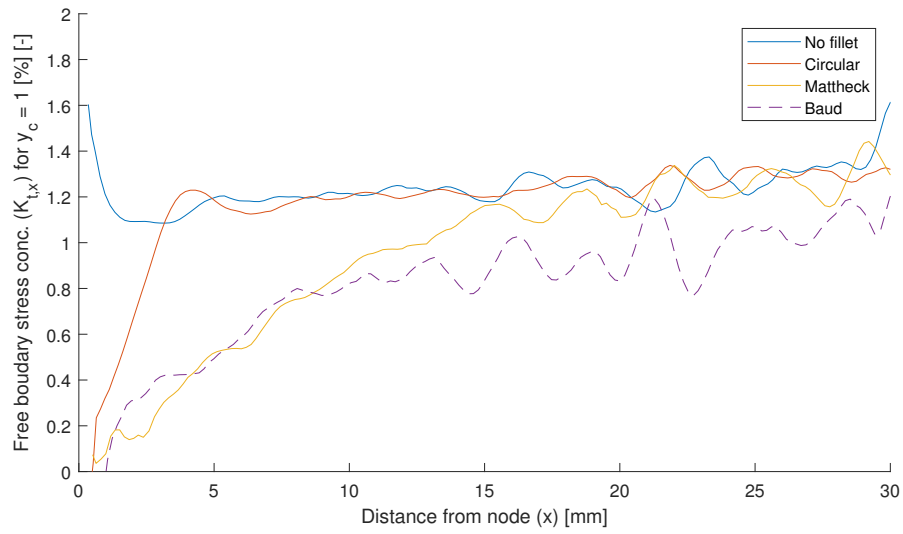


Fig. 6.8 Major principal stress concentration for 1 % tip deflection

of the impending discussion is based around flow analogies to explain the mysterious nature of cellular solid nodes.

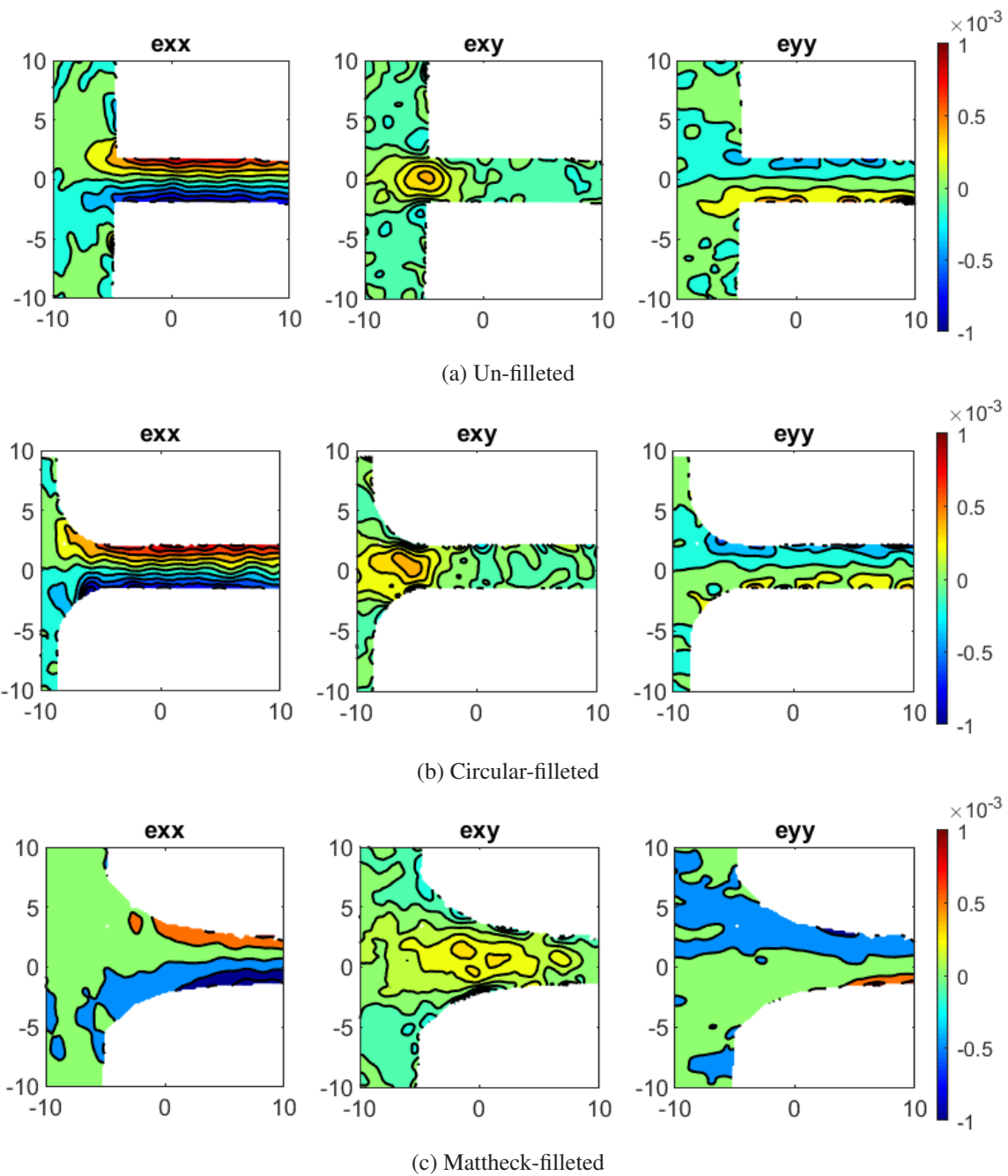


Fig. 6.9 The infinite node internal strains for a 1 [%] tip deflection

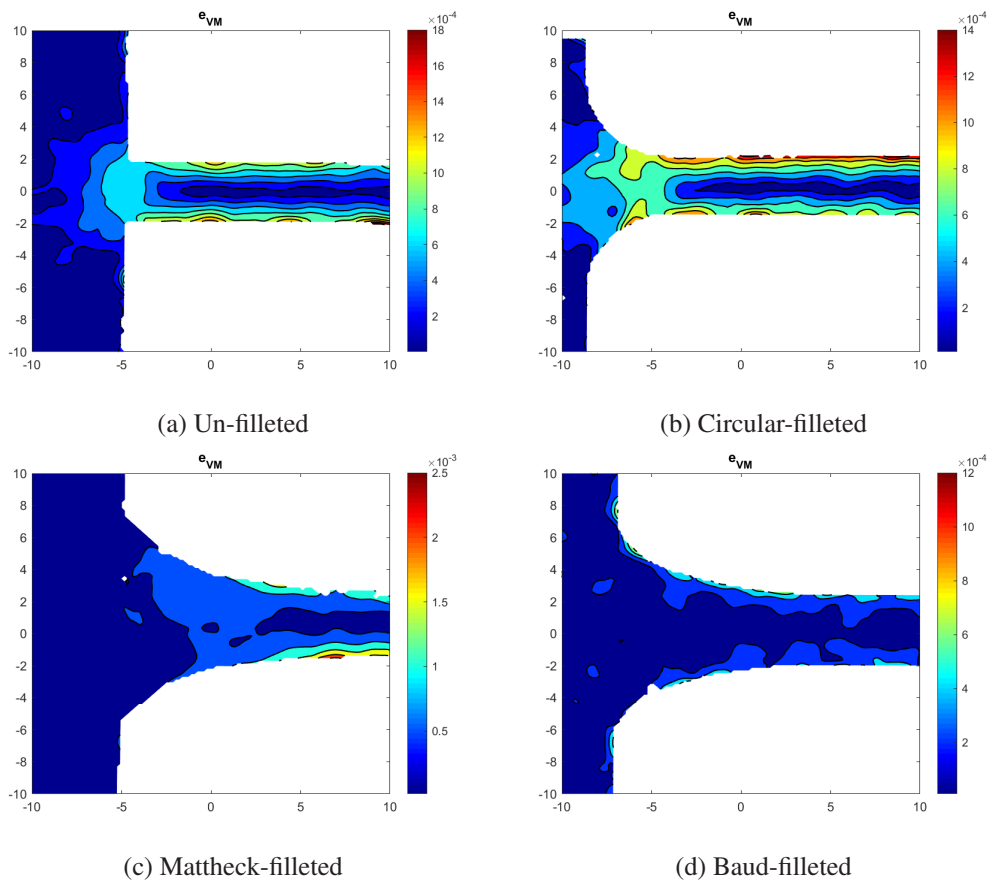


Fig. 6.10 The infinite node equivalent Von Mises strains for a 1 [%] tip deflection

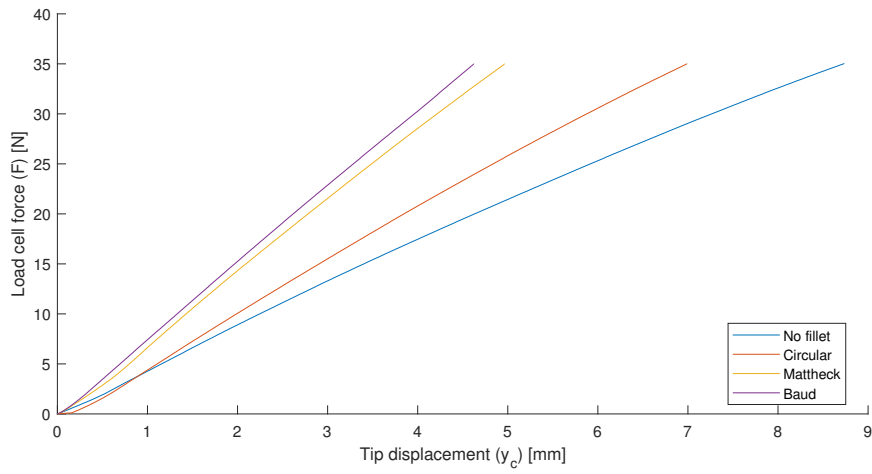


Fig. 6.11 The unprocessed force-displacement results for the finite node specimens

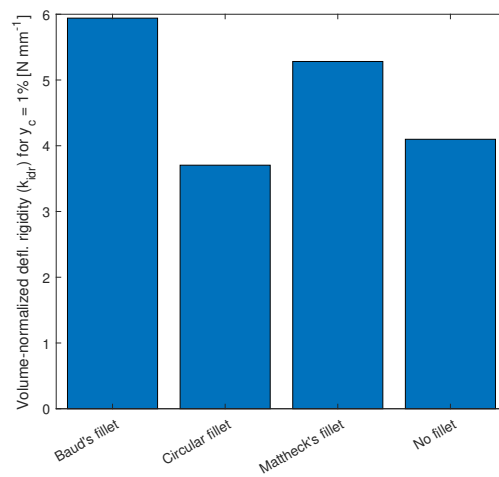


Fig. 6.12 The initial deflection rigidities for the finite nodal specimens

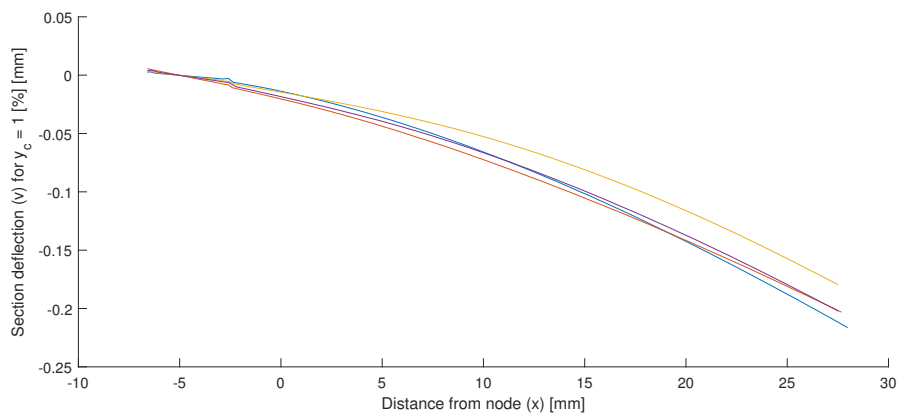


Fig. 6.13 Strut deformation for 1 [%] tip deflection



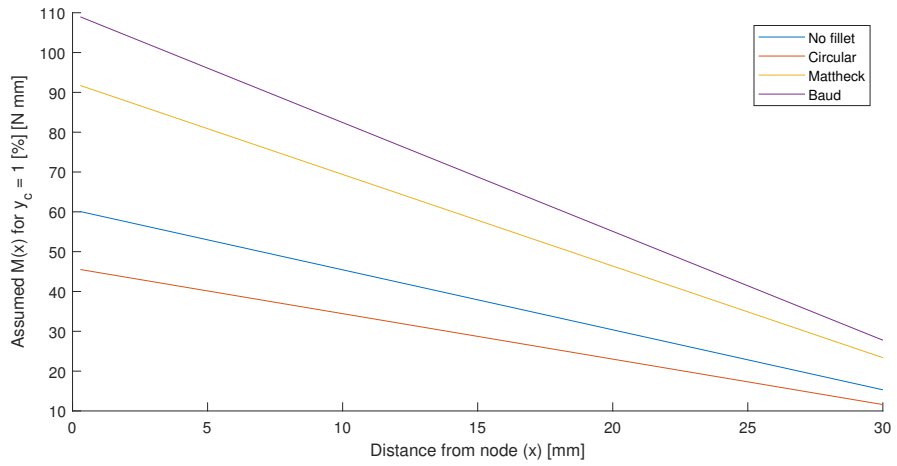


Fig. 6.14 Strut deformation for 1 [%] tip deflection

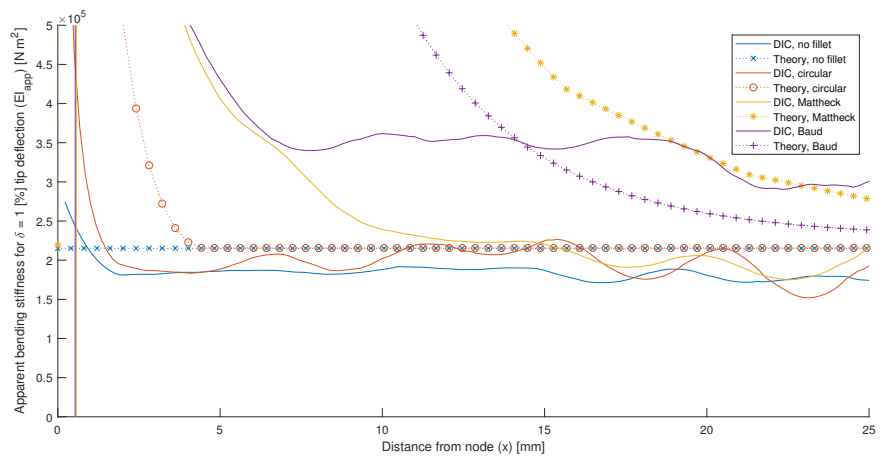


Fig. 6.15 Apparent bending stiffness for 1 [%] tip deflection

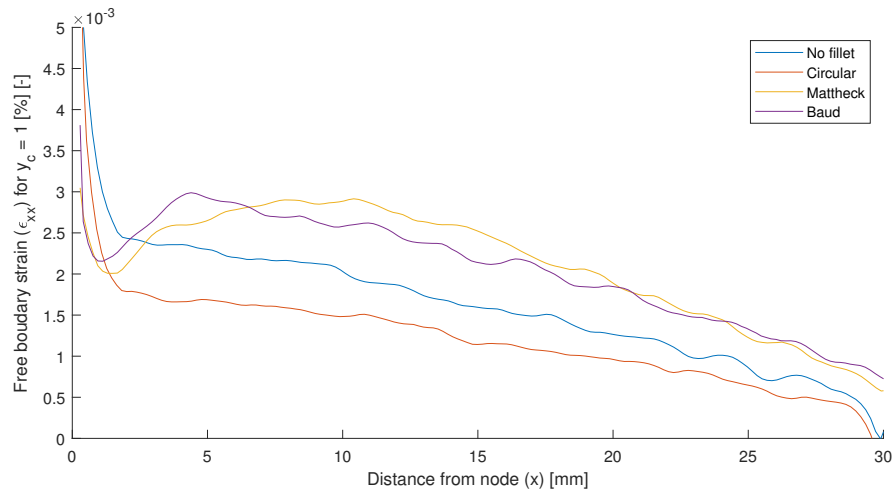


Fig. 6.16 Major principal strain for 1 [%] tip deflection

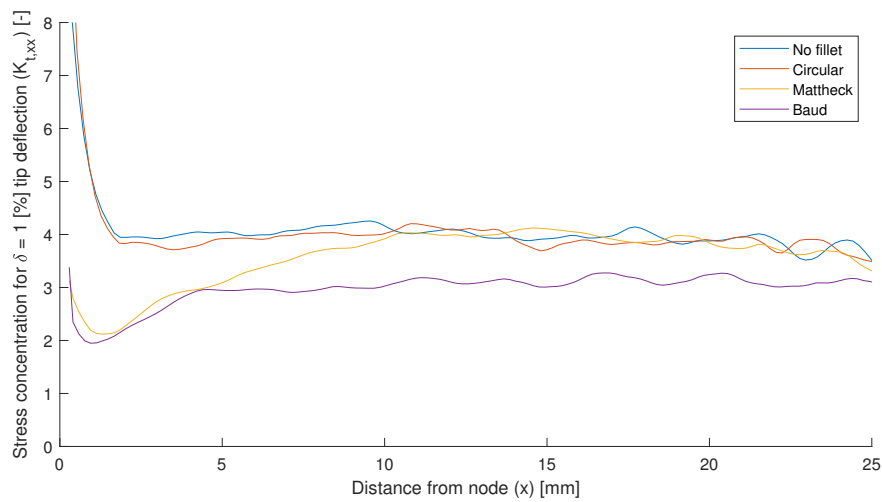


Fig. 6.17 Major principal stress concentration for 1 % tip deflection

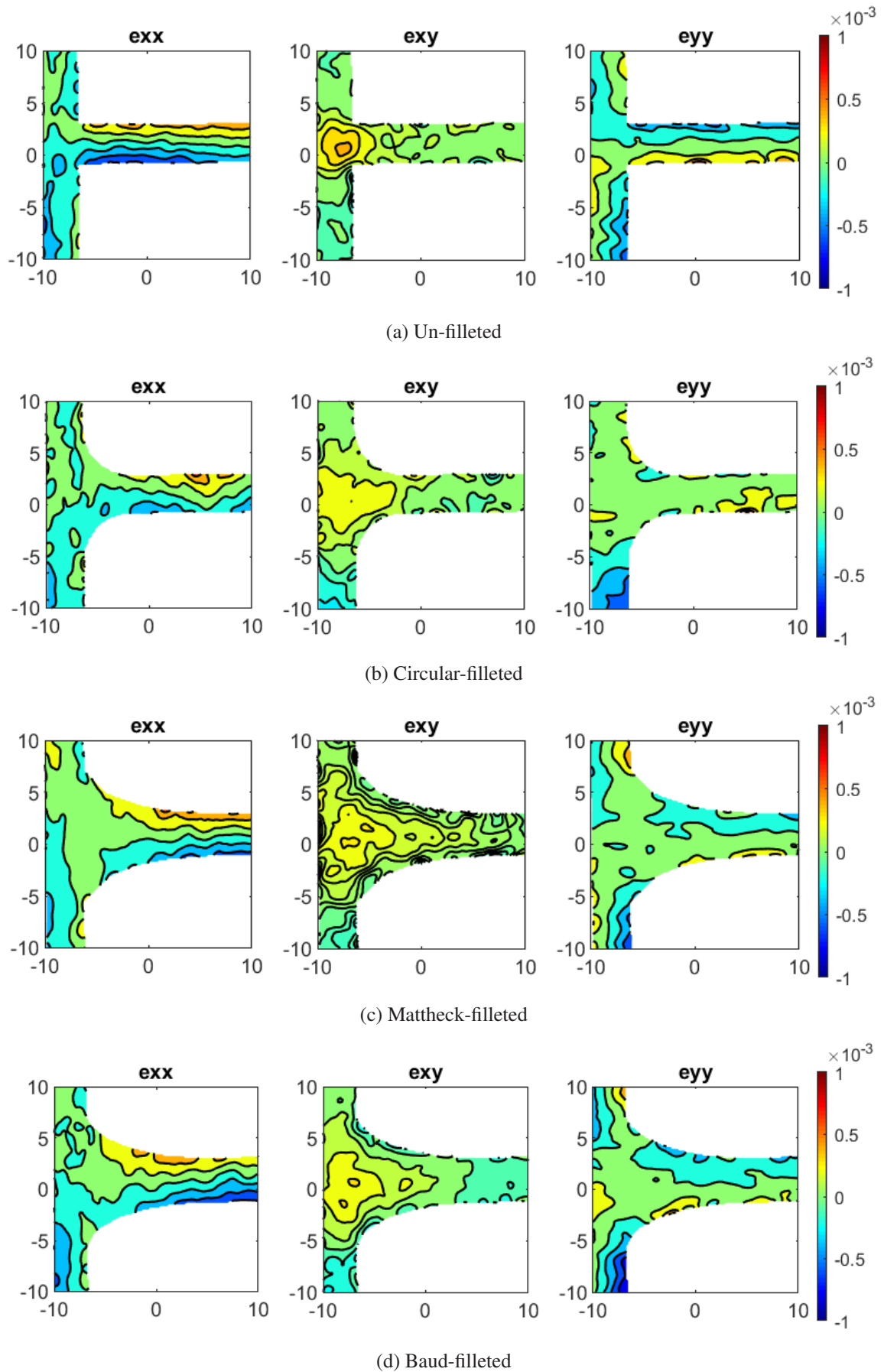


Fig. 6.18 The finite node internal strains for a 1 [%] tip deflection

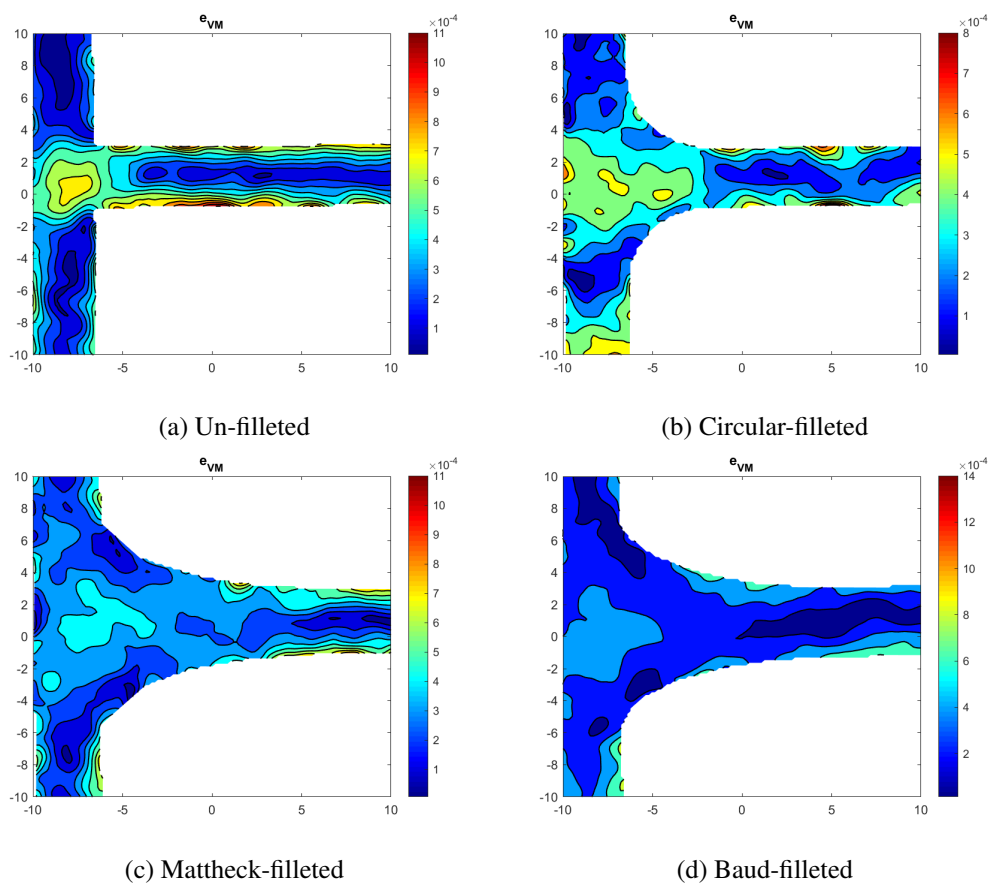
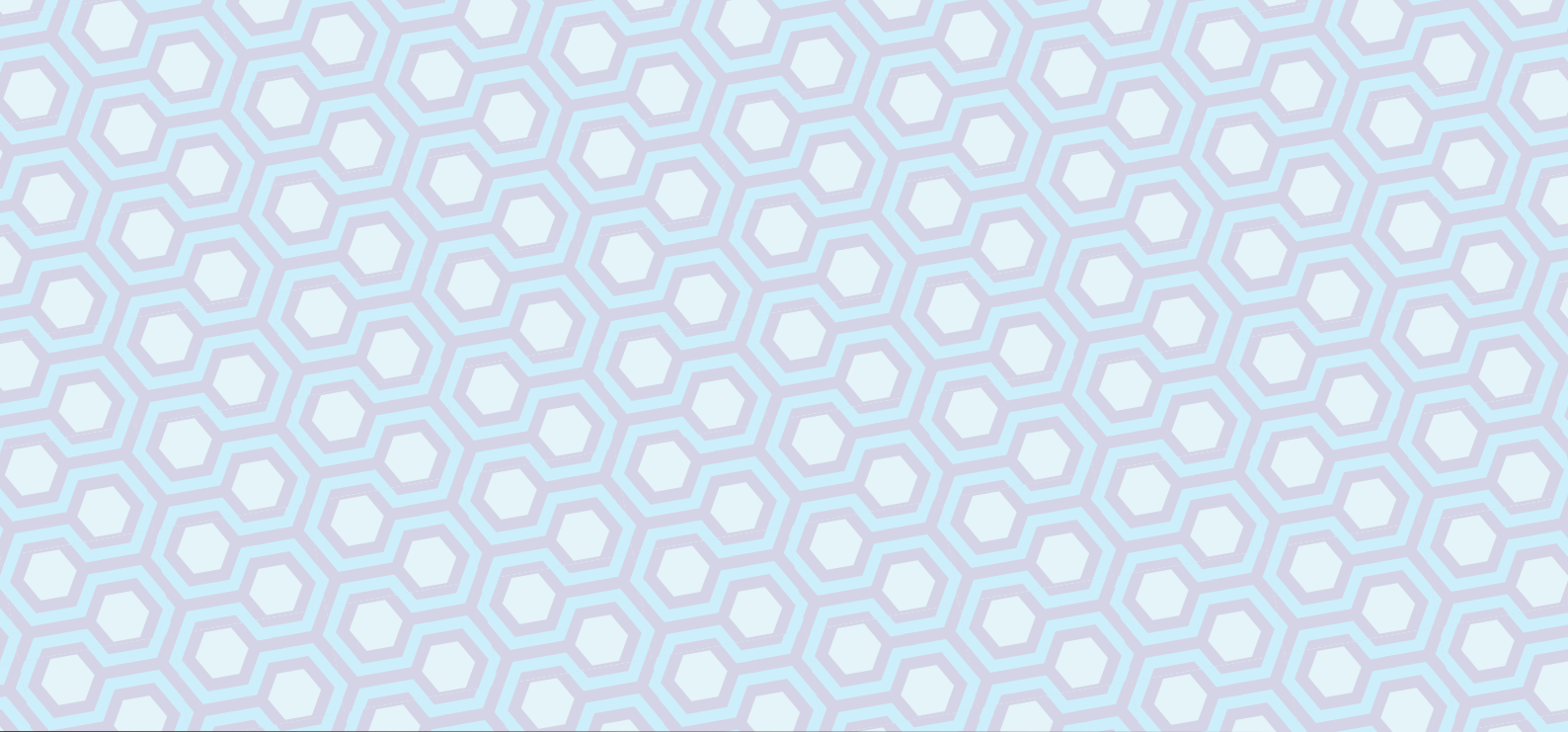


Fig. 6.19 The finite node equivalent Von Mises strains for a 1 [%] tip deflection



**Part III**

**Honeycombs**





## Chapter 7

# Cellular solid level methodology

In an attempt to systematically assess the sensitivity of cellular solids to nodal topology, and offer new insights grounded in real experimental data, the multi-scale study continues with the investigation on the so-called ‘cellular solid level’. A number of hypotheses were put forward earlier in Section 3. The process of refining specimen design, designing test procedures, and amassing enough detailed data to justify drawing those insights is detailed in this Chapter. The author has attempted to be up-front about the decisions that were taken - some of which are arbitrary - and to outline how the results presented in Chapter 6 can be reproduced. More specifically, the objective is to reproducibly challenge Hypotheses 2.1 through 2.4.

### 7.1 Specimen design

The developed specimen type is a low relative density, finite, bioinspired hexagonal bee honeycomb. The difference between specimens can be found by examining their nodal topologies, articulated through the application of different fillet shapes. Should the specimen’s deflection rigidity change for a change in nodal topology, after controlling for other factors, this would indicate a direct correlation between the two, thereby disproving hypothesis 2.1. Details on specimen fabrication and post processing is given in (van Helvoort, 2018).

#### 7.1.1 Nodal fillet shapes

The first fillet shape is the non-filletted node: the result of struts intersecting each other. The remaining shapes were an arbitrary assortment of fillets inspired by different contexts. An overview of the chosen shapes is given in Table 7.1. For more information, the reader is directed to Chapter 2. Table 7.1 similar to Table 4.1, except for the substitution of the ‘lumped’ node design for Baud’s fillet. The lumped node specimen was roughly designed to have a similar amount of material as the other specimens. This choice was made as Baud and Mattheck are similarly shaped, and the author wanted

Table 7.1 Overview of the nodal designs to be applied to the hexagonal cellular solid specimens

Fillet shape	Inspiration
No fillet	Baseline design (current state of most cellular solids)
Circular	'State-of-the-art' in cellular solid design; straight-forward engineering practice
Mattheck's fillet	Bioinspired stress-reducing fillet design
Lumped nodes	Control specimen

to verify that there is more to nodal design than increasing the amount of material allocated to it: all the whether or not shape is of importance is central to the discussion of this thesis.

The geometric or parametric definitions for the first three fillet are given in Chapter 2, where the only obvious common geometric parameter is the fillet envelope height . As the author wished to observe the surface strain of an affected nodal area without significantly disturbing the far-field behavior, the envelope height was arbitrarily set to  $1/10^{th}$  of the strut length for these specimens. For the special case of the lumped node, the increase in volume for the circular node was considered. A theoretically equivalent volume of material was assigned for a circular lumping of material at the node using basic geometry.

### 7.1.2 Specimen development

The first compression specimen designs suffered from printability issues when printed at large inclines for low relative density, and a lack of beam slenderness for printable higher relative densities. After some experimentation, it was discovered that printing thinner extrusions of the honeycomb profiles led to more successful prints. Unfortunately, the second series of compression specimens suffered from significant out-of-plane warping. Although significant differences in the initial deflection rigidities were measured, the boundary conditions were poorly controlled and likely inconsistent, thus rendering the results untrustworthy.

The apparent constraint to print thin extrusions of a honeycomb profile led the author to experiment with a compression-tension (CT) -like specimen design. The concept was to pry an initiated crack between two pull-lugs and observe the crack propagation under quasi-static conditions. Unfortunately, these lugs shattered when drilled, and although Metal plates made from sheet metal were secured to the pull-lug areas with adhesive and clamped in the machine, the clamp eventually slipped. These results were also considered unreliable. Nevertheless, an interesting observation was made.

It was noticed that the initiated crack propagated by fracturing struts close to or at nodal points for the non-filleted honeycombs, and quickly turned towards the clamps. In the case of the filleted honeycombs, however, the crack turned 30 degrees from the initiation zone, and travelled straight through the lattice, fracturing struts almost exactly in the middle, half-way between nodes.



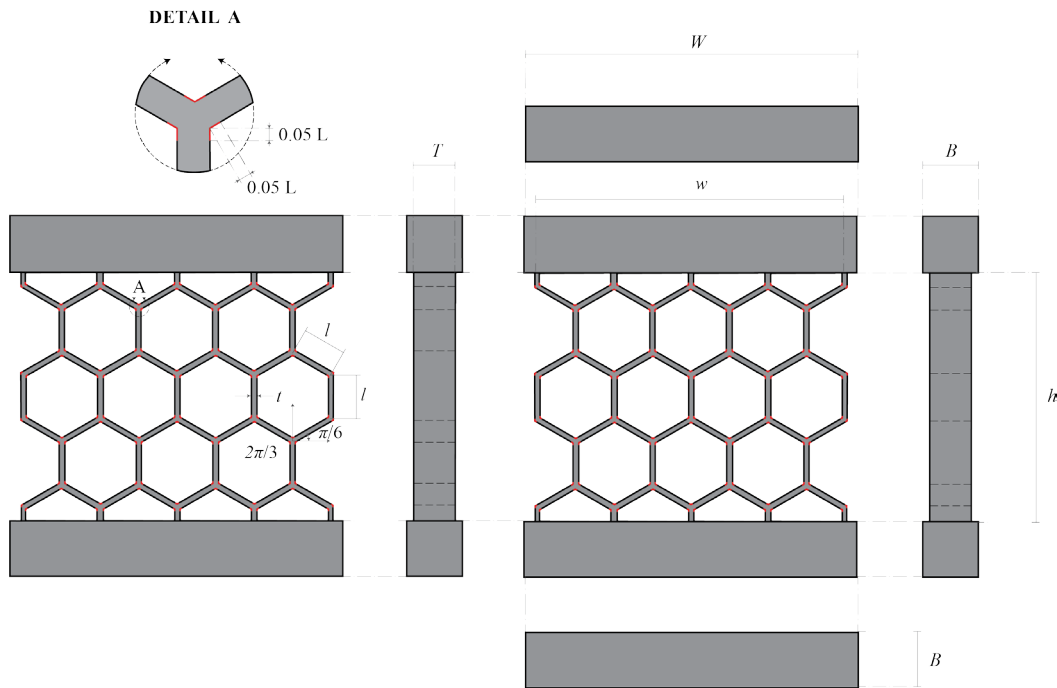


Fig. 7.1 The generalized hexagonal honeycomb specimen, where the red lines indicate the areas affected by the fillet, if present.

### 7.1.3 Chosen specimen design

The lessons from the development process were addressed in an improved compression specimen design. Although a larger order cell structure help support regions to behave as if in a continuum, the low relative density relaxes its importance; it is hoped that a lower cell order will test the proposed hypotheses. A generalized drawing is given in Figure 7.1, where the annotated filleting regions are adapted according to the proposed test matrix.

The specimen arbitrarily features 10 complete cells and 8 ‘boundary’ cells whose vertical struts are encased inside of integrated load introduction bars. The purpose of including bars was to improve consistency in specimen alignment in the test environment, and to introduce load more evenly. The placement of the bars was based on the idea that interrupting vertical struts would mimic the effect of higher order cell systems for low strains. Strut stability here is increased, encouraging failure to occur in the middle of the functional specimens. The high stiffness of the bars relative to the low deflection rigidity of the embedded specimen is assumed to be orders of magnitude higher, justifying this proposal. Furthermore, the effect of the bars straining on the observed strain can assumed to be negligible. It should be checked that excessive deformation or failure does not occur in or near the bars.

## 7.2 Methodology validity

The proposed experiment is comparative, whose objective is to investigate the effect of nodal topology on cellular solid deflection rigidity and the nature of the stress fields in one of the cell walls. To level the playing field the apparent deflection rigidity was normalized by relative differences in mass. Details on the normalization procedure can be found in Chapter 8.

The printed specimens were weighed by a Mettler AE 1666 digital scale. The projected volumes of material were acquired from the PreForm printing software.

The material used to fabricate all specimens was the Formlabs Gray resin V4 using a Formlabs Form 2 SLA printer. The specimens were rinsed and post-cured using the Formlabs Wash and Cure stations respectively. It is assumed that the critical sections to be compared are not thick enough to experience residual stress concentrations, and other material differences as a result of the manufacturing processes used are eliminated using the manufacturer's advise on specimen treatments. The relatively thick parts of the specimens did not seem to suffer from excessive warping, indicating that this is a reasonable assumption to make. The assumptions were necessary with regard to the thesis scope and time-frame. This is revisited later in Chapter 10.

## 7.3 Experimental design

### 7.3.1 Test goal

This is a comparative experiment a compressive load is introduced through load introduction bars into cellular solid specimens. A comparison of overall deflection rigidity, the center wall strain fields and observed qualitative behavior will be had.

The force is applied and recorded by a 20kN Zwick 1455 20kN test bench equipped with a 1 [kN] load cell along with the cellular solid's deflection. To improve load introduction to the solid bar, a metal part was specially fabricated to provide a consistent interface between the load cell and the loading bars. The load should act in-plane with the cellular solid's 2-D geometry (the effectively extruded cross-section).

### 7.3.2 Specimen preparation and camera calibration

After fabricating, washing and curing the test specimens – processes that are detailed in (van Helvoort, 2018) – the specimens were brought to the DASML paint booth. The target surfaces for DIC were spray-painted with a flexible matte white base coat and left to dry for 1 hour. In that time, the DIC setup was calibrated, and the calibration file saved as a reference data file. Then, spare samples were speckled with black paint using swift consistent motions from several distances. Those samples were brought the experimental setup, and the speckle patterns were reviewed. The best results were attempted once more, and then applied to the real experiment specimens.

Table 7.2 Summary of the cellular solid test program on a Zwick 1455 equipped with a 1 [kN] load cell.

Hexagonal honeycomb tests	
Max. force channel voltage [V]	10
Max. force channel force [N]	10000
Max. force test [N]	8000
Max. displ. test [mm]	80
Preload [N]	5
Strain rate test [mm / min]	5

### 7.3.3 Experiment procedure

Table 7.2 summarizes the experimental test program that was used for the 20kN Zwick 1455 20kN test bench. It is also available for download in the form of a template and with the unprocessed experimental data at (van Helvoort, 2018).

The following procedure was then followed.

1. A specimen is placed in the test environment. A small distance of approximately 3 [mm] can be left between the specimen and the test bench's point of force application.
2. The environment temperature and relative humidity is recorded using a simple climate instrument.
3. The DIC camera rig is manually set to start taking pictures at a rate of 2 FPS using hardware triggering.
4. The regular camera car is manually set to start taking pictures at a rate of 2 FPS using the camera car software.
5. The load cell is calibrated to 0 [N].
6. The test program described in Table 7.2 is executed.
7. After reaching the maximum force threshold, the camera rigs are manually controlled to stop taking pictures.
8. The specimen is removed. Any necessary data management can be performed. Return to step 1 until all specimens have been tested.



## Chapter 8

# Cellular solid level data processing

Unprocessed data in the form of analog sensor spreadsheet logs, and stereoscopic DIC black and white digital images were processed with MATLAB and Correlated Solutions' VIC-3D 8. The camera car photographs were to be used for qualitative purposes only. The reader is referred to (van Helvoort, 2018), where the MATLAB data processing scripts have been made available. Briefly, the underlying theory is presented in this Chapter. Appendix C contains an overview of the settings used for VIC-3D 8.

### 8.1 Apparent initial flexural rigidity

To compare the apparent initial flexural rigidity of the cellular solid specimens, the force-deflection curves of each specimen was analyzed. Although a pre-load of 5 [N] was defined in the test program, it is assumed that any remaining initial non-linearities are the result of load introduction and are not significant. A small deflection window from 0.5 and 1.0 [mm], at the beginning of each specimen's response, was arbitrarily selected to define the initial flexural rigidity, defined earlier in Equation 2.14.

### 8.2 Normalized specimen strain energy absorption before break

The work done by the test bench to compress the honeycomb specimens until failure can be defined as the integral of the resultant force with respect to its deflection. For the displacement-controlled test, numerically using `trapz`. One can also calculate a more conservative estimate from load initiation until the maximum force experienced. The appeal of the latter method is that it more representative for contexts where a maximum load is more relevant, barring strain rate effects. The latter is particularly important.

Spring back is not considered relevant, as the total energy absorption until failure is what seemed most-interesting, and illustrative for energy-absorption contexts wherein loading until failure is of key significance. Mathematically, the two methods can be expressed mathematically in terms of the

honeycomb axial deflection  $\delta$ :

$$U_1 = \int_0^{\delta_{ult}} F d\delta, \quad (8.1)$$

and

$$U_2 = \int_0^{\delta_{F_{ult}}} F d\delta, \quad (8.2)$$

where  $U$  is the strain energy absorbed up to the ultimate deflection  $\delta_{ult}$  and ultimate force  $\delta_{F_{ult}}$  respectively, and where  $F$  is the force.

Each energy absorption can be normalized by each specimen's relative density to give the relative density specific energy absorption  $\bar{U}_i$  before break of each specimen as defined by

$$\bar{U}_i = \frac{U_i}{\rho_{rel}}, \quad (8.3)$$

and where  $U_i$  is the chosen method, and  $\rho_{rel}$  is the specimen relative density.

# Chapter 9

## Cellular solid level results

The hexagonal honeycomb specimens whose detailed designs are explained in Chapter 7 were tested according to the methodology set out in Chapter 8. Together, the group represents the cellular solid level effect of nodal topology on an arbitrary over-arching cellular solid architecture in a wider multiscale analysis of the research question defined earlier in 3. These results shall presently be synthesized in a cross-scale synthesizing discussion in Chapter 10.

A summary of the projected specimen volumes are provided in Table 9.1. The functional mass is defined as the material volume that only corresponds to the cellular solid itself; in other words, the volume without the loading bars.

A theoretical solid block of material that occupies the space of each honeycomb, with dimensions  $T$ ,  $W$ , and  $w$  was calculated. This theoretical block is the reference solid from which the specimen relative densities are calculated. These results are provided in Table 9.2.

Under quasi-static displacement-controlled compression, the mass-normalized deflection rigidities of each specimens specimen seem distinctive from each other. The unprocessed test results are shown in Figure 9.1. A visual depiction is shown in Figure 9.2. The initial deflection rigidities were plotted against each specimen's relative density is shown in Figure 9.3 along with trend shapes that the Ashby model would expect.

By integrating the force-displacement curve, the strain energy stored in the cellular solids before failure can be calculated. By integrating the force-displacement curve to the point of maximum load,

Table 9.1 An overview of hexagonal honeycomb specimen projected total and functional volumes

Fillet design	Specimen projected volume $\pm 0.05$ [ml]	Functional projected volume $\pm 0.05$ [ml]
No fillet	122.53	25.43
Circular	124.76	27.66
Mattheck's fillet	124.99	27.89
Lumped node	124.84	27.74

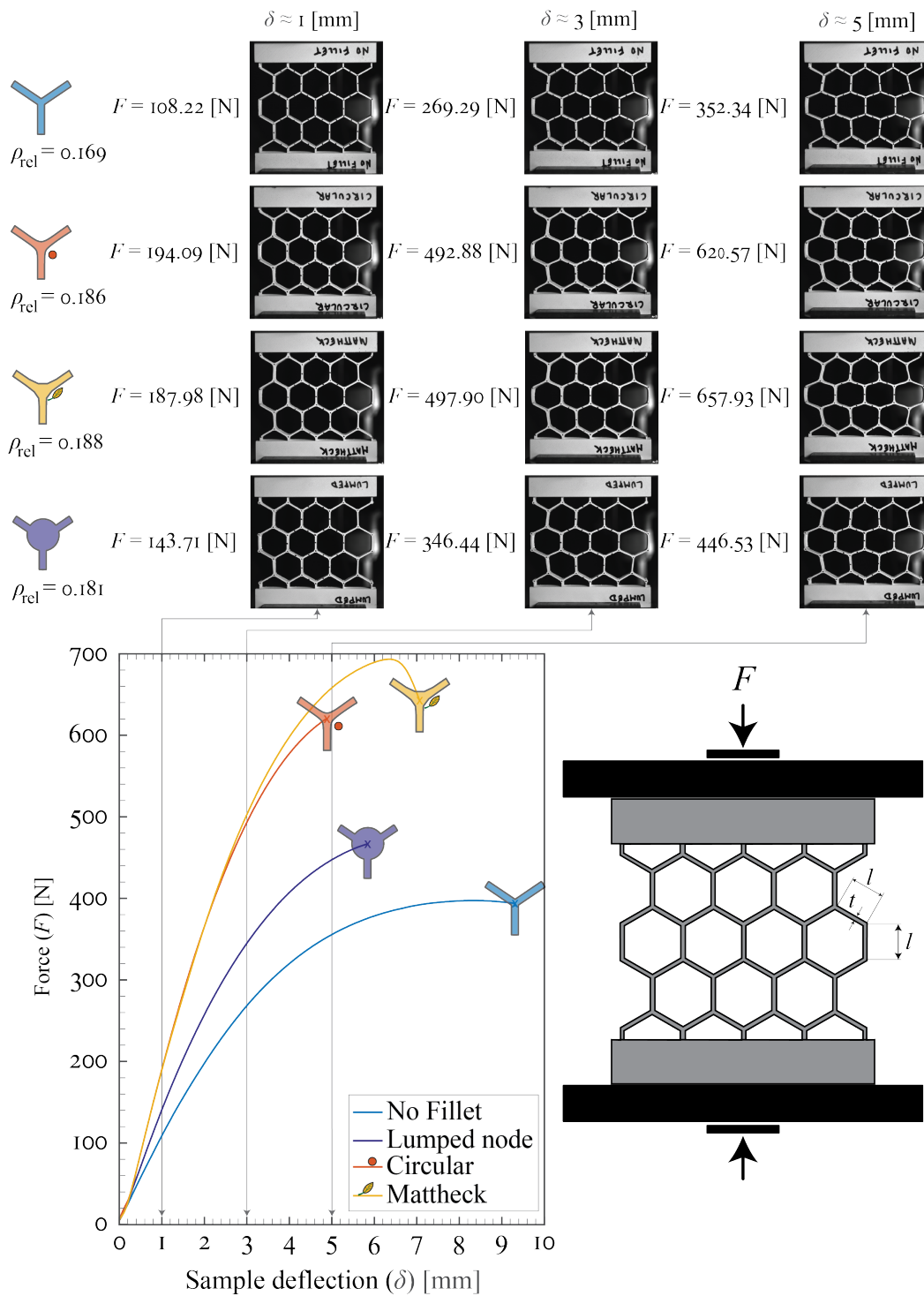


Fig. 9.1 The unprocessed force-displacement of the hexagonal honeycomb specimens



Table 9.2 Overview of the hexagonal honeycomb specimen relative densities

	Relative density ( $\rho_{rel}$ ) [%]
No fillet	16.91
Circular	18.62
Mattheck's fillet	18.78
Lumped nodes	18.07

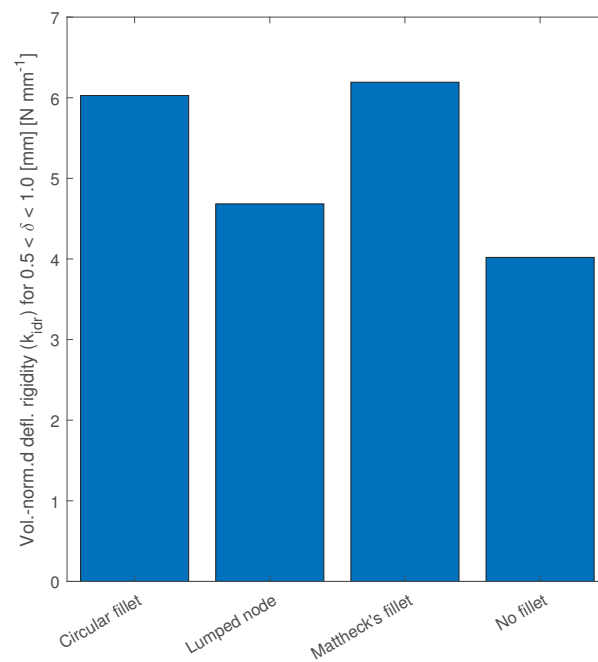


Fig. 9.2 The volume-normalized initial deflection rigidities

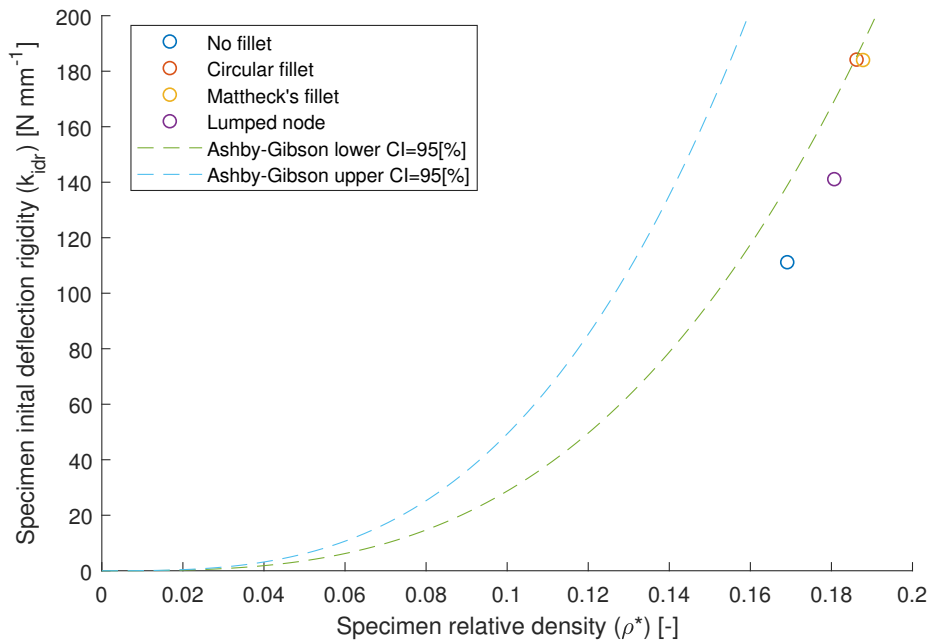


Fig. 9.3 Relative density against the initial deflection rigidities of the hexagonal honeycomb specimens. The Ashby-Gibson model is plotted for a material confidence interval of 95 [%]. Notice that the data points do not fit these shapes.

Table 9.3 Overview of the hexagonal honeycomb specimens' energy absorptions

	Energy absorption to $F_{ult}$ ( $U_{F_{ult}}$ ) [J]	Energy absorption to $\delta_{ult}$ ( $U_{\delta_{ult}}$ ) [J]
No fillet	2353	2760
Circular	1870	1877
Mattheck's fillet	2927	3398
Lumped nodes	1766	1769

an approximation for the strain energy absorption potential of each specimen can be estimated for a force-controlled experiment. These results are given in Table 9.3, and shown visually in Figures 9.4 and 9.5.

The DIC results show that strain gradients from node to node across specimen cell walls have the appearance of a 'bathtub', whose sensitivity to strain gradients in the nodal area seem to inversely correlate with the magnitude of the mean or mid-strut strain, and the overall cellular solid deflection rigidity. This can be seen in Figure 9.6.

Each of the specimens failed in an apparent catastrophic explosion, with the specimens breaking into many small shards. Observations were made by the author at the time that the size and number of shards seemed to differ across specimens, although it is difficult to know whether each shard was the direct result of the failure, or the result of secondary collisions such as hitting the test environment or floor. Furthermore, the filleted specimens experienced fractures in the strut sections at roughly

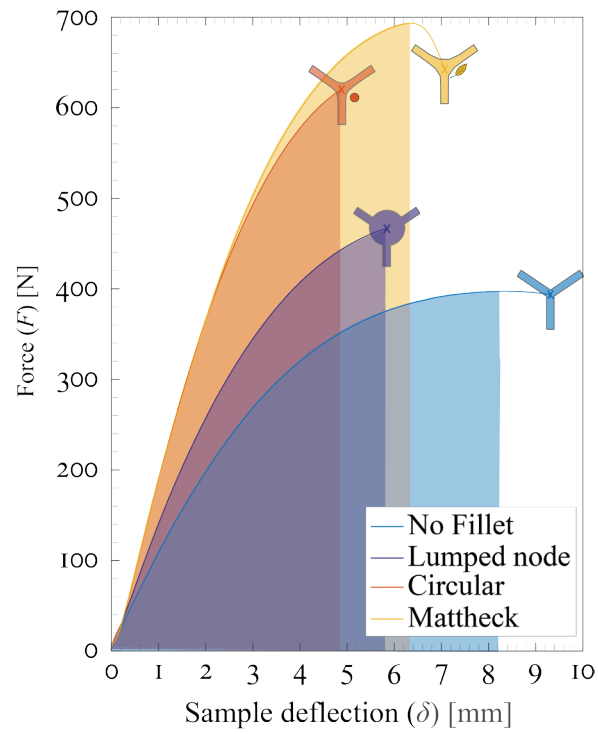


Fig. 9.4 Energy absorption of hexagonal specimens until ( $F_{ult}$ ).

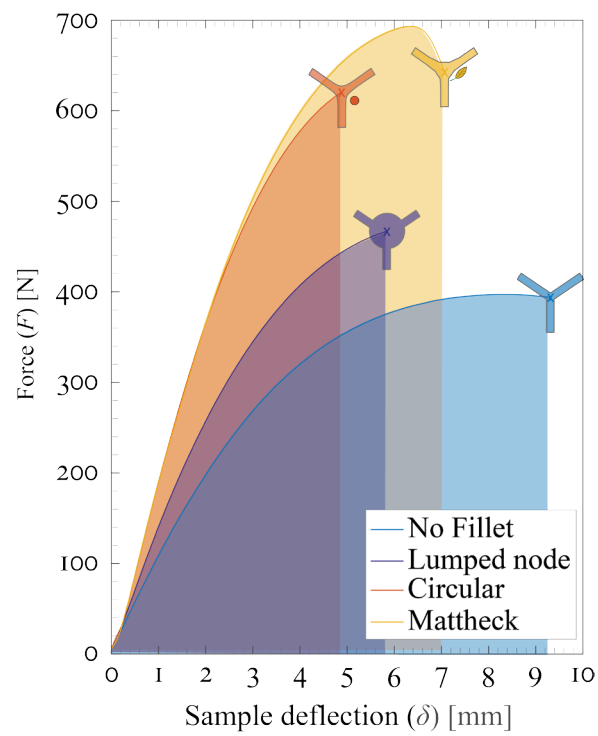


Fig. 9.5 Energy absorption of hexagonal specimens until ( $\delta_{ult}$ ).

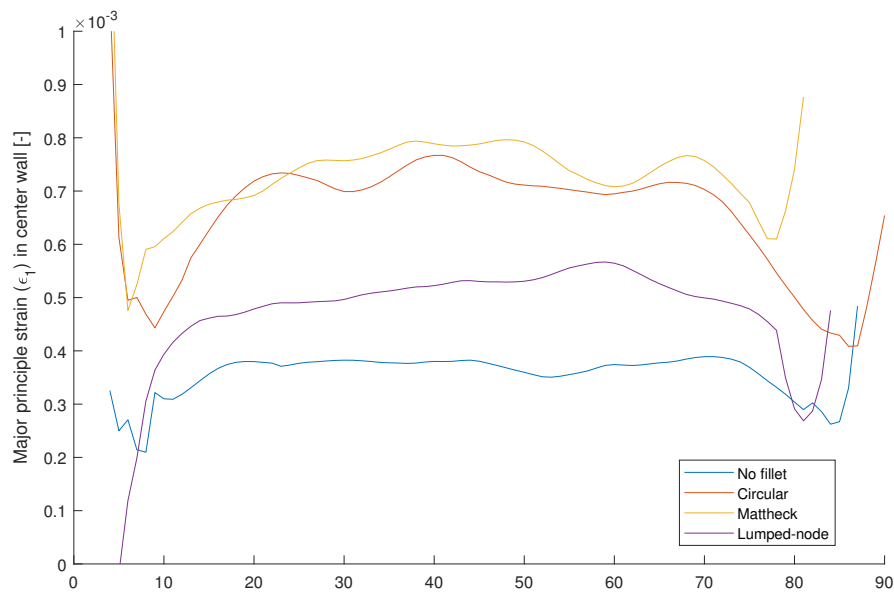


Fig. 9.6 Bathtub major strain curves for hexagonal honeycomb center wall during a 1 [%] tip deflection.

1/3 or 1/2 through the attached strut, whereas the un-filleted and lumped-node specimens failed at the notch of the strut-node interface. Pictures of the un-filleted, circular-filleted, Mattheck-filleted and lumped-node honeycomb specimen fragments can be found in Figures 9.7, 9.8, 9.9 and 9.10 respectively.

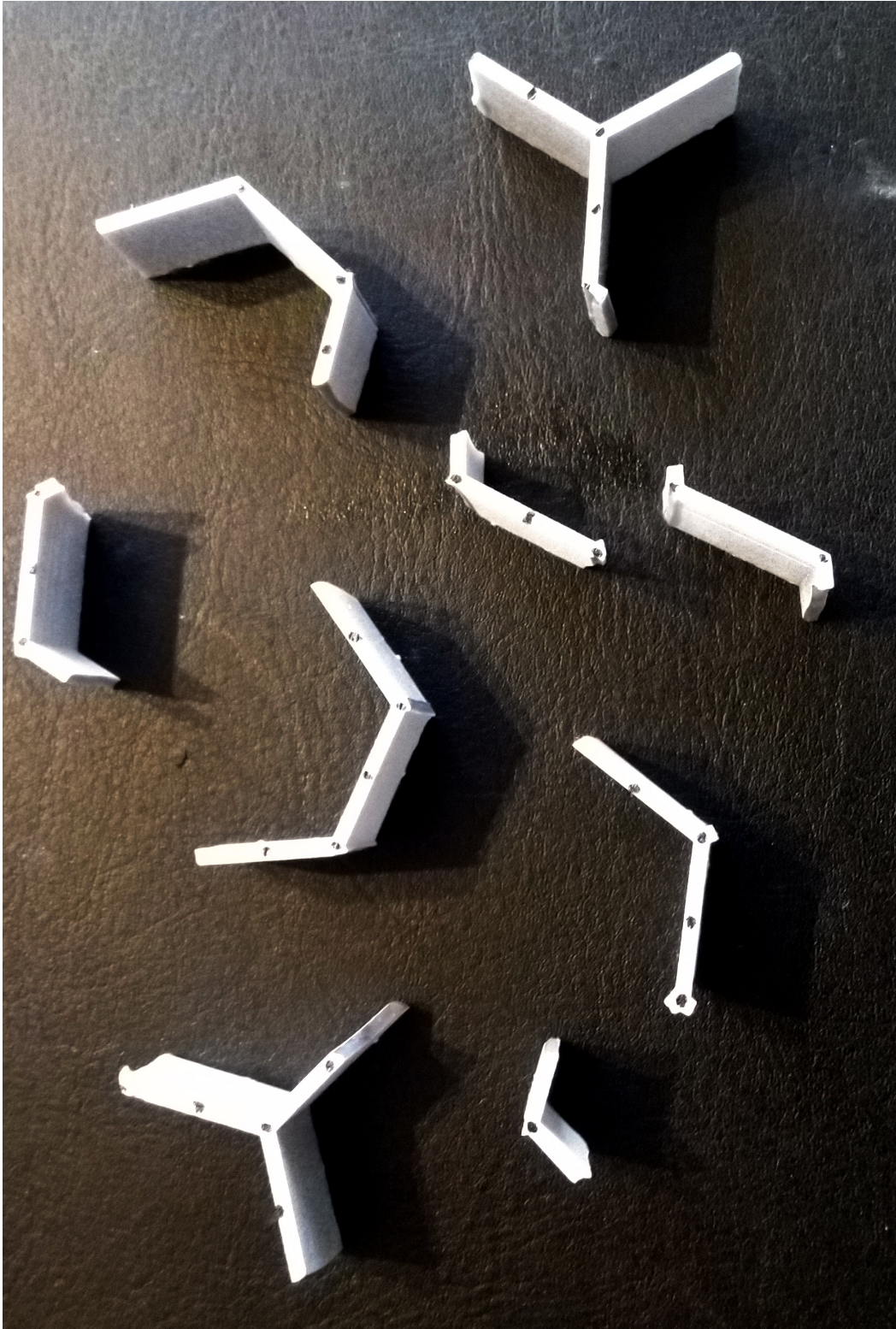


Fig. 9.7 Photograph of the un-filleted honeycomb post-experiment fragments

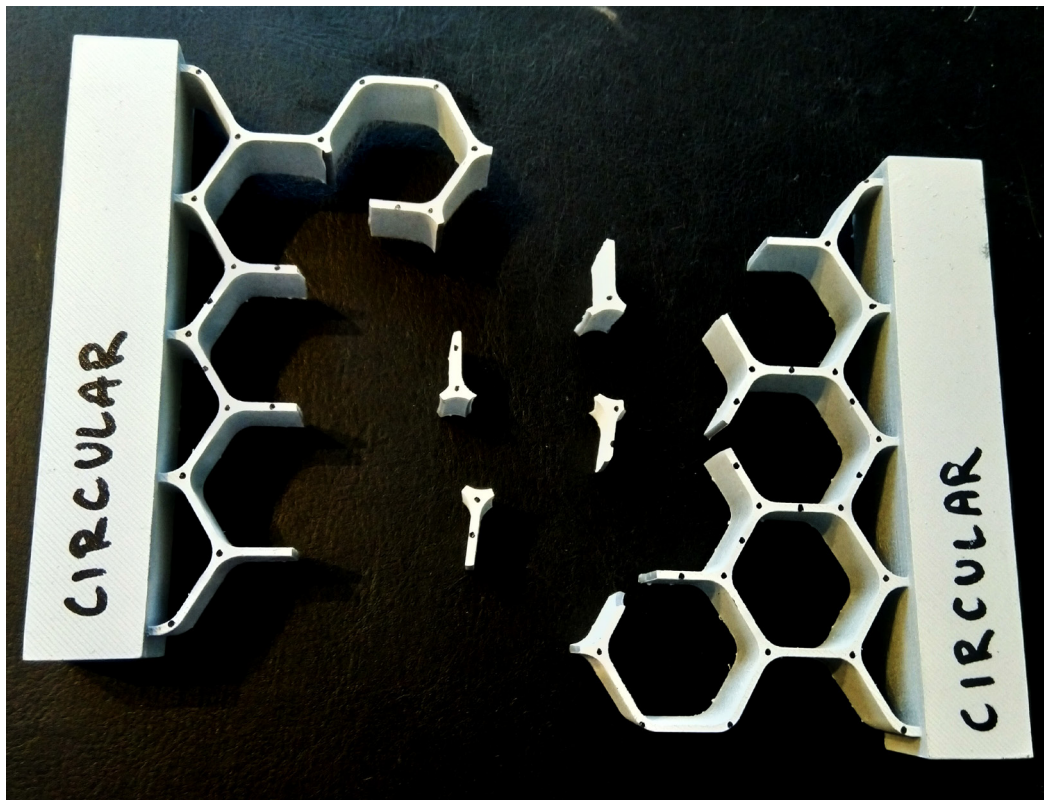


Fig. 9.8 Photograph of the circular-filletted honeycomb post-experiment fragments

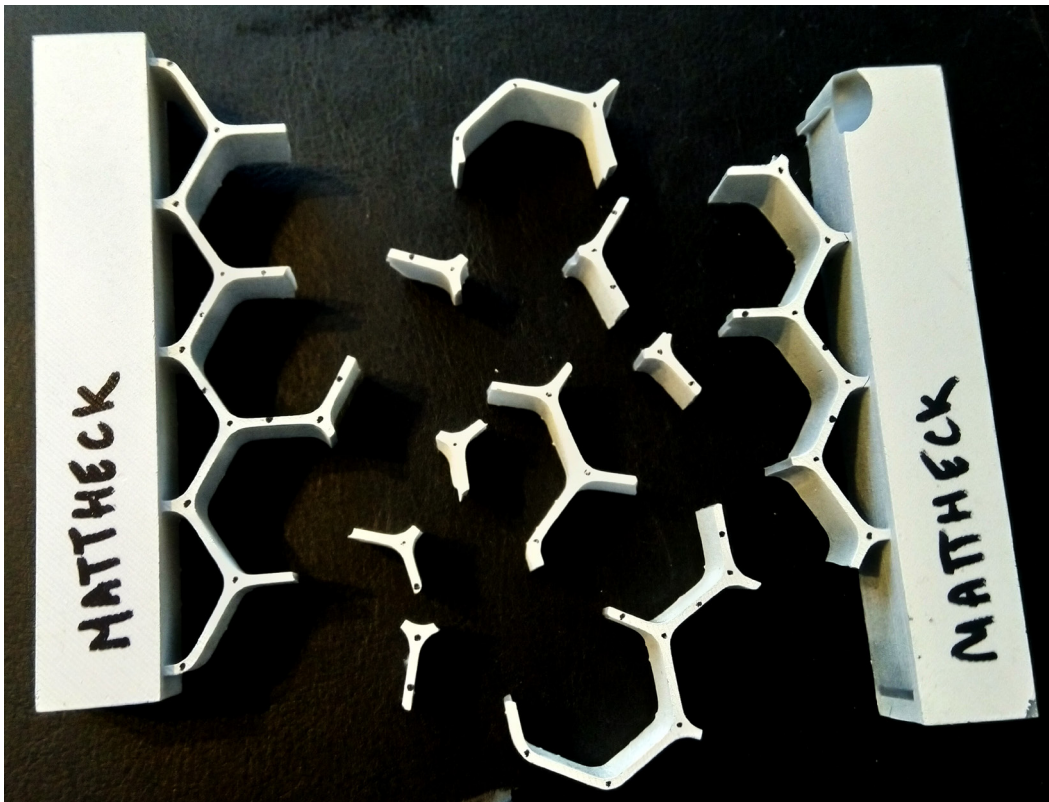


Fig. 9.9 Photograph of the Mattheck-filletted honeycomb post-experiment fragments



Fig. 9.10 Photograph of the lumped-node honeycomb post-experiment fragments





---

**Part IV**

**Discussion, conclusions &  
recommendations**

---



# Chapter 10

## Discussion

Although additive manufacturing has allowed researchers and engineers to produce metamaterials, knowledge of cellular solids is still emerging. The detailed behavior of unit cells and their constituents are not yet fully understood. Studying natural cellular solids like avian long bones reveals that nature homogenizes stress to maximize material usage: reinforcing struts join to the thinner-than-mammalian bone walls through stress-reducing fillets. One might well ponder about the sensitivity of cellular solids to nodal topology, the subject of this preliminary experimental investigation. Two null-hypotheses were made, one on the nodal-level of analysis, and one on the cellular solid-level, regarding the effect of nodal topology on the overall initial deflection rigidity: that there would be no effect.

Null hypotheses regarding the local stress fields of nodal regions regarding their topology as well, namely that they would be indifferent to such changes. If-then hypotheses were also given, predicting that a reduction in stress localization generally leads to improved mass- (or volume-) normalized deflection rigidity. For the cellular solid case, a reduced sensitivity to high-stress regions through the neutralization of stress concentration would increase the height of the so-called stress plateau.

### 10.1 A synthesis of the experimental evidence

At the nodal level of analysis, the initial deflection rigidity of the specimens - a step that essentially idealizes specimens as torsional springs - indicate distinct differences. The least-rigid responses were those of the un-filleted and circular-filleted specimens while the most rigid responses were those filleted with Mattheck's bioinspired and Baud's fluid flow-inspired curves, even after controlling for the volume of functional material.

The aforementioned groupings seemed to hold for both the infinite and finite cases, although the relative difference between the two groups was reduced in the latter case. This is undoubtedly due to the general topology of that problem: instead of a practically infinite reservoir of material for strain to dissipate into, the node is no longer encastré and is able to warp 'freely'. Nevertheless, a difference in

stiffness was still observed for a rather challenging load transfer problem, where material stress must flow around a sudden 90 degree corner into the adjoining struts.

The author suspects that had the tests continued to specimen failure, the Baud- and Mattheck-filletted nodes would have caused the specimens to be more tough. The circular-filletted design, meanwhile, would hold some middle-ground in terms of toughness. Initially, this suspicion was based on the extents of stress-concentration mitigation that can be expected from those designs from classical stress concentration theory; reducing the peak stress may easily affect the development of geometric non-linearity from bending itself, as well as the point of onset for multiple failure modes including strut lateral buckling and brittle collapse. A reduction in the magnitude of the maximum stress concentration and its localization was indeed observed, which was accompanied by a shift in its location away from the nodal region. This can be seen in Figures 6.8 and 6.17.

Steps in the methodology were specifically designed to control each specimen's fabrication, post-production steps, and clamping. Specimens within a series were printed simultaneously or in closely timed batches, and in similar orientations; they experienced tightly controlled rinse cycles and cure times; and they were stored together in a light-tight box until they were painted, speckled and tested. Regarding the latter steps, paint applications occurred simultaneously in the DASML paint booth, and a test clamp for both series was manufactured from aluminum to ensure near-identical loading. The point of load application was recorded in the form of an ink-print on the strut for later analysis to help define  $l$ .

Although the material quality of the specimens was not specifically investigated by the author, little-to-no warping was observed in the hexagonal honeycomb bars or infinite-node, save for the back-end of the infinite bases. The essential parts of each specimen were relatively thin by comparison, so it is thought that any residual stresses from curing are not significant enough to cause process-dependent changes in the specimens. Furthermore, the manufacturer-recommended post-cure stage is thought to address any residual stresses in a kind of heat-treatment. Any mechanical differences, by extension, are assumed to be the result of geometric differences only. This was a preliminary diagnostic investigation. Before drawing any final conclusions, however, the material quality of the Formlabs 3-D printers should be more intimately understood. To do so is beyond the time-scale and scope of this project.

In summary, With the exception of the Baud-filletted infinite node which rotated in its clamp due to an incompletely-fastened screw, the author makes the following over-arching assumption: ***the specimens are comparable to one another***. Thus, the differences between the individual initial deflection rigidities within each series are significant, directly challenging Hypothesis 1.1, although more efforts are required for these findings to prove conclusive.

In a similar vein, at the cellular solid level of analysis, the initial deflection rigidities as seen in Figure 9.1 of the filletted specimens seemed to stiffen, thereby increasing the effective Young's Modulus of the hexagonal honeycomb. For a given displacement, the sum of the internal loads result

in a larger required force for that deflection: an important design aspect for lightweight stiffness-led designs such as beams.

Examining the cellular solid center wall principal strain distributions in Figure 9.6, it can be seen that the initial stages of each experiment shows that the un-filleted specimen walls are loaded most, followed by the lumped-node, then circular- and Mattheck-filleted specimens. Though the observed wall is not necessarily representative of all other walls, it is possible that the more highly loaded cell walls of the un-filleted and lumped-node specimens are the result the material absorbing strain energy more efficiently by better redistributing that energy throughout the structure.

This latter point is supported by examining the experiment debris, where the filleted nodes seemed to fracture in the struts themselves, and the un-filleted and lumped-node specimens failed next to or in the nodal area at the points of high stress concentration. Furthermore, the pieces not caused by secondary impacts - a careful study of the experiment pictures was performed - seem to be more plentiful and smaller for the circular- and Mattheck-filleted specimens, and larger and fewer for the lumped- and un-filleted specimens. These arguments are more subjective than the author would like, and not as reliable as the others. Perhaps the use of high-speed cameras would help to determine what was caused by specimen failure caused by the test, as well as a means to determine the size and number of parts more accurately. It should be noted that it was not possible to find all of the pieces, and smaller pieces were easily mixed up.

Earlier, it was assumed the a linear moment distribution would be caused by the force deflecting the infinite and finite node struts. The second derivative of the span-wise deflection according to DIC data was taken with respect to  $x$ , and relative to the point of load introduction  $l$ . This apparent strut stiffness was directly compared to the known local stiffness - the result of computing the second moment of area  $I_{xx}$  of the local rectangular section. Although relatively good agreement was observed for the outer or 'far-field' sections, the in-board sections indicated major anomalies for low values of  $x$ .

As the shape of the basic underlying structure is common between all specimens, the far-field can be expected to bend according to the Euler-Bernoulli bending law, and Saint-Venant's principle can be assumed to hold, the growing deviation towards the strut root does not yet have a satisfactory explanation. The discrepancy zone is essentially what might in future help define the node-strut interface, as well as refine their idealizations. In the hexagonal honeycomb structure, it seemed from the section-view strain distributions that the strut provides bending stiffness, and the node transfers acts as connective tissue, transferring load.

The transfer from strut to node, and the nature of the node itself infers high complexity. The models treated in this thesis are not sufficient to explain its characteristics. It is likely that an Airy stress function or similar mathematical models might contain the seemingly mysterious behaviors that were observed in the experiment: a growing increase in apparent stiffness towards the nodal area that seemed to culminate in an apparent singularity demonstrated by the asymptotic behavior, as seen in Figures 10.1 and 10.2, repeated here for the reader's convenience. In terms of the mathematical models treated here, it may be sufficient to say that the shape of the assumed moment distribution is

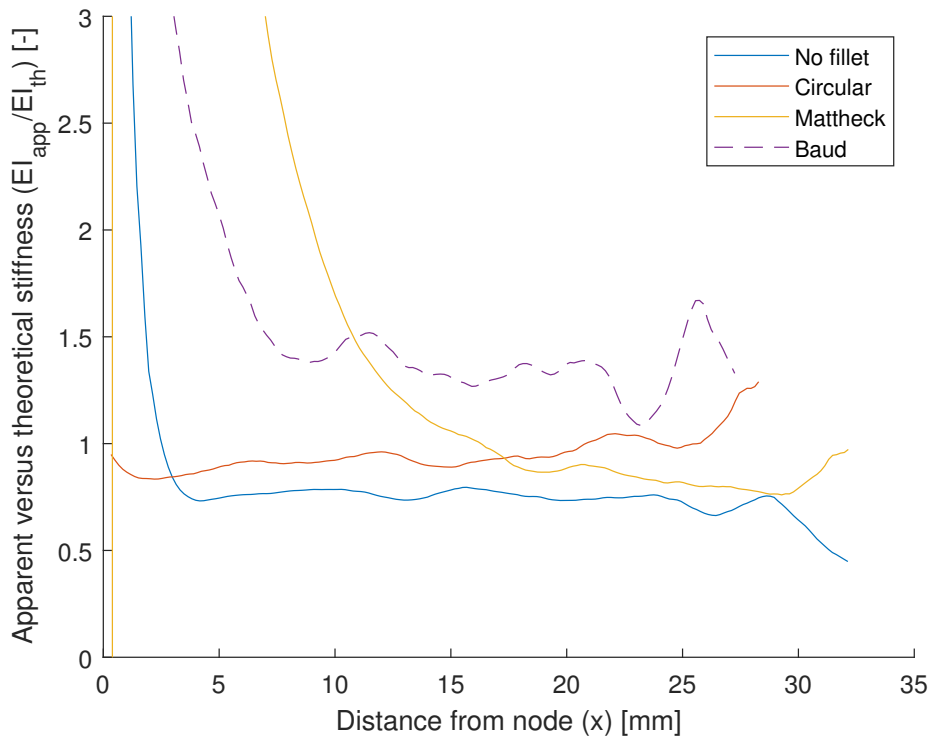


Fig. 10.1 A direct comparison of the infinite-node theoretical and apparent bending stiffness according to DIC data.

unrealistic; the expected strain pattern deviates in reality, as it either dissipates through shear into the infinite node, or transfers through shear into a mixture of bending and axial loading of the adjoining struts in the finite case.

This deduction is contained by the difference in the fictional effective strut lengths of the infinite specimens in Tables 6.5. The larger-than-expected values for the un- and circular-filletted struts indicate that the base material is not behaving as the expected cantilever. Some of the base material must therefore still be bending in an extended nodal region, affecting the definition of the load itself. The lower-than-expected values for the Mattheck- and Baud-filletted nodes indicate that the nodal region is *not* bending. Instead, improved load transfer seems to have undercut the moment distribution's development in the nodal region, and consequently changed the definition of its load to reduce it.

The DIC data for a small deflection of 1 [%] also supports the argument that the Euler-Bernoulli law is fundamentally challenged at the nodal level of analysis, where more complex mechanics are at play, thereby dominating the structural response. As seen in Figures 10.3 and 10.4 (repeated) the  $\epsilon_x$  distribution maintains its general axial pattern throughout the strut, and extends into the strut base for the infinite node before finally dissipating.

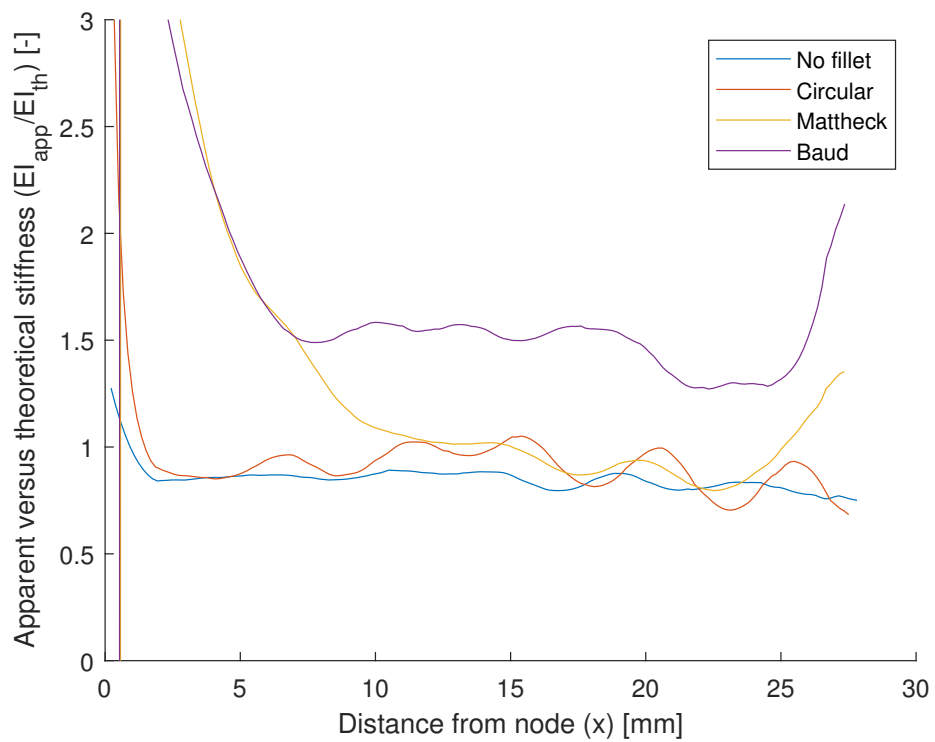


Fig. 10.2 A direct comparison of the finite-node theoretical and apparent bending stiffness according to DIC data.

In the finite node case, this dissipation is somewhat faster in terms of the full strain distribution, but bending technically occurs throughout the entire nodal region. The Mattheck-filletted specimens, meanwhile, deviate from this pattern much earlier, at a distance of 10 [mm] from the node. It is clear that the bending stress distribution was already experiencing an upset. The lines of equipotential - or isoclinics - following the outer free boundary indicate that stress here was relatively homogeneous at the free boundary.

The shear distribution is also highly significant to examine in the nodal area. In the un-filletted case, the strain distribution forms a highly localized 'hot-spot', whereas the Mattheck-filletted nodal area has a more homogeneous distribution, with isoclinics roughly adopting the free boundary shape. In other words, the strain takes the form of its 'container'. The peak shear stresses are lower, and are distributed over a larger area than in the un-filletted case. The circular fillet provides a kind of middle-ground, explaining its intermediate deflection stiffness relative to its un-filletted and Mattheck-filletted counterparts.

According to the Von Mises equivalent strain fields, shown again in Figures 10.5 and 10.6, the filletted finite nodes held an advantage over their baseline counterpart in that they outright eliminated the threat of an internal stress concentration in the nodal region itself. It would be difficult to observe this stress concentration in a more realistic structure.

In fact, the Mattheck-filletted finite node even had 'cold' material that could be removed to produce a more suitable overall topology for that specific loading, according to its Von Mises equivalent strain distribution. Such an act is similar to the so-called 'soft-kill' method that is so favored by Mattheck.

Although the detailed strain behavior of the cellular solid nodes is an incomplete picture in this series of experimental tests, differences in the initial deflection rigidities were observed for varying nodal topologies. More specifically, circular- and Mattheck-filletted seemed to significantly increase overall stiffness, and the lumped-node design formed a half-way point between them and the baseline un-filletted design. After inspecting the experimental debris, it was remarked that the apparent fracture positions seemed to coincide with high-stress locations that would be identified by classical fillet design theory in the un-filletted and lumped-node specimens. The Mattheck- and circular-filletted specimens, meanwhile, had fractures that occurred further out from the node itself, at a point where the cross-sectional area first becomes minimal.

Regarding ultimate failure, the Mattheck-filletted specimen was unique in that vertical cell wall elastic buckling of the center-most cells was observed for a few moments before failure. This caused the cellular solid to effectively soften before failing, which can be seen by a decreasing resultant force for an increasing displacement.

Whether or not the un-filletted specimen failed through elastic buckling is uncertain, though the last frame of the experiment does support such an assumption: the center walls are no longer upright. Furthermore, the force level was seen to dip slightly after the ultimate load was reached.

Assuming that the central struts of the un-filletted and Mattheck specimens did indeed undergo elastic buckling, the height of the stress plateaux can be assumed as a function of the struts' length,



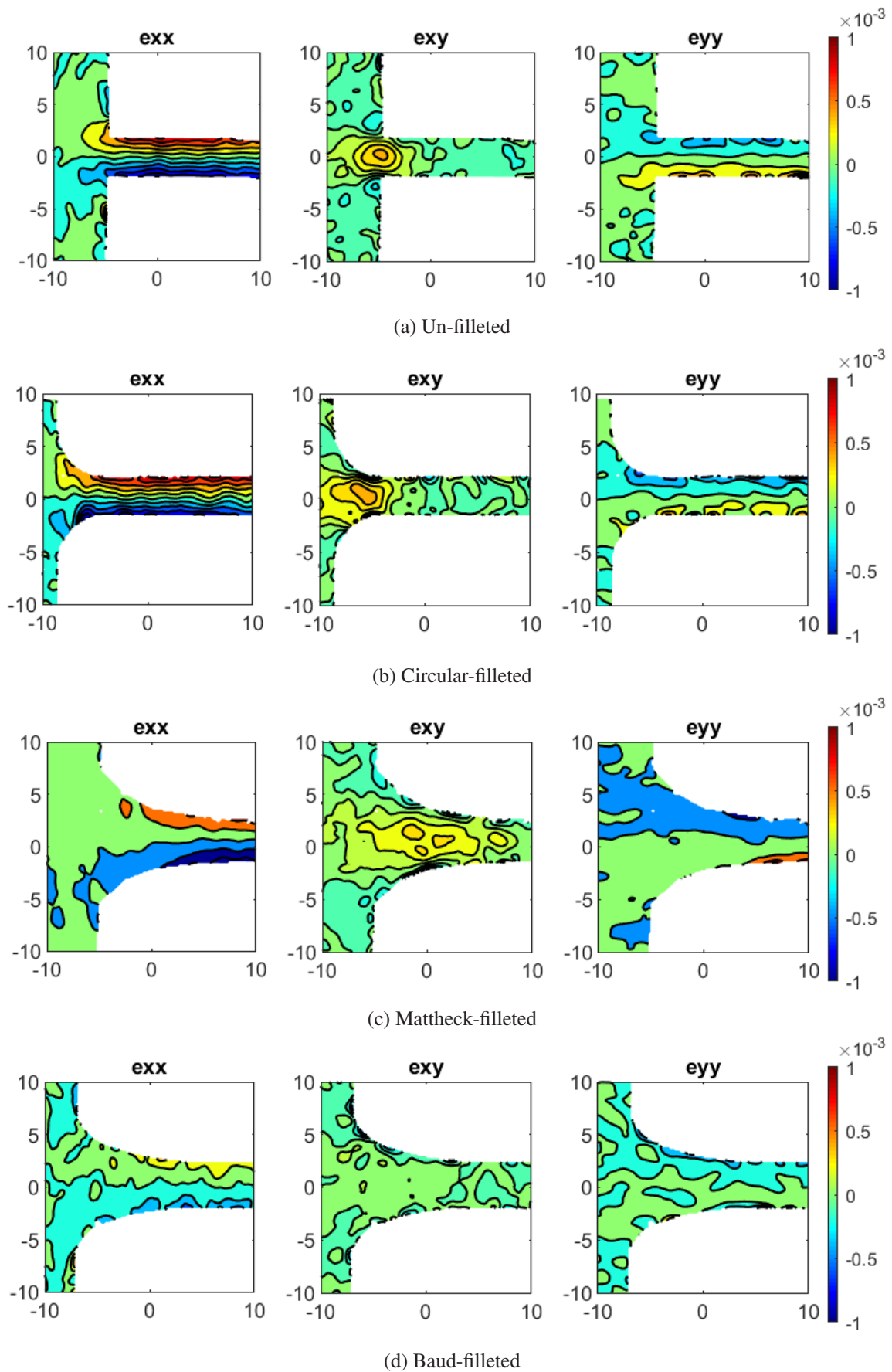
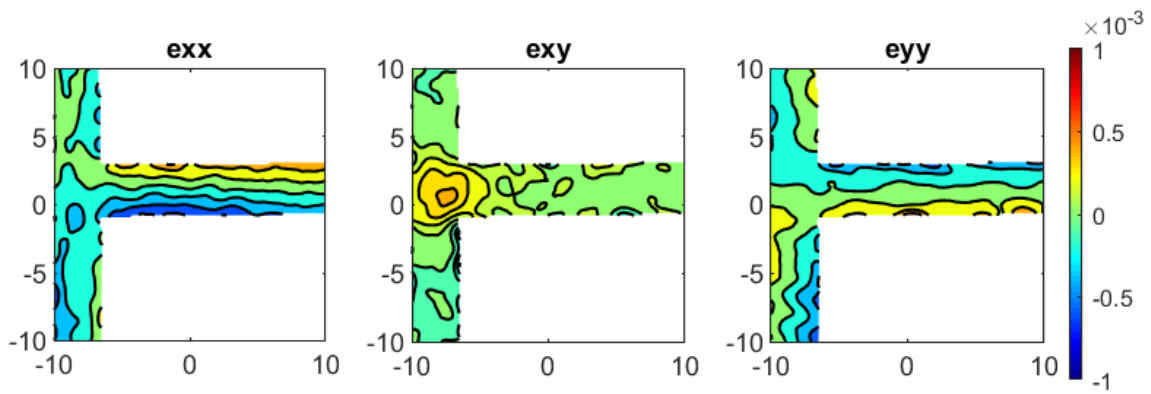
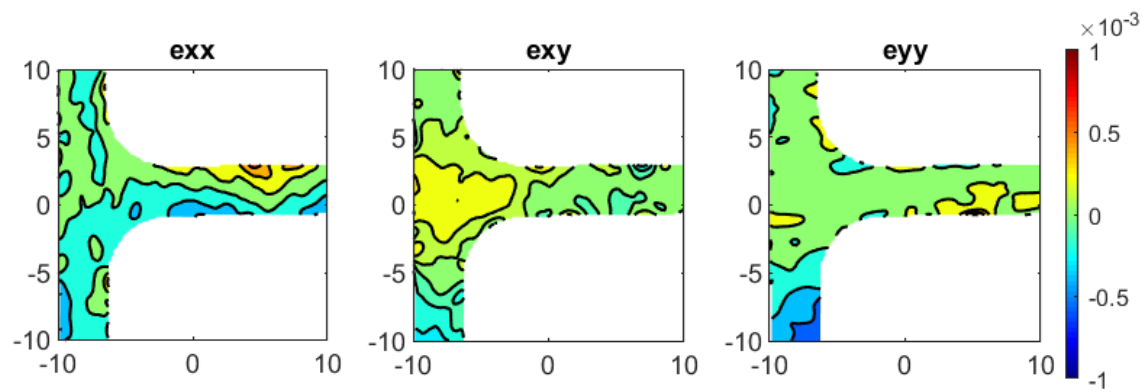


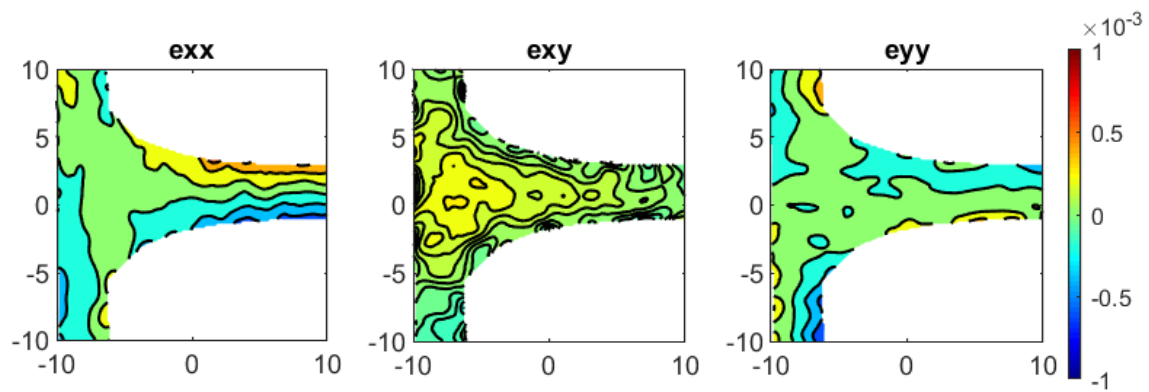
Fig. 10.3 The infinite node internal strains for a 1 [%] tip deflection



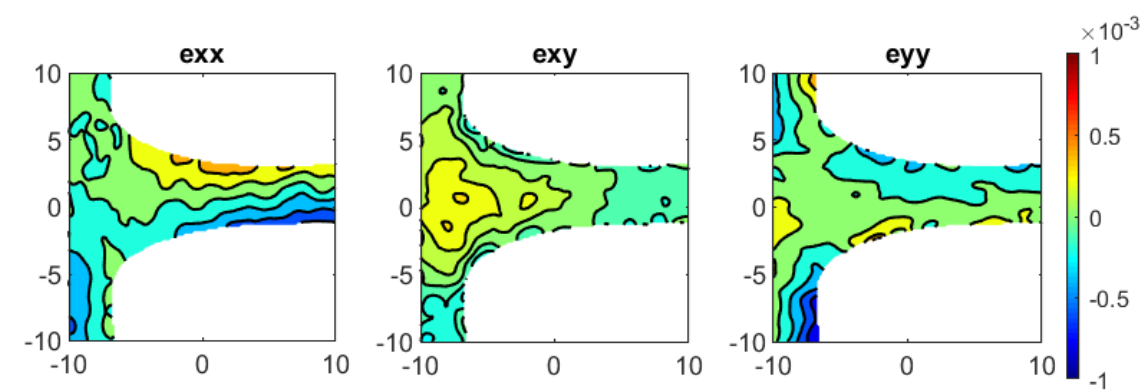
(a) Un-filletted



(b) Circular-filletted



(c) Mattheck-filletted



(d) Baud-filletted

Fig. 10.4 The finite node internal strains for a 1 [%] tip deflection

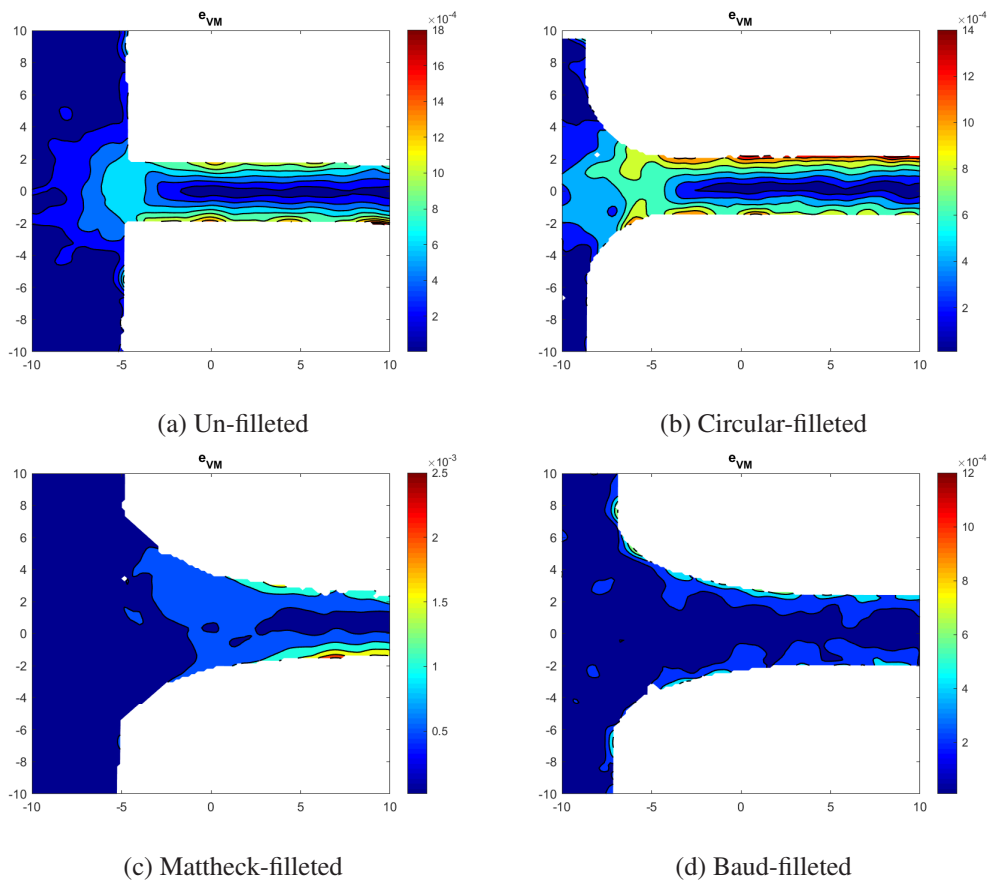


Fig. 10.5 The infinite-node equivalent Von Mises strains for a 1 [%] tip deflection

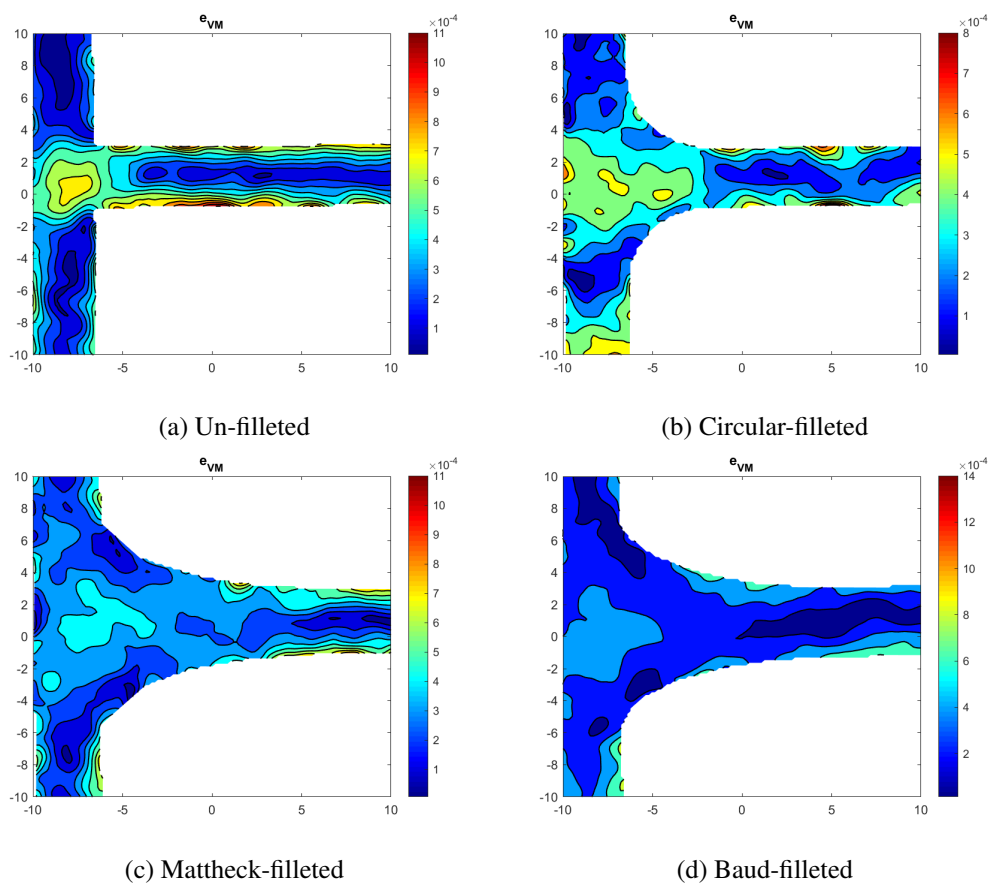


Fig. 10.6 The finite-node equivalent Von Mises strains for a 1 [%] tip deflection

minimum bending stiffness, and orientation according to Ashby & Gibson's models. By sticking with this interpretation, equivalent strut lengths can be found from the stress plateaux and compared to the actual strut lengths. From Equation 2.2,

$$l_{\text{eff,eb}} = \sqrt{\frac{0.686^2 \pi^2 EI_{\text{min}}}{P_{\text{crit}}}}, \quad (10.1)$$

where  $l_{\text{eff,eb}}$  is the effective length from the elastic buckling analysis,  $P_{\text{crit}}$  is assumed to be an even distribution of the total force  $F$  divided by the number of walls (in this case 4), and  $EI_{\text{min}}$  is the minimum stiffness of the cell wall. A value of 0.686 is assumed to hold true for the end fixities. Assuming that the un-filleted cellular solid indeed buckled, its  $l_{\text{eff,eb}}$  is 22.65 [mm] (1.42  $l$ ). The Mattheck-filleted cellular solid has an  $l_{\text{eff,eb}}$  of 17.15 [mm] (1.07  $l$ ).

Though these effective strut lengths are reductive, it allows for a more intuitive understanding of how fillets increase the rigidity and collapse force for a cellular solid, by wrapping the nodal fixity into a conceptualization where the node remains 1-D. The strut now addresses the end-fixity and the boundary between the two 'components'. This also has the advantage of allowing the re-use of Gibson & Ashby's models for modelling cellular solid performance and ask further questions.

The energy absorption characteristics of the circular-filleted and lumped-node specimens were similar in that the amount of energy absorbed by the specimens increased until their ultimate catastrophic failure - most probably cause by cell wall fracture. The Mattheck-filleted and un-filleted specimens underwent a levelling off of energy absorption rate per unit displacement. The Mattheck-filleted curve certainly softened in a post-yield regime after its vertical struts elastically buckled. The un-filleted baseline failed more suddenly with less softening.

A more realistic application of load would be better-represented by a force-controlled experiment. In such a context, the Mattheck-filleted specimen would fail earlier, and would likely absorb less energy, though the effects of nodal topology on strain rate is unknown and needs to be studied.

Even so, the amount of energy absorbed by the Mattheck-filleted curve is greater, and was achieved in a smaller deflection. For applications in which energy-absorbing material is applied to an engineering design, it is possible that both weight and volume is a defining parameter.

Although the effect of nodal topology on strain-rate is uncertain, it seems that further research into the nature of nodal topology for energy absorbing cellular solid structures is a promising direction to take. This is because the filleted cellular solids supported much higher ultimate forces in the same honeycomb height, making them interesting in engineering designs where space comes at a premium. This topic is revisited in Section 11.2.

Overall, strong evidence exists to disprove Hypotheses 1.1 and 2.1 outright: both strut deflection and cellular solid deflection rigidity seem highly sensitive to the nodal topology of strut bases or nodes, corroborating Dallago *et al.*'s observations in (Dallago et al., 2017), although with experimental evidence and in a much more obvious manner in terms of the difference in structural moduli.

Classical stress theory suggests that those fillets are able to reduce peak stresses, which would in turn mitigate the extent of nodal warping and its downstream propagation through adjoining struts in the form of strut displacement. Warping would cause load eccentricity; in mathematical terms, a node is effectively a strut's boundary condition - one that can be compromised from its ideal. This is an argument that Dallago *et al.* independently gave.

The above arguments were suspected to be relevant at the beginning of the project, culminating in the articulation of (null-) Hypotheses 1.2, 1.3, and 2.2 through to 2.4. The hypotheses pertained to the detailed nature of the nodal regions themselves. With lines of equipotential or isoclinics roughly following the outer free boundary of the nodal topologies in the case of the Mattheck- and Baud-filleted node-level specimens coinciding with apparently decreased effective strut lengths, and by observing stress homogenization in their detailed strain fields, it was thought that improved load transfer is the central cause of the improved deflection rigidity. Thus, Hypotheses 1.2 and 2.2 are thought to have been directly falsified by the experimental evidence, whereas 1.3 and 2.4 remain plausible.

## 10.2 Implications for further research and potential applications

Across scales, trends in the theoretical equivalent strut lengths that were the reduced mechanical performance of finite-level and cellular solid level struts were similar in that filleted nodes had smaller effective lengths. Evidence from the nodal-level experiments supports the notion that fillets mitigate the negative effects of highly localized stress concentrations, and seem to move critical regions from the nodal areas away from the node and into the strut.

Consequently, there are important implications here for the continued research into damage tolerant lightweight structures, structural health monitoring, and fatigue performance in tandem with continued research in cellular solids. Adding to those, applying this thinking to architectural and civil structural design, and to wound-composite joinery and other composite material materials are suggested.

Regarding structural health monitoring and damage tolerant cellular solid design, having a structure whose critical region is well-understood and precisely located, can improve the detection of damage. The design is somewhat analogous to the functionality of common household electric fuses. The user could then be alerted and switch to a less intensive usage mode until a more intensive assessment or repair is made.

Examining inspectability for a moment in detail: this point was encountered in the experiments themselves. The un-filleted and lumped-node specimens had nodes that were not directly observable by the DIC cameras and strain calculation process, whereas the filleted nodes were. The usefulness of this point is not just limited to optical inspectability. Applying strain gauges to relatively smooth struts is much more feasible than to discontinuous nodes.

A strict binary ‘fuse’ concept would be limited to damage. A softer definition might also be useful, perhaps by implementing a high (but accurate) stress raiser. Applying a strain gauge to an affected region would allow a structural component function similarly to a test-bench load cell, thereby recording precise structural usage logs. Not only would this improve inspection and maintenance, it might introduce new business models.

Another advantage to encourage damage to initiate in the strut instead of near the node: less of the network risks becoming compromised. A fracture initiating and propagating within the strut is preferable to one in the nodal region, as less of the structure is directly implicated or risked by that damage. It is much better to lose one strut instead of a node along with all of its adjoining struts.

With regard to implications for cellular solid fatigue performance, stress peaks in the structure for a given load may be homogenized to a more even level, increasing its fatigue life. For any designs that are already in use for cyclical load contexts, redesigning them may even bring them under the fatigue limit.

One potential criticism of the work done in this thesis is that the scale at which parts must be fabricated are relatively large: enough resolution must be available to control the precise nature of nodal topologies. But consider the following statement: it is better to maintain relatively tight controls over nodal topology to homogenize stress, than to relinquish it and produce stress-raisers. After all, there are large differences between lightening holes in aircraft spars and sharp notches or cracks. The argument is more of an analogy than a water-tight explanation backed by empirical evidence; it is clear that more work needs to be done.

In architectural or civil engineering contexts, large-scale deposition modeling-like processes are beginning to be used, where concretes are 3-D printed in layers to produce novel structures. Filleting macro-scale notches in a similar fashion to that of the cellular solid specimens in this thesis might conceivably deliver performance and cost-improvements, as well as being more aesthetic. More research would need to be done to investigate this claim.

Lastly, filament-wound carbon fiber tubes are currently used to make high-performance lightweight structures like race vehicles. Joining them using lightweight parts remains difficult. By applying the lessons regarding nodal topology and load transfer from this preliminary investigation, lightweight parts might be fabricated to give a balance between providing stiffness, load transfer, and enough compliance to improve overall structural performance.





# Chapter 11

## Conclusions & Recommendations

*What is the effect of nodal topology on cellular solid mechanics?*

### 11.1 Conclusions

In the available literature, almost nothing was known about nodal topology in cellular solids; much is known about stress concentration factors and beam models. On its face, applying classical stress-reduction design methods to nodal points seems like a straightforwardly favorable proposition.

Many of nature's designs feature stress-reducing curves. Natural cellular solids are not exceptions to this fascinating pattern. Avian long bones have particularly low relative densities, offering lightweight bending stiffness and an integration with the peculiar ornithological pulmonary and circulatory systems. Streamlined struts bridge the extremely thin outer walls, forming smooth spacious vaults within.

Nature has it right. Stress-reducing fillet geometries increased strut deflection rigidities on both the nodal- and cellular solid- levels. As a result, null-Hypotheses 1.1 and 2.1 were falsified. The fillets successfully stiffened the strut-node combination to varying extents on the nodal-level, with the bioinspired curves coming out on top. On the cellular solid-level, the initial deflection rigidities of both fillets achieved similar results early on, but seemed to behave very differently in failure; the bioinspired Mattheck curve seemed to strengthen the nodal region enough to cause buckling to occur. From there, it seems that a crushing fracture initiated in the strut.

On the nodal-scale, the increase in deflection rigidity occurred simultaneously with an improved load transfer through the nodal region. This was observed using DIC apparatus and analysis methods. The filleted nodes were able to activate the base material much better in both the infinite- and finite-node cases: equivalent Von Mises stress was more homogeneous.

Meanwhile, the un-filleted node experienced high-stress gradients that did not conform as well to the free boundary. These observations were also clearly observable in the basic stress distributions for  $\epsilon_x$ ,  $\epsilon_y$  and  $\tau_{xy}$ .

Table 11.1 Current status of the hypotheses

ID	Hypothesis	Status
1.1	Mass-normalized strut deflection rigidity is unaffected by nodal topology.	False
1.2	Strut stress fields and their homogenization are unaffected by nodal topology.	False
1.3	If stress homogenization in a bending structure improves, then that structure will increase in its mass-normalized strut deflection rigidity.	Plausible
2.1	Mass-normalized cellular solid deflection rigidity is unaffected by nodal topology.	False
2.2	Stress homogenization in a cellular solid is unaffected by nodal topology.	False
2.3	If stress homogenization improves, then a cellular solid will increase in its mass-normalized deflection rigidity.	Plausible
2.4	If stress homogenization improves, then a cellular solid will become less sensitive to localized stress gradients and their effects, thereby increasing the height of the so-called stress plateau.	Plausible

Overall, it seemed that fillets were able to effectively expand the ‘nodal zone’ with a conjugal reduction in effective strut length. On the cellular solid level, the height of the so-called bathtub curves differed according to fillet shape. Overall, this indicates that null Hypotheses 1.2 and 2.2 were falsified.

Effective strut lengths were calculated across scales as a simple way to investigate and capture the reduction in functional strut length, and an increase in end-fixity. The results indicate a decreasing effective length for improving fillet geometry, and an increasing end-fixity coefficient. This supports the if-then Hypothesis 1.3.

On the cellular solid-level, changing bathtub heights coincided with higher stress plateaux as well, though the extent of stress-homogenization was not observed completely. Inspecting the experimental debris indicates that stress was better-distributed in the filleted honeycombs as they fractured in the cell walls, and not in the nodes. This was in stark contrast to the un-filleted nodal honeycombs that did fracture at the sharp notch of un-filleted nodal points. Together, these observations indicate that if-then Hypotheses 2.3 and 2.4 remain reasonable. A summary is given in Table 11.1.

In summary, stress-reducing fillet geometries were used as a vehicle to explore nodal topology effects. It seems that low density cellular solids are highly sensitive to nodal topology across both scales of analysis.

## 11.2 Recommendations

A number of recommendations for future research can be made that carry from the discussion presented in Chapter 10 and from Section 11.1. The recommendations have taken the form of open research questions which have prompted a further evaluation of the work done in this thesis.

### 1. **What is the cause of cellular solid nodal softening and its corresponding effects on cellular solid mechanics?**

In cellular solids, *softening* is the phenomenon of material effectively *seizing up* inside lattices, or locally yielding at edge-cells due to a lack of constraint. In this thesis, un-filleted nodes had highly localized regions of stress concentration and large stress gradients which seemed to affect cellular solid mechanics such as the initial deflection rigidity. Filleted nodes were seemingly less affected by these phenomena, though to varying extents.

An investigation of specimen debris at the cellular solid level indicated that sharp notches induce failure at the notch, whereas those whose notches were filleted broke at the minimum cross-sectional area of the strut. On the nodal level, the Baud curve seemingly increased the apparent stiffness of the entire finite strut, as well as eliminated the free boundary stress concentration through stress-homogenization.

In summary, the precise nature of those effects remain unknown, and thus need to be examined more closely. From the work performed in this thesis, it was clear that the actual moment distribution in the struts were far from their idealized shapes. Modelling and measuring the load distributions of the filleted struts more accurately might prove a good start. Solving Airy stress functions for the equilibrium reached in the nodal region is one possibility.

### 2. **How can stress-reducing cellular solid fillet geometries be applied to 3-D open cell structures?**

In this study, stress reducing nodal geometries based upon a 2-D extruded shape were examined. There is no obvious extension of these shapes for generalized 3-D lattice nodes, whose shape cannot be reduced as easily. Numerous lattice structures being used in the biomedical and aerospace engineering fields are comprised of lattices made of ligaments with circular cross-sections. A means to extend the 2-D geometries to accommodate the intersections of circular rods thus needs to be addressed.

### 3. **Is it certain that the curing and post-curing effects are negligible?**

In this study, stress reducing nodal geometries based upon a 2-D extruded shape were examined. The specimen fabrication and post treatments were repeated using manufacturer recommendations. It was assumed that the specimens did not differ in their performance due to material or process-dependent variables such as microstructure or residual stress distributions. Were this a more exhaustive post-doctoral research paper, such tests would have been carried out to ensure

that geometry was indeed specifically targeted as the free variable space. This was beyond the scope and time-scale of this Master of Science thesis.

**4. Can a nodal grading tool be developed to fine-tune finite cellular solid structure deflection requirements of lightweight damage-tolerant structures?**

In high-performance lightweight structures, supporting advanced functionality is challenging; systems integration, structural inspection, and damage tolerance come on top of structural requirements in numerous aerospace applications. In this study, it was observed that cellular solids have a high sensitivity to nodal topology on a mass-basis, and that filleted nodes were more easily inspected with DIC. The latter translates well to strain gauge application. A tool that negotiates the various performance requirements by providing the required stiffness and forcing specific failure modes to occur is an exciting idea. Perhaps a study comparing the effects of strut diameter and relative fillet size needs to be addressed on a mass-basis. Another idea is to study the sensitivity of asymmetrical nodal topology on strut buckling direction.

**5. Can a nodal grading tool be developed to fine-tune finite cellular solid structure deflection requirements of lightweight damage-tolerant structures?**

In high-performance lightweight structures, supporting advanced functionality is challenging; systems integration, structural inspection, and damage tolerance come on top of structural requirements in numerous aerospace applications. In this study, it was observed that cellular solids have a high sensitivity to nodal topology on a mass-basis; cellular solid deflection rigidity seems to be directly affected. Currently, cellular solid continua have well-understood mechanical properties. In the biomedical and aerospace engineering fields (to name a few), the application of cellular solids is limited to a target volume. In other words the edges conform to some arbitrary shape. Edge cells tend to have different and often undesired mechanical properties. An ability to cause a similar structural response in these areas through the systematic application of nodal grading could be a solution.

**6. Can cellular solid nodal fillets be optimized to cause adjoining struts to fail with high reliability in easily-inspected regions using structural health monitoring concepts and hardware to create tomorrow's lightweight damage-tolerant structures?**

In this study, it was observed that cellular solids with filleted nodes were more easily inspected with DIC. This also translates well to the application of other transducers such as strain gauges. A future engineering thesis might consider the redesign of an aerospace component whose design is made up of cells and a structural 'fuse' to be monitored with SHM technology. The fuse would in this context be a strut which provides insight into real-time structural performance according to its design requirements. Such work would be a practical preliminary investigation of the wider research question, helping engineers and companies to envisage smarter designs. Although it is not a scientific help, it might also be a project that might help secure funding for further cellular solid research.

**7. What is the effect of nodal topology on strain rate sensitivity of a compressing cellular solid?**

In this study, it was observed that cellular solids are highly sensitive to nodal topology. The experimental evidence was gathered under quasi-static conditions. The results show that the filleted cellular solids are more effective in a defined space than their unfilleted counterparts; these improved designs are able to withstand higher loads, and transform the work done on the system into material strain more effectively. In design contexts where energy absorption is a key functionality for the cellular solid, it is not just these capacities that matter, but also the speed at which the force is applied. Examples could include blast-protection in military personnel vehicles, impact shields on-board satellites, improved automotive crush zones, airplane crush zones, *et cetera*. A means to extend the analysis to these high-energy impact situations is needed, and thus the issue of strain rate sensitivity needs to be addressed specifically.

**8. How can the lessons from this thesis be applied to produce lightweight joints for filament-wound carbon fiber tubes?**

**9. How can the lessons from this thesis be applied to bigger scale architectural and civil designs?**



# References

- Diab W. Abueidda, Mete Bakir, Rashid K. Abu Al-Rub, Jörgen S. Bergström, Nahil A. Sobh, and Iwona Jasiuk. Mechanical properties of 3D printed polymeric cellular materials with triply periodic minimal surface architectures. *Materials and Design*, 122:255–267, 2017. ISSN 18734197. doi: 10.1016/j.matdes.2017.03.018.
- Agricultural Research Service. Soybean cyst nematode and egg, 2006. URL [https://en.wikipedia.org/wiki/File:Soybean\\_cyst\\_nematode\\_and\\_egg\\_SEM.jpg](https://en.wikipedia.org/wiki/File:Soybean_cyst_nematode_and_egg_SEM.jpg).
- M.F. Ashby. The properties of foams and lattices. *Philosophical Transactions of the Royal Society A: Mathematical, Physical and Engineering Sciences*, 364(1838):15–30, 2006. ISSN 1364-503X. doi: 10.1098/rsta.2005.1678. URL <http://rsta.royalsocietypublishing.org/cgi/doi/10.1098/rsta.2005.1678>.
- M.F. Ashby. *Materials Selection in Mechanical Design*. Elsevier, Oxford, 4th edition, 2011. ISBN 978-1-85617-663-7.
- R.V. Baud. *Beiträge zur Kenntnis der Spannungsverteilung in prismatischen und keilförmigen Konstruktionselementen mit Querschnittübergängen*. PhD thesis, ETH Zürich, 1934. URL <https://www.research-collection.ethz.ch/bitstream/handle/20.500.11850/133642/eth-20779-01.pdf>.
- Barényi Béla. Kraftfahrzeug, insbesondere zur Beförderung von Personen, 1949. URL <https://www.dpma.de/ponline/erfindergalerie/patente/de854157.pdf>.
- Victor Birman and Larry W. Byrd. Modeling and Analysis of Functionally Graded Materials and Structures. *Applied Mechanics Reviews*, 2007. ISSN 00036900. doi: 10.1115/1.2777164.
- Daimler. Patent No. DBP 854 157, life-saver of thousands, 2009. URL <http://media.daimler.com/marsMediaSite/en/instance/ko/Patent-No-DBP-854-157-life-saver-of-thousands.xhtml?oid=9913733>.
- M. Dallago, M. Benedetti, V. Luchin, and V. Fontanari. Orthotropic elastic constants of 2D cellular structures with variously arranged square cells: The effect of filleted wall junctions. *International Journal of Mechanical Sciences*, 122(December 2016):63–78, 2017. ISSN 00207403. doi: 10.1016/j.ijmecsci.2016.12.026.
- Charles Darwin. *On the origin of species by means of natural selection, or, the preservation of favoured races in the struggle for life*. J. Murray, London, 1859.
- V S Deshpande, M.F. F Ashby, and N A Fleck. Foam Topology Bending Versus Stretching Dominated Architectures. *Acta Materialia*, 49(6):1035–1040, 2001. doi: [https://doi.org/10.1016/S1359-6454\(00\)00379-7](https://doi.org/10.1016/S1359-6454(00)00379-7). URL <https://www.sciencedirect.com/science/article/abs/pii/S1359645400003797>.

- Erik Eckermann. Vom Bestohlenen zur Heiligsprechung Zum hundertsten Geburtstag von Béla Barényi. *ATZ - Automobiltechnische Zeitschrift*, 109(12):1136–1141, 2000. URL <https://link-springer-com.tudelft.idm.oclc.org/article/10.1007%2F03221939>.
- R P Feynman, B Gates, and R Leighton. *"Surely You're Joking, Mr. Feynman!": Adventures of a Curious Character*. W. W. Norton, 2018. ISBN 9780393355680. URL [https://books.google.co.uk/books?id=\\_gA\\_DwAAQBAJ](https://books.google.co.uk/books?id=_gA_DwAAQBAJ).
- Formlabs. Materials Data Sheet Photopolymer Resin for Form 1+ and Form 2, 2018. URL <https://formlabs.com/media/upload/XL-DataSheet.pdf>.
- Guy M. Genin, Alistair Kent, Victor Birman, Brigitte Wopenka, Jill D. Pasteris, Pablo J. Marquez, and Stavros Thomopoulos. Functional grading of mineral and collagen in the attachment of tendon to bone. *Biophysical Journal*, 97(4):976–985, 2009. ISSN 15420086. doi: 10.1016/j.bpj.2009.05.043. URL <http://dx.doi.org/10.1016/j.bpj.2009.05.043>.
- L.J. Lorna J. Gibson and M.F. Ashby. *Cellular solids : structure and properties*. Cambridge University Press, Cambridge, 2nd editio edition, 1997. ISBN 9781139878326. doi: 10.1017/CBO9781139878326.
- Lorna J. Gibson. Biomechanics of cellular solids. *Journal of Biomechanics*, 38(3):377–399, 2005. ISSN 00219290. doi: 10.1016/j.jbiomech.2004.09.027.
- T. C. Hales. The honeycomb conjecture. *Discrete and Computational Geometry*, 25(1):1–22, 2001. ISSN 01795376. doi: 10.1007/s004540010071.
- Honathan Harris. SLM Lattices II, 2014. URL <https://www.flickr.com/photos/cambridgeuniversity-engineering/14144565606>.
- W.C. Hayes and T.M Keaveny. Mechanical properties of cortical and trabecular bone, 1993. URL [https://www.researchgate.net/publication/272152350\\_Mechanical\\_properties\\_of\\_cortical\\_and\\_trabecular\\_bone](https://www.researchgate.net/publication/272152350_Mechanical_properties_of_cortical_and_trabecular_bone).
- Cornelius O. Horgan and James K. Knowles. Recent Developments Concerning Saint-Venant's Principle. *Advances in Applied Mechanics*, 23:179–269, 1 1983. ISSN 0065-2156. doi: 10.1016/S0065-2156(08)70244-8. URL <https://www.sciencedirect.com/science/article/pii/S0065215608702448>.
- Dalia Mahmoud and Mohamed Elbestawi. Lattice Structures and Functionally Graded Materials Applications in Additive Manufacturing of Orthopedic Implants: A Review. *Journal of Manufacturing and Materials Processing*, 1(2):13, 2017. ISSN 2504-4494. doi: 10.3390/jmmp1020013. URL <http://www.mdpi.com/2504-4494/1/2/13>.
- C. Mattheck. *Secret Design Rules of Nature*. Forschungszentrum Karlsruhe GmbH, Karlsruhe, 1st edition, 2007. ISBN 978-3-923704-62-0.
- C Mattheck. *Thinking Tools After Nature*. KS Druck GmbH, Karlsruhe, first edition, 2011. ISBN 978-3-923704-75-0.
- C Mattheck and S Haller. The Force Cone Method : A New Thinking Tool for Lightweight Structures. *International Journal of Design & Nature and Ecodynamics*, 8(2): 165–171, 2013. doi: 10.2495/DNE-V8-N2-165-171. URL <https://www.witpress.com/elibrary/wit-transactions-on-ecology-and-the-environment/160/23394>.



- C. Mattheck, R. Kappel, and A. Sauer. Shape optimization the easy way: the method of tensile triangles. *International Journal of Design & Nature*, 2(4):301–309, 2007. doi: 10.2495/D{\&}N-V2-N4-301-309. URL <https://www.witpress.com/elibrary/DNE-volumes/2/4/313>.
- Lauren Montemayor, Victoria Chernow, and Julia R. Greer. Materials by design: Using architecture in material design to reach new property spaces. *MRS Bulletin*, 40(12):1122–1129, 2015. ISSN 0883-7694. doi: 10.1557/mrs.2015.263. URL [http://www.journals.cambridge.org/abstract\\_S0883769415002638](http://www.journals.cambridge.org/abstract_S0883769415002638).
- Lewis Mullen, Robin C. Stamp, Wesley K. Brooks, Eric Jones, and Christopher J. Sutcliffe. Selective laser melting: A regular unit cell approach for the manufacture of porous, titanium, bone in-growth constructs, suitable for orthopedic applications. *Journal of Biomedical Materials Research - Part B Applied Biomaterials*, 89(2):325–334, 2009. ISSN 15524973. doi: 10.1002/jbm.b.31219.
- Lewis Mullen, Robin C. Stamp, Peter Fox, Eric Jones, Chau Ngo, and Christopher J. Sutcliffe. Selective laser melting: A unit cell approach for the manufacture of porous, titanium, bone in-growth constructs, suitable for orthopedic applications. II. Randomized structures. *Journal of Biomedical Materials Research - Part B Applied Biomaterials*, 92(1):178–188, 2010. ISSN 15524973. doi: 10.1002/jbm.b.31504.
- Lawrence Murr, Sara Gaytan, Edwin Martinez, Francisco Medina, and Ryan B Wicker. Next Generation Orthopaedic Implants by Additive Manufacturing Using Electron Beam Melting. *International journal of biomaterials*, 2012:245727, 2012. doi: 10.1155/2012/245727.
- Patrick M. O’Connor and L. P A M Claessens. Basic avian pulmonary design and flow-through ventilation in non-avian theropod dinosaurs. *Nature*, 436(7048):253–256, 2005. ISSN 00280836. doi: 10.1038/nature03716.
- OpenStax. *Anatomy & Physiology*. Rice University, 2016. URL <http://cnx.org/contents/14fb4ad7-39a1-4eee-ab6e-3ef2482e3e22@8.24>.
- Walter D. Pilkey and Deborah F. Pilkey. *Peterson’s Stress Concentration Factors*. John Wiley & Sons, Inc., Hoboken, 3rd edition, 2008. ISBN 9780470048245. doi: 10.1002/9780470211106.
- R.B Heywood. *Photoelasticity for designers*. Pergamon, 1 edition, 1965. ISBN 9781483151953. URL <https://www.elsevier.com/books/photoelasticity-for-designers/heywood/978-0-08-013005-7>.
- Antonella Sola, Devis Bellucci, and Valeria Cannillo. Functionally graded materials for orthopedic applications – an update on design and manufacturing. *Biotechnology Advances*, 34(5):504–531, 2016. ISSN 07349750. doi: 10.1016/j.biotechadv.2015.12.013. URL <http://dx.doi.org/10.1016/j.biotechadv.2015.12.013>.
- Tarah N. Sullivan, Bin Wang, Horacio D. Espinosa, and Marc A. Meyers. Extreme lightweight structures: avian feathers and bones. *Materials Today*, 20(7):377–391, 2017. ISSN 18734103. doi: 10.1016/j.mattod.2017.02.004. URL <http://dx.doi.org/10.1016/j.mattod.2017.02.004>.
- Derron van Helvoort. Data: The effect of nodal topology on cellular solid mechanics - A preliminary diagnostic experimental investigation, 2018. URL <https://osf.io/j9zra/>.
- W. C. Young and R. G. Budynas. *Roark’s Formulas for Stress and Strain*. McGraw-Hill Companies, Inc., New York, 7th edition, 2002. ISBN 007072542X. doi: 10.1002/9780470974414.part3. URL <http://www.amazon.com/dp/007072542X>.
- Zachary Zguris. How Mechanical Properties of Stereolithography 3D Prints are Affected by UV Curing. Technical report, Formlabs, 2018. URL <https://formlabs.com/media/upload/How-Mechanical-Properties-of-SLA-3D-Prints-Are-Affected-by-UV-Curing.pdf>.

Chaoqun Zhang, Daniel A. Mcadams, and Jaime C. Grunlan. Nano/Micro-Manufacturing of Bioinspired Materials: a Review of Methods to Mimic Natural Structures. *Advanced Materials*, 28(39): 8566, 2016. ISSN 15214095. doi: 10.1002/adma.201604494.



---

# Appendices

---



# A Young's modulus analysis

According to the standard material datasheets, the Clear resin is comparable to Gray resin (Formlabs, 2018). In Formlabs white paper (Zguris, 2018), ASTM D638 type IV tensile bars were printed in Clear Resin V2 with Formlabs Form 1+ and Form 2 printers at a layer height of 100 micrometers [ $\mu\text{m}$ ] and tested quasi-statically using a Universal Testing Machine model 500LB equipped with a model SM-500-294 load cell and model 3542-0100-050-ST extensometer. The experimental Young's Modulus was obtained for different cure station temperatures for a wavelength of 405 nanometers [nm]. This data is presented in Figure A.1, where the size of the error bars is said to represent each datapoint's "standard deviation for the mean of four samples" (Zguris, 2018). The author interpreted this as the sample mean. These results indicate a leveling-off at 117.7 kips per square inch (812 [kPa]) for 60 minutes at 60 degrees Celsius [ $^{\circ}\text{C}$ ], with a 66.6 [%] confidence interval bound of  $\pm 13.8$  [%] for an estimated population mean using basic statistics and assuming a normal distribution of random error.

All of the experimental specimens were made from Gray V4 on a Form 2 printer and cured for the recommended cure time of 60 minutes at 60 [ $^{\circ}\text{C}$ ] at a wavelength of 405 [nm] using the Formlabs Cure Station. It is assumed that layer height and short wash-cycles in the recommended isopropyl alcohol do not affect material properties. The white paper's E-modulus scatter at this cure setting is considered representative. The precise details regarding the fabrication and post-processing of all samples can be found at (van Helvoort, 2018).

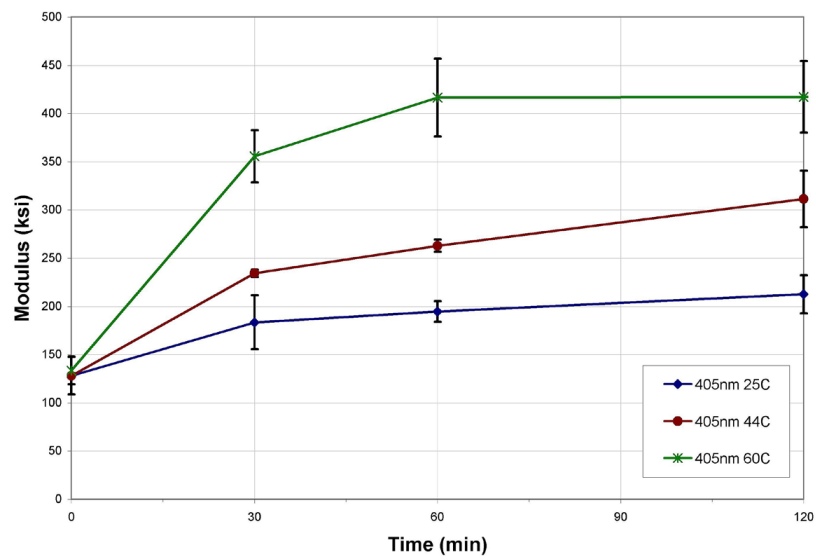


Fig. A.1 The Young's modulus of Formlabs resin dependence on time (Zguris, 2018)

# **B Experiment development and further information**

## **B.1 Specimen clamping**

Initially, the infinite nodes were clamped by tightly sandwiching the plate between two thick steel plates and securing them to the test bench. This made the test environment cluttered. This is a significant problem with the highly sensitive DIC equipment. Specimen alignment was also difficult to control across specimens. A dedicated clamp was fabricated such that specimens were easily introduced and removed from the test environment.

The finite nodes were initially secured to a construction that was already available in the DASML. In this setup, the support struts were secured with thumb-screws which limited nodal rotations. It was also difficult to align the specimens correctly with the rest of the test setup. A dedicated clamp was also fabricated such that specimens could easily be introduced and removed from the test environment.

## **B.2 Specimen preparation**

An ideal DIC speckle pattern should be random, sharp and high-contrast distribution of speckles against a continuous background to mitigate the risk of aliasing and non-convergence. Furthermore, the ideal speckle pattern should be scaled and distributed in such a way that the CCD of the DIC cameras are able to independently resolve each speckle from its neighbors.

As the camera resolution, field of view and focal length of the lenses all evolved in parallel development processes, the ideal speckle pattern changed to be developed accordingly. With the equipment available at DASML, the author soon gave up on reproducing an ideal speckle pattern. Instead, a more workable process was created. First, the DIC cameras and the necessary lights set up and calibrated. Second, speckle patterns were painted on different targets using a spray can with a fully-open nozzle from different distances. Those targets were then placed in the test area, and the best pattern was chosen. The actual test specimens were then taken to the paint room, and the best process was applied to all of them as evenly as possible.

Notable application issues include: graying out the background with overly-fine paint speckles; high resultant variability in individual speckle sizes; differences between resultant speckle patterns between specimens; and applying an uneven paint thickness.

### **B.3 Camera and lighting considerations**

Several issues were resolved regarding camera and lighting considerations:

- The angle between the two cameras in the stereoscopic camera set-up began at a suggested value of approximately  $30^\circ$  but was gradually decreased in favor of increased accuracy in the  $xy$  plane.
- The area of interest was reduced to prioritize observing the strain field of the nodal area in increasing detail. The focal depth became the limiting factor.
- Initially, only one set of DIC cameras were used to observe the section view. This meant that the free boundary could not be observed directly. Thus, a second DIC setup with a smaller focal length was placed inside the setup to observe the free-boundary deformation of the strut.
- Lighting seemed to affect DIC noise significantly. As the author and independent colleagues in the Delft University of Technology's DASML became more experienced lighting became more tightly controlled with the use of light-absorbent materials, powerful lights, smaller camera apertures and faster shutter speeds where possible.

### **B.4 Specimen technical drawings**

#### **Infinite node**

The specimen drawings are given according to the American Projection convention in Figures B.1 to B.4.

#### **Finite node**

The specimen drawings are given according to the American Projection convention in Figures B.5 to B.8.

#### **Hexagonal honeycomb specimens**

The specimen drawings are given according to the American Projection convention in Figures B.9 to B.12.



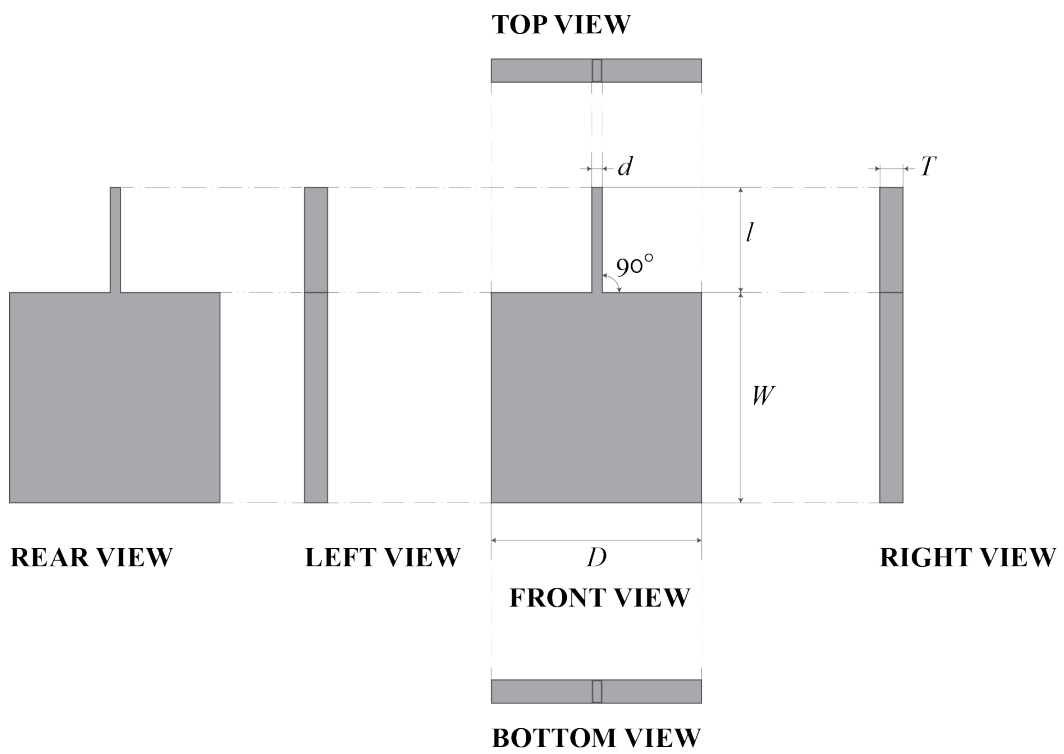


Fig. B.1 Technical drawing of the un-filletted infinite node specimen, employing the American projection convention

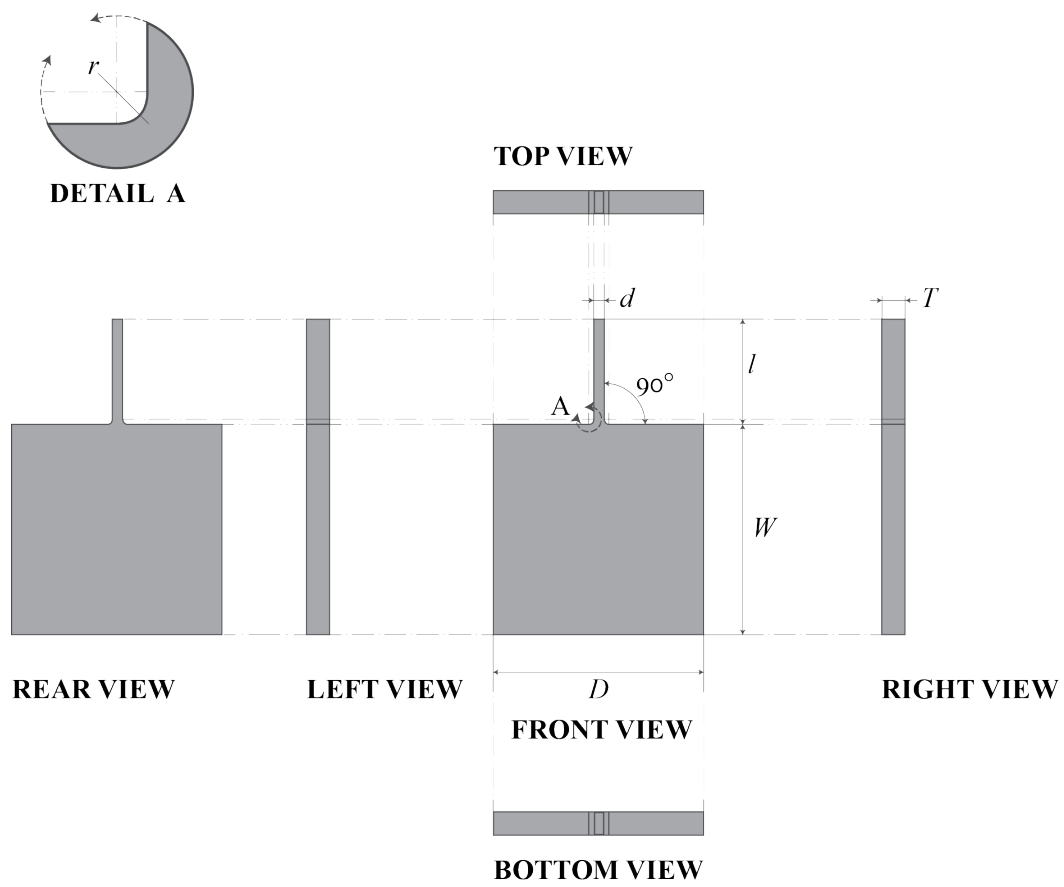


Fig. B.2 Technical drawing of the circular-filleted infinite node specimen, employing the American projection convention

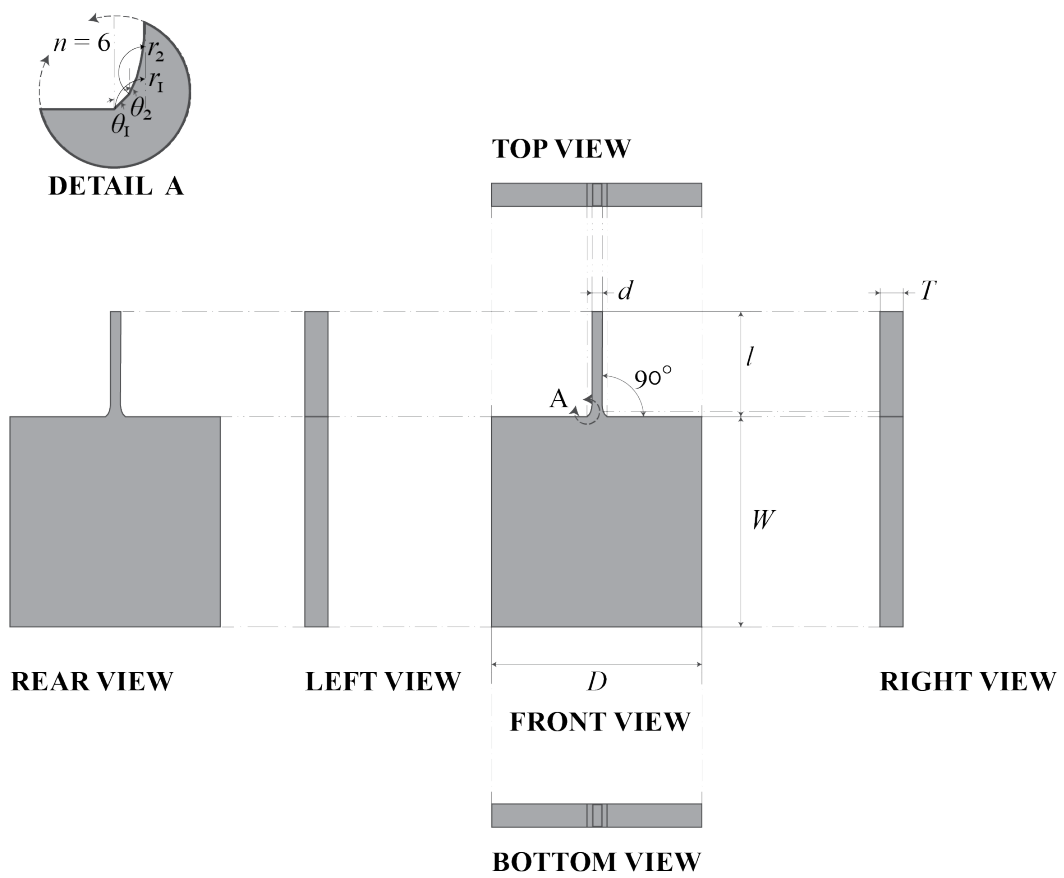


Fig. B.3 Technical drawing of the Mattheck-filletted infinite node specimen, employing the American projection convention

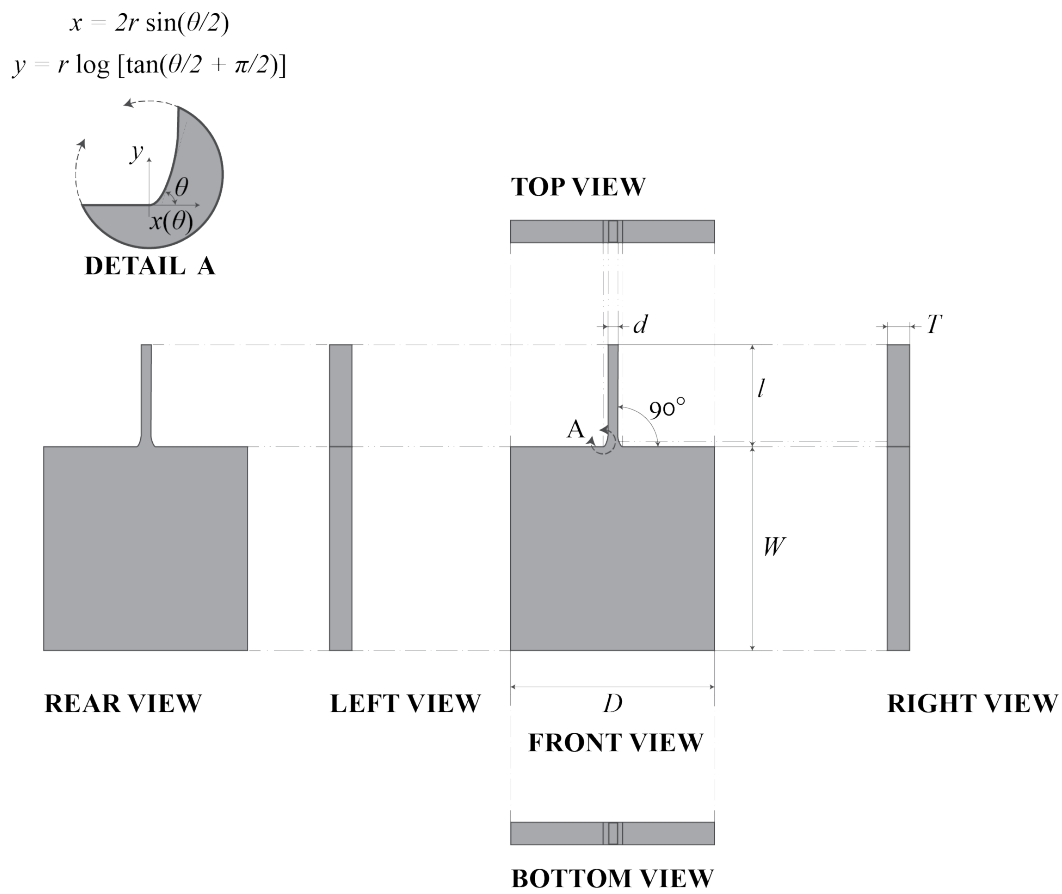


Fig. B.4 Technical drawing of the Baud-filletted infinite node specimen, employing the American projection convention

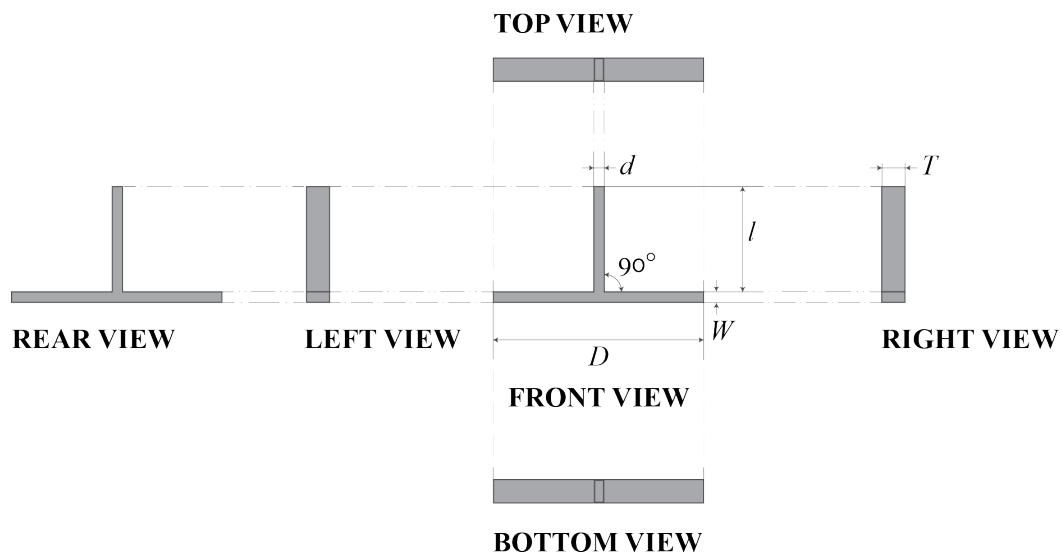


Fig. B.5 Technical drawing of the un-filletted finite node specimen, employing the American projection convention

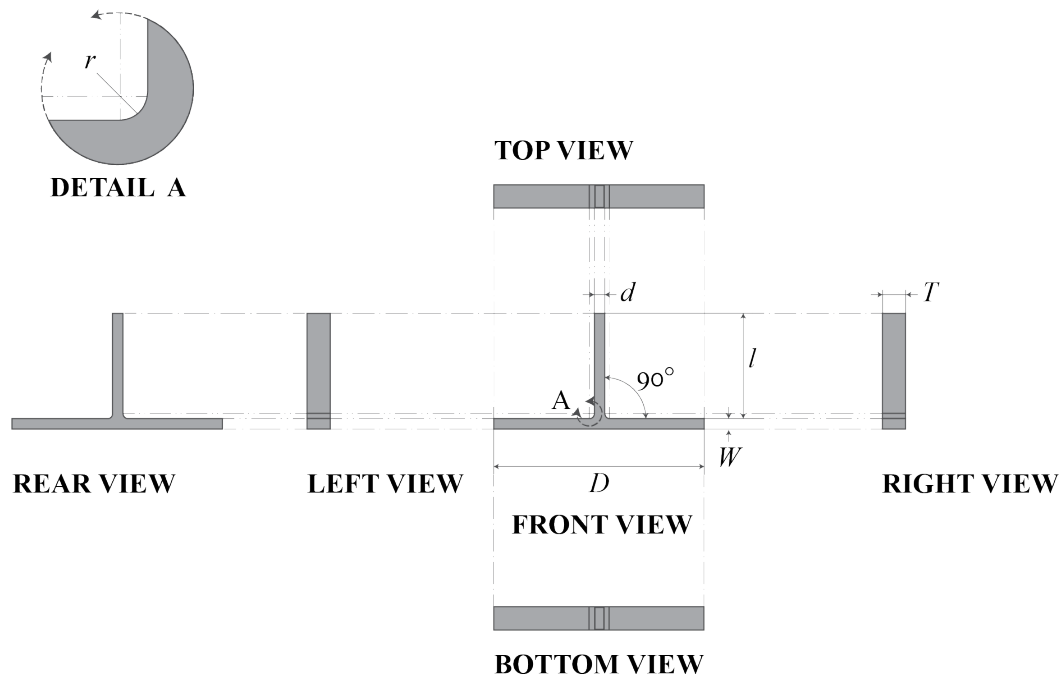


Fig. B.6 Technical drawing of the circular-filleted finite node specimen, employing the American projection convention

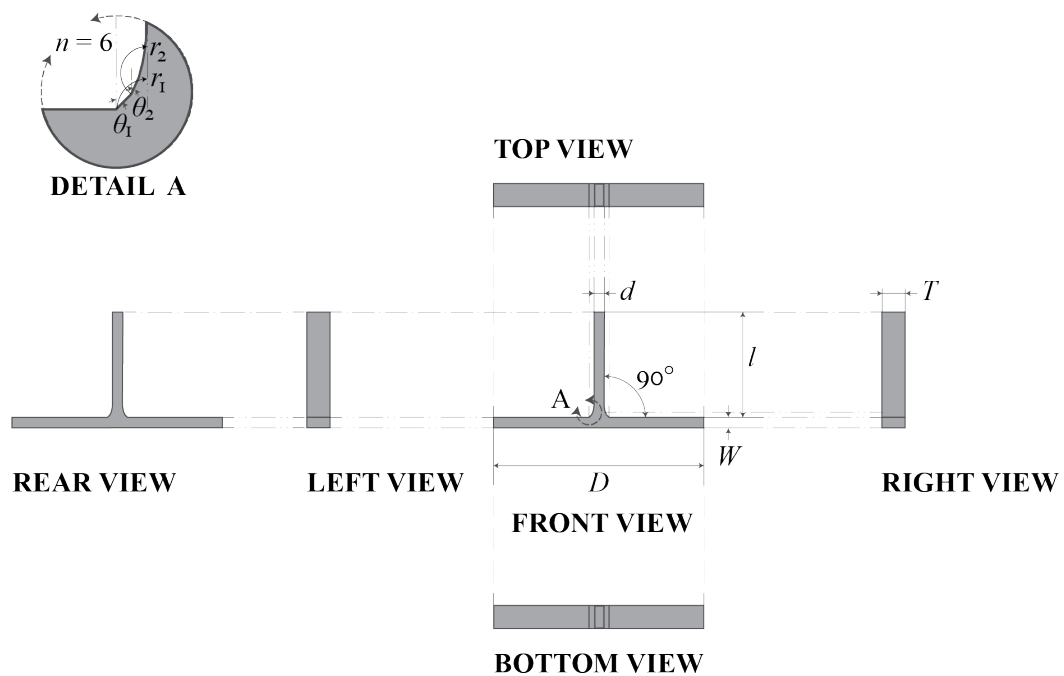


Fig. B.7 Technical drawing of the Matheek-filleted finite node specimen, employing the American projection convention

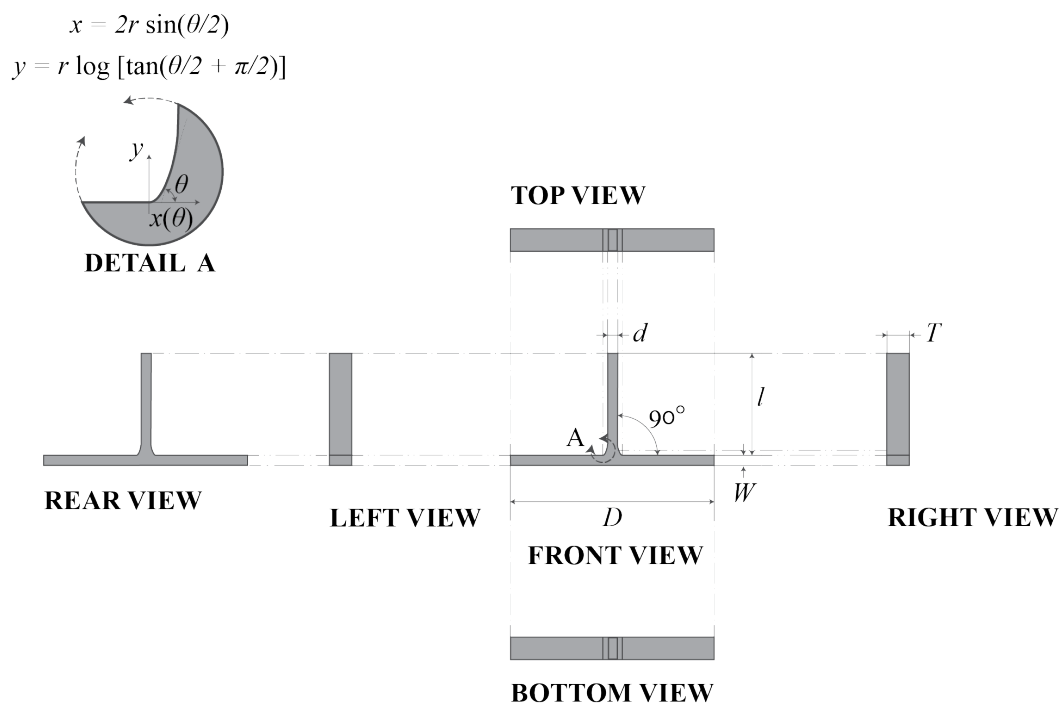


Fig. B.8 Technical drawing of the Baud-filletted finite node specimen, employing the American projection convention

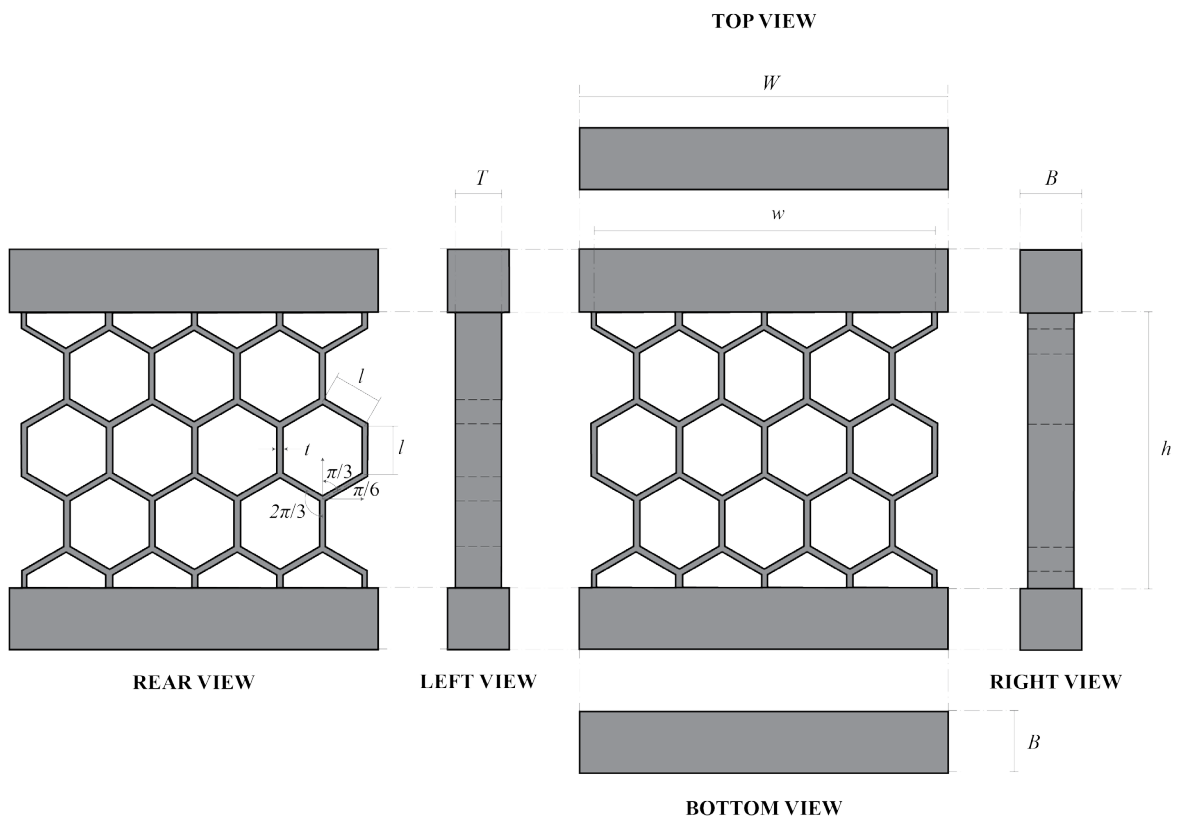


Fig. B.9 Technical drawing of the un-fulleted hexagonal honeycomb specimen, employing the American projection convention

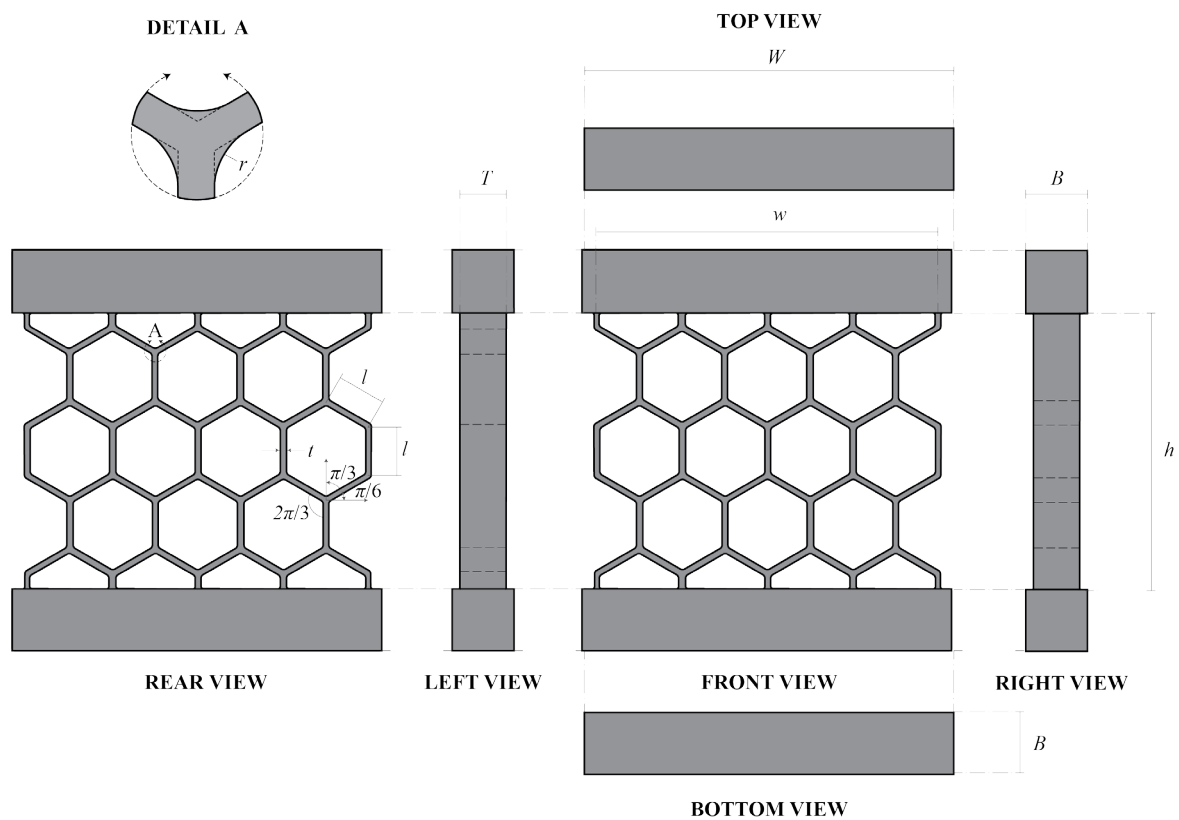


Fig. B.10 Technical drawing of the circular-filleted hexagonal honeycomb specimen, employing the American projection convention



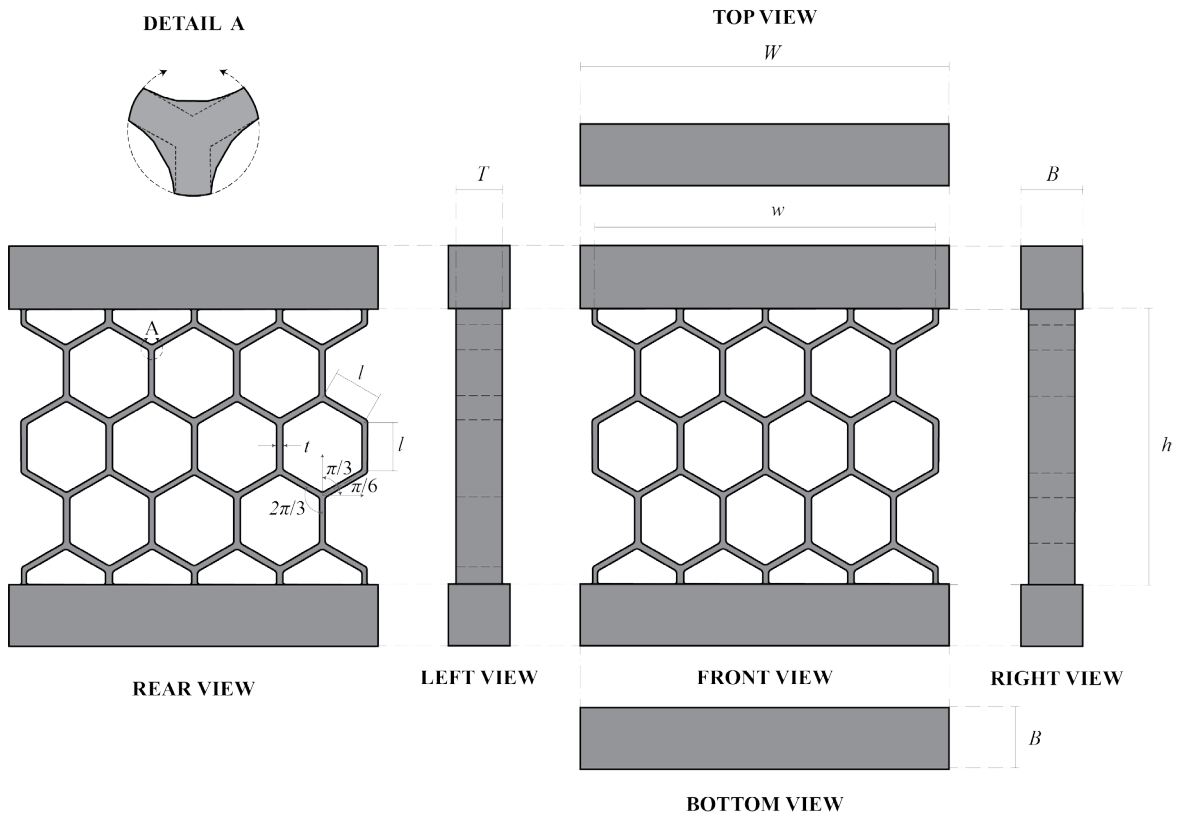


Fig. B.11 Technical drawing of the Matheck-filletted hexagonal honeycomb specimen, employing the American projection convention

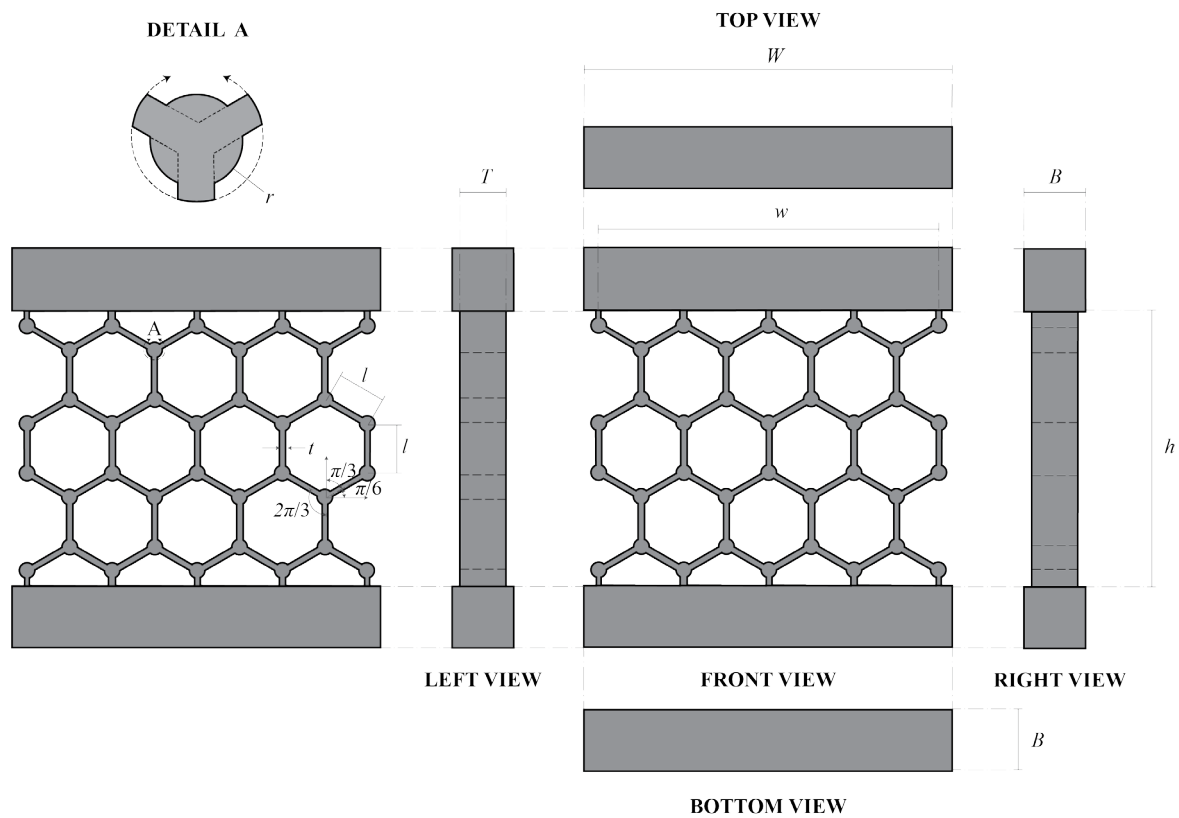


Fig. B.12 Technical drawing of the Lumped-node hexagonal honeycomb specimen, employing the American projection convention

## **C Overview of VIC3D 8 settings**

Table C.1 summarizes the VIC 3D settings used for all experiment analyses.

Table C.1 VIC 3D 8 settings

	VIC 3D 8 parameter settings
Subset size [pixels]	41
Step size [pixels]	10
Step size [pixels]	6
Interpolation type	8-tap
Criterion	NSD
Consistency threshold	0.02
Confidence margin: max. margin	0.05
Matchability threshold	0.1
Epipolar threshold	0.5
Compute confidence margins	Yes
Strain computation	13
Compute principal strains	Yes
Overwrite existing strains	Yes
Von Mises equivalent strains	Yes
Raw gradients	No



